University of California
Santa Barbara

Mechanics and flow of biological tissues

A dissertation submitted in partial satisfaction
of the requirements for the degree

Doctor of Philosophy
in
Physics

by

Arthur Scott Hernandez

Committee in charge:

Professor M. Cristina Marchetti, Chair
Professor Mark Bowick
Professor Sebastian Streichan

December 2023

The Dissertation of Arthur Scott Hernandez is approved.

Professor Mark Bowick

Professor Sebastian Streichan

Professor M. Cristina Marchetti, Committee Chair

December 2023

Mechanics and flow of biological tissues

Acknowledgements

I would like to thank my advisor Cristina Marchetti for training me both as a scientist and as a professional person. I am grateful for her support, encouragement, patience, and wisdom during my PhD studies. Over the years I have been repeatedly inspired by her insight in physics, her work ethic, and how much she cares about each of her students. I would like to also thank Michael Moshe who taught me a great deal and was like a second advisor to me, as well as Mark Bowick for his insight on how to discuss the geometry of physics problems in a precise yet simple and tasteful manner. I would also like to thank Sebastian Streichan for being on my committee and his encouragement. Much thanks also goes to Michael Staddon for teaching me a good deal about the minutiae of the vertex model.

I would like to thank my parents for creating me and encouraging my curiosity as a child which I attribute as a key reason why I decided to study physics. I am also grateful to my wife Lucía for all the support and help during graduate school and moving to Europe. I would also like to thank my brother Benjamin for giving me motivation to be a better role model.

Several teachers and friends have taught me about physics, the world, and myself through our interactions and conversations during the past 7 years. I would like to thank them, in no particular order: Will Wylie, Joey Paulsen, Merrill Asp, Manu Mannattil, Vito Iaia, Sarah Bratt, Gaye Ceyhan, Muhammad Asaduzzaman, Pinaki Abhilash, Shreyas Parthasarathy, Oran Szachter, Noemie Livne, Adolfo Holguin, Fernando Caballero, Robinson Mancilla, David Grabovsky, Austin Hopkins, Toshi Parmar, Sergio Sokolovskiy, Fridtjof Brauns, Benjamin Loewe, Paarth Gulati, Sattvic Ray, Thomas Rozycki, Aria Chaderjian, Preeti Sahu, Alex Smith, Monica Ripp, Chaitanya Afle, Nick Didio, Zhitao Chen, Jesse Held, Taka Park, Michael Czajkowski, Ali Imran, Gavriel Lo-

ria, Yakym Pirozhenko, Edward Warden, Tito Fonta, Niko Claussen, Yubi Chen, Enrique Morell, Molly Kaplan, Rüdiger Kürsten, Lorena Magaña Zertuche, Wayne Weng, Chris Browne, Joey Glynn, Berkan Uze, Roberto Abril, Sid Senthilkumar, Francesco Serafin, Diogo Pinto, David Schuster, Cesareo Contreras, Laura Nuño, Dan Schwartz, Zhihong You, Myles O'Leary, and Vitaly Nikolaev. If I forgot anyone, please forgive me, this list is too long which reflects that I talk too much.

Lastly, I would like to thank Dr. Jonathan Worstell who helped me find the confidence to apply to graduate school in the first place, and Mr. McCauley my high school physics teacher.

Curriculum Vitæ

Arthur Scott Hernandez

Education

2023	Ph.D. in Physics, University of California, Santa Barbara.
2019	M.S. in Physics, Syracuse University.
2014	B.A. in Physics, The University of Chicago.

Publications

1. **Arthur Hernandez**, M. Cristina Marchetti, `Poisson-bracket formulation of the dynamics of fluids of deformable particles,` , Published in: Phys. Rev. E 103, 032612 (2021).
2. **Arthur Hernandez**, Michael F. Staddon, Mark J. Bowick, M. Cristina Marchetti, and Michael Moshe, `Anomalous elasticity of a cellular tissue vertex model`, Physical Review E 105, 064611 (2022).
3. Michael F. Staddon, **Arthur Hernandez**, Mark J. Bowick, M. Cristina Marchetti, and Michael Moshe, `The role of non-affine deformations in the elastic behavior of the cellular vertex model` Soft Matter 19 (17), 3080-3091 (2023).
4. **Arthur Hernandez**, Michael F. Staddon, Mark J. Bowick, M. Cristina Marchetti, and Michael Moshe, `Finite elasticity of the vertex model and its role in rigidity of curved cellular tissues` Soft Matter (2023).

Abstract

Mechanics and flow of biological tissues

by

Arthur Scott Hernandez

Understanding the mechanics and flow of biological tissues invites a rethinking of how to formulate faithful *tissue scale* continuum theories based on *cell scale* structure. A common approach in modeling biological material is to utilize or modify theories originally developed to describe passive solids or fluids. Many textbooks and theoretical studies, for instance, on the solid mechanics of tissues, such as muscle fibers, skin, or organs, are typically based on elastic models of rubber or fiber-reinforced composites [1, 2]. For flowing biological material, such as blood or metastasized cancer cells, a non-Newtonian fluid model is often utilized [3]. While partly successful, these approaches do not consider that biological tissues are composed of flexible cells which may support self-tension and modify their own shape and are more akin to deformable droplets or foams than a conventional solid or fluid. Unlike a passive material with a preset structure, a biological tissue may adapt its mechanical properties at both the tissue and cell scale and presents a more challenging system to model. The research contained in this thesis addresses two questions. Firstly, how the solid-fluid transition of epithelial tissues can be understood as a consequence of *geometric frustration* [4] where cells cannot achieve target shape to relax tension and thereby behave rigidly, and how cells may utilize this to fine tune tissue mechanical properties. And secondly, how to develop a hydrodynamic description which distinguishes between shape elongation, which signals the solid-fluid transition, and possible local nematic alignment.

Summary

Chapter 1

Introduction

1.1 Jamming of biological tissues

The form and function of biological tissues within animal and human physiology is complex and involves a myriad of bio-chemical and mechanical processes as well as external factors such as gravity, temperature, and light. Biological tissues are also inherently modular, being composed of constituent cells that can carry out functions. In particular, one critically important ability of cells is the capacity to modify their shape and even move, both autonomously and collectively, in response to forces, and is an essential part of many biological processes such as tissue morphogenesis [5, 6, 7, 8], wound healing [9, 10, 11, 12], and cancer metastasis [13, 14, 15]. Single cell mechanics [16] and motility [17, 18] are well-studied. The connection between cell scale and tissue scale mechanics and motion is less well understood, however there has been a recent surge of interest in cell jamming transitions in dense biological tissues [19, 20], especially in the context of biological development [21, 22, 23, 24]. Understanding the mechanism that controls the rheological state of biological tissue presents an important and challenging problem in physics and quantitative biology.

A type of tissue frequently studied in biological development is the epithelium (plural: epithelia). Epithelia are ubiquitous structures in biology as they form the surfaces of organs, glands, and body cavities, and perform several functions which are key to survival and development. This type of tissue forms when mesenchymal cells adhere to one another to form a thin sheet of cells in what's known as a mesenchymal-to-epithelial transition [25]. This process is reversible in the sense that cells may separate from one another and move autonomously via an epithelial-to-mesenchymal transition [26]. The phenomenon plays an important part in biological processes such as in embronyic development [27, 26] and the metastasis of cancer cells [28, 29].

The epithelial-to-mesenchymal transition has been thought of as a sort of solid-fluid transition: a tissue with specific form and arrangement of cells can become fluid-like with cells re-arranging and slipping past each other, and is described as an unjamming of cells [30, 22]. However some argue for the distinction between the epithelial-to-mesenchymal transition and tissue fluidity [31, 21], because cells within a tissue may flow and rearrange while still maintaining the strong adhesion between cells characteristic of an epithelial tissue. Nonetheless, the jamming transition perspective has inspired much work in theoretical physics and quantitative biology to describe the onset and loss of rigidity in epithelial tissue, termed "tissue jamming" [32] or "cell(ular) jamming" [19, 20]. Various studies have tied the solid-fluid transition to multiple mechanisms, often occurring simultaneously, such as crowding [33, 32, 34, 35], cell fluctuations [27, 36, 37, 38], individual cell motility [39, 40], and cell-cell adhesion [41, 42].

Generally, cells in epithelia are densely packed, forming a confluent sheet with minimal connective material between cells. In simple epithelia, this sheet is a monolayer of cells which break top-down symmetry by having cells' apical membranes tethered to one another via adherens junctions. The adherens junctions also connect to the cell cortex, resulting in a network of cell edges under tension at the apical surface of the epithelium

which resembles a polygonal tiling. The adherens junctions bind cells to one another by linking actin filaments which permeate the cell interior, and thereby allows cells to mechanically coordinate with one another via their actin cytoskeleton [25].

The structure of the epithelium is directly reflected in the junction network, which in turn is regulated by a variety of mechanisms, such as cell motility (cell-cell rearrangements), remodeling (birth-death processes, extrusions), myosin recruitment, and cell packing morphology. The geometric information encoded in this network serves as key data in quantitative biology and theoretical modeling of the mechanics and dynamics of tissues [43, 44]. In particular, imaging analysis of the junction network of epithelia both *in vitro* and in developing embryos reveals a close connection between cell shape and network topology on one hand and mechanics and shape at the tissue scale.

In vitro experiments and analysis by Park *et al.* [30] of bronchial cells report a transition of cells from a liquid-like state where cells freely exchange neighbors to a jammed, solid-like, state at constant cell density, as quantified by the measured Mean-Square-Displacement (MSD) of cell motion. Paradoxically, this jamming transition is not associated with cellular crowding nor with increased cell-cell adhesion. In fact, amplification of cell-cell adhesion was found to correlate, instead, with the unjammed, liquid-like state. Rather, the observed fluidization of bronchial cells was found to be associated with a change in mean cell shape. This counter-intuitive result validated a previous theoretical prediction of a rigidity transition in the Vertex Model of tissue, where the cell shape index s, defined as the ratio of perimeter P over square root area A of each cell, averaged over all cells, $s = \langle \frac{P}{\sqrt{A}} \rangle$, serves as a structural order parameter [45, 46, 47, 48]. For a given junction network, the shape index quantifies how rotund or elongated cells are on average, with regular shapes having a smaller shape index than irregular ones. In disordered vertex model simulations jamming is observed to occur at a shape index of ≈ 3.81 [48], a value in agreement with experiments in bronchial tissues [30]. Larger

values of s correspond to a liquid-like state where cells tend to be larger and elongated. This type of cell-shape mediated fluidization of epithelia has also been observed in other tissue, such as in *Drosophila* [49] and *Tribolium castaneum* [50] development, as well as in tumor cells [51].

An example of the correlation between cell shape and solid-like or fluid-like tissue response is gastrulation during early embryonic development in *Drosophila* [22]. At this stage of development, the embryo consists of an ellipsoidal surface of cells wrapped around a fluid yolk. A major morphogenetic event in *Drosophila* gastrulation is ventral furrow (VF) invagination [52], where the embryo partially folds into itself, followed by subsequent germ-band extension (GBE). During GBE cells are collectively transported by convergent extension with frequent cell-cell rearrangements; simultaneously, cells on the dorsal side, in what is known as the amnio serosa, accommodate GBE via a combination of both cell shape changes and cell-cell rearrangements [24, 23, 7, 53]. Lastly, during early *Drosophila* development, jammed and unjammed regions of cells correlate with regions of high and low *intrinsic* curvature, respectively, reflecting the interplay between shape and rigidity [54]. The synchronous fluid-like and solid-like tissue behaviors are key ingredients of morphogenesis and aide the embryo in acquiring its final functional 3D shape.

1.2 How to describe rigidity

The study of the transition between flowing and solid states of matter is a rich area of physics, with scientists utilizing different approaches depending on the specific system. One framework to think about solid-fluid transitions is spatial symmetry such as in crystalline solids which may be modeled as a lattice of atoms/molecules with discrete rotational and translational order. This lattice structure defines a reference state of the solid. The linear, and sometimes even nonlinear, mechanical response to external de-

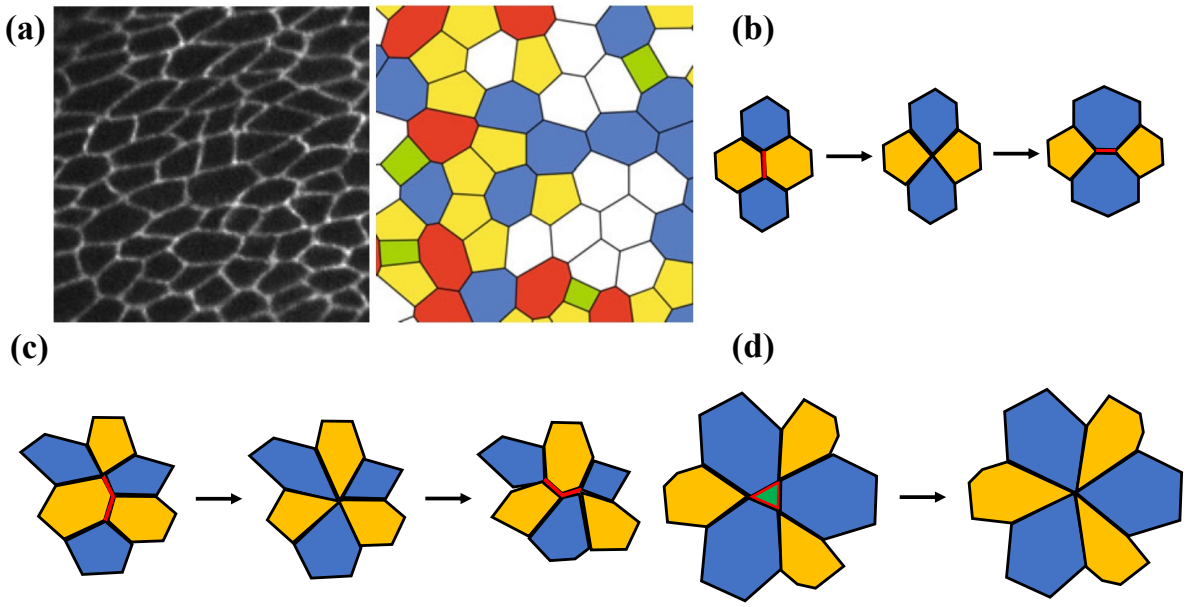

Figure 1.1—(a) Confocal image data taken from [46] of epithelial tissue from Drosophila wing during development compared with vertex model representation of epithelia as a polygonal tiling of the plane. (b)A T_1 transition between a quartet of cells whereby an edge shrinks to a vertex, and then decomposes into two vertices an d a new edge. The result is an exchange of neighbors between cells. (c) A generalized version of a T_1 process involving more cells, resulting in an intermediate multicellular rosette configuration whereby 5 or more cells share a vertex. (d) A T_2 transition where a cell (green triangle) shrinks to a vertex and is removed resulting in a multicellular rosette, corresponding to cell delamination or apostosis.

formations imposed on this reference state, as characterized by elastic constants such as Young's modulus and Poisson's ratio, can be theoretically predicted from the lattice structure [55, 56, 57, 58]. The destruction of crystalline order - or melting - corresponds to the loss of spatial symmetry and indicates the onset of fluidization [58]. The lattice structure framework is intuitive when thinking of systems with a naturally periodic microstructure such as ice or metals, and has served as a springboard for statistical theories addressing the role of defects and order in solid-fluid phase transitions in 2D such as in KTHNY theory [59, 60, 61]. This framework of has also provided insight in studying amorphous solids where the proliferation and flow of defect-like regions is associated with

failure and plasticity [62, 63]. Additionally, the idea of a pre-stressed reference state has been used to modify theoretical tools developed for crystalline solids to, instead, describe the mechanical response of amorphous solids [64, 65].

The solid or fluid response of materials can also be understood by consideration of the time scales involved. For example, Oobleck putty is a viscoelastic fluid composed of cornstarch and water whose mechanical response is a function of the rate of imposed strain. A sudden mechanical perturbation results in a solid-like response, but if perturbed at a slower rate the putty responds like a fluid. In Oobleck polymer strands are embedded in water and relax with a certain characteristic time after being deformed. If strained at a fast enough rate, the polymers cannot fully relax resulting in stress built up and solid-like response; whereas, at a slow enough strain rate the polymer strands can relax before stresses build up, resulting in a fluid response.

Lastly, density mediated jamming is another route towards rigidity. In this case structural rearrangements cease upon increasing density due to particle crowding, resulting in a spontaneous restriction of phase space and yielding a jammed state [66]. It is an example of ergodicity breaking due to the spontaneous collective arrest of particles[67].

These examples, though not exhaustive, illustrate how, depending on the system, the question of distinguishing between rigid and flowing states can be understood by different metrics. It is not surprising that continuum models developed to describe the solid and fluid aspects of biological tissues often make contact with, or even directly import, tools from these other frameworks. For instance, the observed junction network in epithelia can be naively taken to encode rigidity, as is the case with a crystalline solid or spring network, and has motivated the use of a Hookean type elasticity model [68, 69, 70]. This approach fails to capture the solid-fluid transition signaled by cell shape, nor accounts for the non-affinity of the mechanical response which is a robust feature of cells in epithelia [53].

Biological tissues are characterized by several time scales corresponding to various biochemical processes, cell division and death, cellular rearrangements, and morphogenetic events. *In vitro* rheological studies of cell aggregates and monolayers show that cellular tissue responds viscoelastically: it is able to support stress on short time scales but it flows on longer time scales [71]. A still relatively open question is how to formulate a constitutive relation between stress and strain that incorporates the role of cell shape. There is analogy to rheological models of binary immiscible fluids [72] and foams [73] under shear, where droplets or bubbles undergo shape changes, change orientation, and rupture, engendering unusual rheology. Several groups have tried to incorporate cell shape, birth and death processes, and cellular rearrangements in continuum models of biological tissues, yielding models which connect these cell features to macroscopic properties such as diffusivity, viscosity, strain stiffening, tissue polarity and finite yield stress [74, 75, 76, 77, 78, 79].

Even though epithelial tissues can fluidize at fixed density, ideas developed in the context of conventional packing and jamming theories can still be useful to describe the atypical jamming transition of epithelia. An example is the notion of geometric frustration, as known to occur in dense colloids [80], liquid crystals [81], magnets [82], and packings of spheres [83]. These systems can exhibit structural organization which is incompatible with the local interactions and/or the embedding space. This sort of structural incompatibility or geometrical frustration [4] can not only alter physical proprieties [84], but also yield highly degenerate ground states [85]. Geometrical frustration has been recently identified in Vertex and Voronoi models of epithelia tissues [86, 87, 88, 89] and in programmable metamaterials, where the shape of the building blocks or the cells can control mechanical response and engender anomalous elasticity, such as auxetic behavior [90], as well as encode Goldstone modes [91, 92, 93, 94], self-assembly [95, 96, 97], and rigid to floppy transitions [89, 98, 86].

In the context of 2D biological tissues, the rigidity transition in the Vertex model arises from the cells' inability to simultaneously satisfy constraints set by target area and target perimeter. This occurs for parameter values corresponding to target shapes which are not geometrically realizable and thus are incompatible. The resulting frustrated state, as will be explained in this thesis, yields rigidity. In the next section we describe the vertex model and emphasize its inherently geometrical aspects. Next, I review relevant work on the ground states of the vertex model which relate shape incompatibility to rigidity, and provide some commentary on the connection between the model and the isoperimetric inequality.

1.3 Vertex model: biological tissues as polygonal tilings.

The connection between cell shape and tissue functionality is a recurrent theme in biology and has interested scientists for over a century. For instance, a honeycomb packing[1] is often tied to several biological processes, such as in Drosophila eye development and hair formation on wing discs [100, 101]. The Scottish mathematician D'Arcy Thompson attributed the ubiquitous motif of hexagonal packing in confluent tissues to force balance, conceptualizing cells as bubbles in a foam under surface tension [102]. A century later, laser ablation techniques have confirmed that junction networks in epithelial tissues are typically under tension even when cells are irregular and undergo cell-cell rearrangements [103]. Other structural motifs in the epithelium may be explained by topology: an argument based on simple mathematical principles can explain why, on average, cells have 6 neighbors due to cell proliferation, and offers an explanation for the predominance of hexagonal topology[2] in epithelia [105]. While these mathematical

[1]The honeycomb conjecture dates to antiquity and states that a honeycomb tiling subdivides the plane with the least amount of perimeter, and was first rigorously proved in 1999 [99].

[2]The hexagonal topology of the junction network suggests that cells are also, on average, in some sense also hexagonal in shape: if each cell has 6 neighbors, and therefore 6 edges, then one has a hexagon.

insights aide in developing some intuition on the observed structure of cellular tissues, they cannot provide a complete account for aspects such as cell size and shape changes, nor mechanical properties, let alone the dynamics of bulk tissue during development.

An open question in tissue mechanics is the emergence of global scale mechanical properties of biological tissues due to collective cell coordination and single cell proprieties such as the various proteins within the cytoskeleton which give cells their shape and integrity, as well as the adhesion molecules which bind cells together [106, 107, 108]. There have been several proposed theoretical models to describe epithelial tissues, both at the microscope level, for instance, via a cellular Potts model [109], and at the tissue scale via various continuum models which can account for polar and nematic order, viscoelasticity, mechano-chemical feedback, and cell motility [110, 111, 112, 113]. A fruitful starting point in capturing the mechanical proprieties of biological tissues has been the vertex model, which describes a densely packed cell monolayer as a polygonal pattern and was first proposed as a model for simple epithelia by Ref. [114].

The vertex model is a 2D model which describes each cell's apical surface as a polygon, each cell-cell junction as an edge between two polygons, and each multicellular junction as a vertex, and thus the epithelium's junction network is cast a polygonal tiling. The precise formulation of vertex models differs widely between contexts, and the model was originally developed to describe foams [115, 116], soap bubbles [117], and grain boundaries [118]. In the context of epithelial tissues, the model can incorporate network tension, area constraints, biochemical feedback, noise, as well as topological rearrangements connected with cell motility, cell intercalation, and cell division through changes in lattice network [44, 113].

Tissues exhibit several time scales with the shortest one being the relaxation of cell

The recent findings of small scale hexatic order in epithelia is unsurprising if one defines hexatic order via cell shape [104].

shape in response to local deformations, typically on the order of seconds to minutes. Cell division and tissue shape changes occur on the order of hours to days. Thus, at short time scales the tissue can be assumed to respond to imposed deformation quasi-statically, motivating the assumption that cells are in force balance as described by an energy functional. The vertex model free energy for a collection of N cells labelled by Greek indices $\alpha, \beta = 1, 2, \cdots, N$ can be written as [46]

$$E = \sum_{\alpha=1}^{N} \frac{\kappa_A}{2}(A^\alpha - A_0^\alpha)^2 + \sum_{i,j}^{M} \Lambda_{ij}\ell_{ij} + \sum_{\alpha=1}^{N} \frac{\Gamma_\alpha}{2} P_\alpha^2 \tag{1.1}$$

The first term on the right hand side of Eq. (1.1) describes the energy cost for a cell to change its area A^α relative to a target value A_0^α, with κ_A is areal elasticity. It arises from the incompressibility of cells tissue in 3D, which allows for cells to change their area by changing their height. The second term corresponds to cell-to-cell interactions along the junction network. Here ℓ_{ij} is the length of the cell edge connecting vertices i and j, with Λ_{ij} the line tension along the corresponding edge. The sum here is over all cell edges, as denoted by the M vertices of the network. Vertices are labelled by Latin indices $i, j = 1, 2, \cdots, M$. The tensions Λ_{ij} are controlled by the interplay of cell-cell adhesion and cortex contractility and can be negative when adhesion overcomes contractility. Finally, the last term describes active cell contractility and elasticity of the cell's cytoskeleton, which together set an overall cell contractility via Γ.

Given a coordinate system, the vertex positions can be prescribed by Cartesian vectors $\mathbf{R}_i$. Force balance then corresponds to minimizing the energy with respect to the positions of the vertices, which gives a system of M coupled equations obtained by imposing $\frac{\partial E}{\partial \mathbf{R}_i} = 0$.

The parameters of the vertex model account in an effective manner several biochemical processes. For instance, the cell tensions Λ_{ij} are controlled by the interplay

of E-cadherins that tune cell adhesion [119, 120] and myosin that regulates contractility of the cytoskeletal network and whose recruitment is in turn regulated by mechanical feedback [53]. What makes this energy functional distinct from a Hookean approach (masses and springs) is the second term due to line tension between cell junctions. In lieu of each edge having its own independent spring constant, the strength of the tensions is instead set by cell-cell interactions and network topology: cell-cell adhesion favors contact, thereby increasing perimeter, whereas subcortical tension favors minimizing cell boundary. Thus, each edge's individual elasticity is inherently nonlocal.

The vertex model energy is highly degenerate and does not *a priori* fix a unique ground state for any given network. Stability criteria such as Maxwell counting fail to determine the system rigidity based on network topology[3]. To elucidate this degeneracy, consider the special case where line tension is uniform $\Lambda_{ij} = \Lambda$, then one may complete the square and drop a constant term to re-cast the tissue energy as

$$E = \sum_{\alpha=1}^{N} \frac{\kappa_A}{2}(A^\alpha - A_0^\alpha)^2 + \frac{\kappa_P}{2}(P^\alpha - P_0^\alpha)^2 \tag{1.2}$$

where $P_0 = -\frac{\Lambda}{2\Gamma}$ sets target perimeter and $\kappa_P = \Gamma$. This energy penalizes harmonic derivations away from target area and target perimeter instead of individual target edge length. A mechanical system governed by this energy, unlike a Hookean network of springs, is underconstrained for any network topology because area and perimeter constraints do not in general fix a unique shape, and therefore the system is floppy. Even a hexagonal triangular polygonal network, which would certainly be rigid for a collection

[3]Models of confluent tissues, such as the vertex model, typically describe a tissue network with predominately triplet junctions, i.e. 3 cells meet at each vertex. Quartet and higher order junctions and can occur during cell-cell rearrangement via a T_1 transition. A modified Maxwell counting procedure outlined in [121] shows that the solid-to-fluid transition in the vertex model can be driven by both rosette density (see Figure 1.1 (b,c,d)) *and* intracellular tension, confirming that network topology alone is not sufficient.

of springs, is floppy: a triangle has 3 degrees of freedom, but this energy only constrains two of them [122, 123].

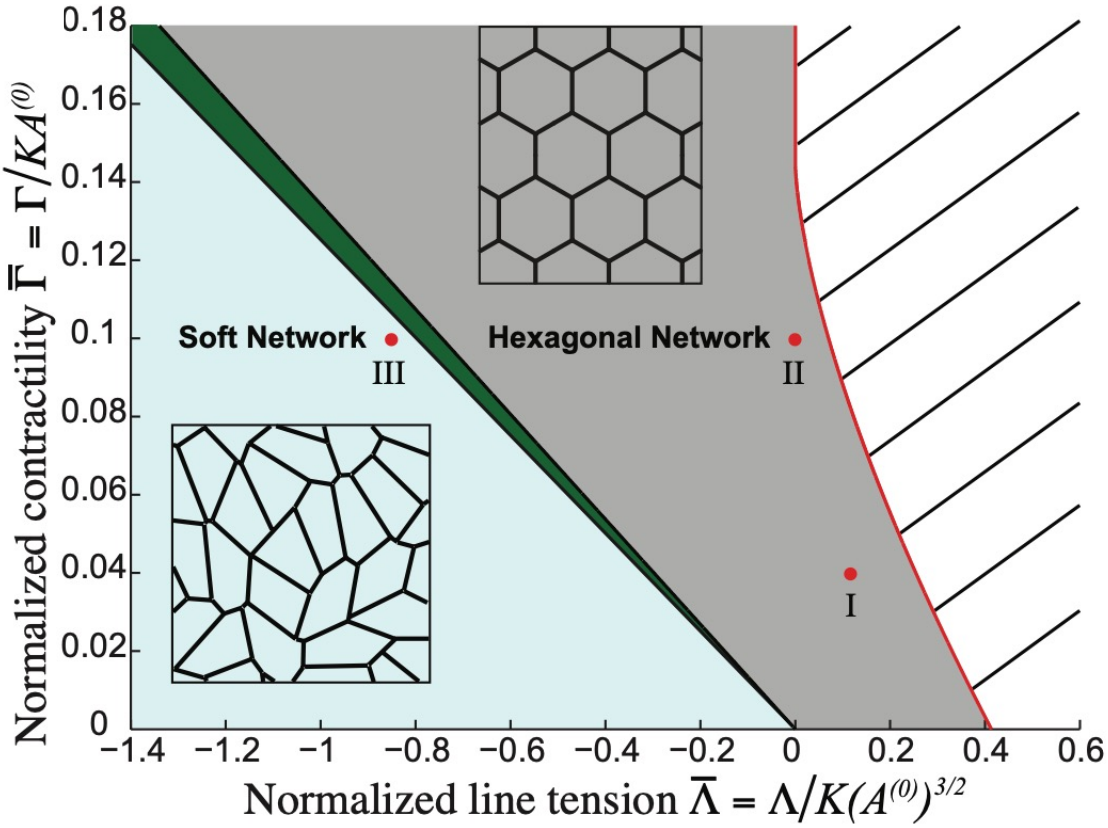

Figure 1.2—Ground states of the vertex model for rescaled Λ and Γ of Eq. (1.1) from [101] for a network of fixed lattice topology, where each vertex connects 3 edges. In the grey region force balance/energy minimization fixes the network into a regular hexagonal tiling, with a finite shear modulus. In the green and blue regions the system is highly degenerate, corresponding to irregular hexagons, and has a vanishing linear and nonlinear shear modulus in the green and blue regions, respectively.

What encodes rigidity into the model is the interplay between area and perimeter constraints along with other possible external constraints such as imposed stretching, shearing, dilatation, and the embedding geometry. The work of Staple *et al.* was the first to explore how rigidity in the vertex model ties to target perimeter, $P_0 = -\frac{\Lambda}{\Gamma}$ and target area, A_0. Their results [101] on the ground states of the VM, summarized in Figure 1.2, show a transition between rigid states (with non-zero shear modulus) to floppy states

(with a vanishing shear modulus) at fixed lattice topology, with the transition tuned by P_0 and A_0. Furthermore, they find that topological rearrangements, such as T_1 and T_2 processes (see Figure 1.1), involve energy barriers. Thus, the lowest energy response to imposed (small) shear deformations is cells changing shape rather than intercalation. The vertex model encodes two distinct paths towards fluidity at constant density: a purely geometrical route arising from the inherently unconstrained nature of the energy, in contrast to the more conventional route of fluidization corresponding to topological rearrangements of cells.

The rigidity transition tied to geometry can be thought in terms of a cell's ability to achieve a target perimeter, and therefore target shape (if we fix area) as tuned by P_0, and whether this is geometrically realizable. A cell's perimeter must adhere to necessary conditions that Euclidean geometry imposes on shape itself. The isoperimetric inequality describes these geometric constraints by stating a lower bound on the relationship between a polygon's area and perimeter in the Euclidean plane [124]

$$s_0^* \leq \frac{P^2}{A} \tag{1.3}$$

Where $s_0^* = \sqrt{4n \tan\left(\frac{\pi}{n}\right)}$ is the isoperimetric quotient, and in the limit of large n recovers the lower bound for general domains [124]. In the absence of external deformations and boundary conditions, this inequality is the only constraint on the ground states of the vertex model. This inequality is a weak constraint, amounting to a compatibility condition on shape and cannot fix cell size[4] or shape - for this, one really needs to study the energy landscape of Eq. (1.1). However, the inequality is sharp in the sense that, as shown in Chapter 2, s_0^* sets the transition, as tuned by P_0 and A_0, between rigid and floppy states of the vertex when $s_0^*(n) = \frac{P_0}{\sqrt{A_0}}$ for a system consisting of a

[4]Note that the isoperimetric inequality is scale invariant.

uniform triangular, quadrilateral, and hexagonal network, corresponding to $n = 3, 4, 6$, respectively. In disordered vertex models the critical point is given by $s_0(5) \approx 3.81$, corresponding to a pentagon. The critical value $s_0(5) \approx 3.81$ can be argued by a scaling analysis done in Ref. [48], but a more intuitive picture can be gotten by noting that during a T_1 transition a quartet of cells all become pentagons, see Figure 1.1 (b).

1.4 Outline

This thesis presents my doctoral research which has centered around a single question, namely how cell shape controls the athermal bulk mechanical and flow properties of a confluent biological tissue. It builds upon the work of Staple, Farhadihar and collaborators who first identified the deep connection between cell shape and tissue rigidity [46, 45, 101]. All of my doctoral work has been restricted to a single theoretical description - the vertex model. Nonetheless, this simple model engenders a great deal of possibilities, as reflected by the myriad of theoretical and computational studies referenced above.

The first three chapters are based on articles published in PRE and Soft Matter, and report on a mean field theoretic treatment of the linear and nonlinear mechanical response of the vertex model. Despite the absence of several important physical features, such as $T_{1,2}$ processes, growth and death processes, and biochemical-mechanical feedback, the mean field model encodes novel elasticity such as the coupling between shear and compression/dilation modes, curvature mediated rigidity transitions, and robust non-affinity in the linear mechanical response. These anomalous elastic proprieties are fundamental features of the model, and are obtained in both experimental and computational data [79, 125, 77], demonstrating that they need to be accounted for in any faithful continuum theory of tissue based on the vertex model. The fifth chapter presents a continuum model which incorporates cell shape anisotropy as an order parameter for

the solid-fluid transition, coupled to local order of elongated cells. While many epithelia exhibit ordered states, fluidized tissues are typically disordered and thus cell anisotropy and local (nematic) order are connected to distinct types of phase transitions. I conclude in the sixth chapter with a brief summary.

Chapter 2

Anomalous elasticity of the cellular tissue vertex model

This chapter is adapted from a 2022 Physical Review E article [126] co-authored with Michael Moshe, Michael Staddon, Mark Bowick, and M.Cristina Marchetti. Theoretical work was performed by Michael Moshe and myself, and simulations by Michael Staddon, with M. Cristina Marchetti, Mark J. Bowick, and Michael Moshe providing mentorship, manuscript editing, guidance, and support.

2.1 Introduction

Biological tissue are active materials capable of generating mechanical stresses and transmitting such stresses at the organ and organism scale [127]. In the other direction, imposed global forces on tissues typically result in individual cell responses [30], reflecting the strong connection between tissue scale and cell scale mechanics. The ability of a biological tissue to tune its own rigidity and thereby adapt its mechanical response to external perturbations engender significant challenges for the formulation of a continuum description.

Chapter 1 introduced the idea that a bulk tissue may become solid-like due to self-tension of cells in the context of the vertex model, and tied the onset of rigidity to *geometric incompatibility*. This geometry-driven transition between rigid and floppy states has been identified before in Vertex and Voronoi models of confluent tissue [86, 128, 87, 88], but the characterization of the elastic and rheological response of the VM to external deformations is only beginning to be addressed [129].

The existence of a potential energy and of a single reference state are crucial ingredients for constructing continuum elastic theories of solids, where the linear response to small deformations is analyzed via an expansion of the energy to quadratic order in strains. Both ingredients are absent in living matter, where out-of-equilibrium active processes prevent the formulation of a conservative potential energy and the under-constrained structure of the cellular network results in highly degenerate ground-states. This prevents the identification of a unique rest configuration with respect to which deformations and strains can be measured. As a result, the formulation of a continuum elasticity of living matter that incorporates both active processes and the intrinsic rigidity arising from the structure of the cellular network remains a formidable challenge.

In recent work, Schneibner *et al.* have proposed a continuum theory of active solids

that lack a potential elastic energy [130]. By coarse-graining a model of active force generators on a triangular lattice, these authors showed that the elastic stiffness tensor of an active solid contains an asymmetric part that violates conservation of energy and reciprocity. While the elastic response of a homogeneous and isotropic passive solid with a single rest configuration is fully characterized by just two elastic moduli describing the response to shear and isotropic dilation/compression, these authors showed that the description of the mechanics of isotropic elastic solids with active bonds requires a theory of "odd elasticity", with two new elastic moduli that stem from the ability of an active elastic medium to go through a closed cycle of quasistatic deformations with non-zero total work output.

In this chapter we examine how geometric constraints affect the continuum elasticity of cellular networks in the context of the two-dimensional Vertex Model (VM). The VM describes a confluent tissue as a network of polygons tiling the plane. Each polygon represents a cell and is characterized by target values of area and perimeter encoding a variety of bio-mechanical mechanisms [131, 114, 46, 45, 132, 44, 48, 113, 133]. The observed cells' area and perimeter are controlled by a tissue energy that penalizes deviations from the target values. Most studies of the VM have focused on disordered and active realizations, where the polygons form a disordered network and active processes can drive cell rearrangements and neighbor exchanges [134, 89, 135, 136]. Here, in contrast, we consider an ordered realization where the network is composed of regular polygons and neglect active processes responsible, for instance, for T_1 transitions. This allows one to isolate the structural and energetic origin of the rigidity transition associated with geometric incompatibility.

By combining mean-field theory and numerical simulations, we show that the response of the VM to infinitesimal deformations is never described by linear Hookean elasticity. Specifically, the fluid state exhibits vanishing stiffness up to a critical strain

as it can accommodate external strains with zero stress by spontaneous shear. The rigid state has finite linear response, but the measured elastic moduli do not satisfy the conventional relations of isotropic linear elastic solids, where the response to small deformations is fully characterized by just two independent stiffnesses. The strongest deviations from linear elasticity are found in the critically-compatible state. In this state mechanical reciprocity is violated, an anomalous coupling between bulk and shear deformations emerges, and quartic rigidity is observed in response to specific linear deformations.

Recent work by [125] has examined numerically the response of a disordered Voronoi model, that naturally incorporates topological rearrangements, to quasi-static shear. This work finds that the compatible/fluid state exhibits zero stress below a critical applied strain, confirming the results of our minimal mean-field approach. It additionally shows that both the liquid and the solid exhibit shear stiffening above a critical strain and that a mean-field theory that incorporates the ground state degeneracy of the compatible regime captures the nonlinear behavior of the shear response.

Although derived from an energy, the VM elasticity shares similarities with odd elasticity, including the breakdown of reciprocity and the emergence of an anomalous coupling between isotropic and shear deformations. As in odd solids, the linear response of the VM violates the basic symmetries of the elastic stiffness tensor of passive solids and the elastic response depends on the protocol of the deformation. Contrary to odd elasticity, these properties emerge not from a sustained energy input that breaks the conservative nature of forces, but from pure geometric constraints that result in the failure of a Taylor expansion to faithfully describe the elastic potential energy even for small deformations. The geometric origin of the anomalous elasticity is highlighted through a derivation of a generalized continuum elastic theory of the VM, which provides excellent quantitative agreement with the numerical simulations. These findings provide new insights into the geometrical aspects of tissue mechanics, which underlie in an essential way the rigidity

transitions controlled by active processes. They also lay out a path for the design of new mechanical metamaterials with mechanical properties mimicking those of living tissue.

The structure of this chapter is as follows: Sect. 2.2 reviews the properties of the passive ordered VM. Sect. 2.3 introduces a mean-field approach to VM, implemented in Sect. 2.4 to measure global response to uniform loads, and compared with numeric results. Sect. 2.5 shows that the measured properties violate linear elasticity. Sect. 2.6 proposes a visual representation of VM mechanics, uncovering the source of its peculiar behavior and the required modifications to classical elasticity. The last section 2.7 provides a brief summary and offers directions for the road ahead.

2.2 Vertex Model and geometric incompatibility

In the VM, each cell is described as a convex polygon with target area and perimeter A_0 and P_0 respectively. Given a configuration with actual area A and perimeter P, the cell stores a mechanical energy

$$E_{\text{cell}} = \frac{\kappa_A}{2}\big(A - A_0\big)^2 + \frac{\kappa_P}{2}\big(P - P_0\big)^2 \,. \tag{2.1}$$

A tissue consists of a network of many such cells, covering the plane. Cells in epithelial tissue typically resemble disordered arrangements of mainly 5−, 6− and 7−sided irregular polygons, with an average coordination number of 3 at each vertex. To highlight the qualitatively new mechanics emerging from purely geometric constraints, here we consider the seemingly simple quasi-static response of a uniform tissue (i.e. uniform A_0 and P_0) to uniform imposed loads that lead to uniform observed A and P. We assume that all cells respond identically. Thus the tissue energy is $E = N\,E_{\text{cell}}$ and it is sufficient to analyze the behavior of a single cell. This corresponds to a mean-field theory of the

tissue VM. Additionally, for clarity we mainly analyze the case of a triangular tissue. This transparent example is also closer to the familiar discrete model of elastic materials [55, 137, 138]. Our results are not qualitatively affected by the specific polygonal shape considered.

A naïve degree-of-freedom counting reveals that the VM is under-constrained [121, 87]. Even the most rigid polygon, a triangular cell, has three structural degrees of freedom, corresponding to the lengths of the three edges, but fixing target area and perimeter only imposes two constraints, implying that a single triangular cell is floppy.

As mentioned in chapter 1, recent work has shown that VMs exhibit a transition tuned by the *target* shape index $s_0 = P_0/\sqrt{A_0}$ between a fluid-like state where cells freely intercalate and a rigid state where cells are collectively jammed [48, 39, 30]. The order parameter for this transition is the *observed* cell shape index defined as $s = P/\sqrt{A}$. In early work the loss of rigidity was associated with the vanishing of energy barriers for neighbor exchanges known as T_1 transitions which mediate local changes in network topology [48]. Studies of VMs with fixed topology (hence no T_1 transitions) have suggested, however, that a possible underlying origin of this transition is the geometric incompatibility of the target shape index with the embedding space: in a regular version of the VM, rigidification occurs when the target shape index violates the isoperimetric inequality which requires $s_0 \geq s_0^*(n)$, with $s_0^*(n) = \sqrt{4\,n\tan(\pi/n)}$ for a regular n-sided polygon [45, 46, 86, 89]. An ordered vertex model of n-sided polygons hence undergoes a transition at $s_0 = s_0^*(n)$. For $s_0 < s_0^*$ the cells cannot achieve their target shape and the tissue is in a rigid, incompatible state, with a single finite-energy ground state. For $s_0 > s_0^*$ the tissue is soft/floppy, or compatible, with multiple zero-energy configurations.

Since in the incompatible state the tissue has a well-defined, albeit frustrated, ground-state configuration, one may think that such a ground state would be a legitimate reference for measuring deformations and that an expansion about such a state to quadratic

order in the strain would provide an accurate description of the linear elastic response of the system. In the present chapter I show that this is not the case, and that the response of ordered VMs to small deformations deviates qualitatively from linear elasticity. The next section presents a mean-field model that justifies this conclusion and then uses it to calculate the various elastic moduli that quantify the response to uniform imposed loads.

2.3 Mean field theory and ground states

The elastic moduli of a tissue encode information about the mechanical response to uniform external loads. We assume that in a uniform ordered tissue the responses of all cells are identical, and formulate a mean-field theory by considering the elastic energy of a single cell, Eq. (2.1). To begin, we express the energy in terms of configurational variables by introducing the symmetric 2×2 metric tensor $\mathbf{g}$. Denoting the unit vectors defining a regular polygon by $\mathbf{v}_i$ and the polygon's area by ΔS, we can then write cell perimeter and area as

$$A(\mathbf{g}) = \sqrt{\det \mathbf{g}}\, \Delta S \,, \tag{2.2}$$

$$P(\mathbf{g}) = \sum_{i \in \text{cell}} \sqrt{\mathrm{v}_\mathrm{i}^\alpha \mathrm{g}_{\alpha\beta} \mathrm{v}_\mathrm{i}^\beta} \,, \tag{2.3}$$

where Greek indices α, β denote Cartesian components. Note that for triangles all configurations can be parametrized exactly as in Eqs. (2.2) and (2.3). For higher order polygons the description of edges in terms of a single uniform metric is an approximation.

It is convenient to introduce dimensionless quantities by using $\sqrt{A_0}$ as the unit of length. The dimensionless form of Eq.(2.1) is then

$$E = \frac{E_{\text{cell}}}{\kappa_A A_0^2} = \frac{1}{2}\left(a(\mathbf{g}) - 1\right)^2 + \frac{r}{2}\left(p(\mathbf{g}) - s_0\right)^2 \,, \tag{2.4}$$

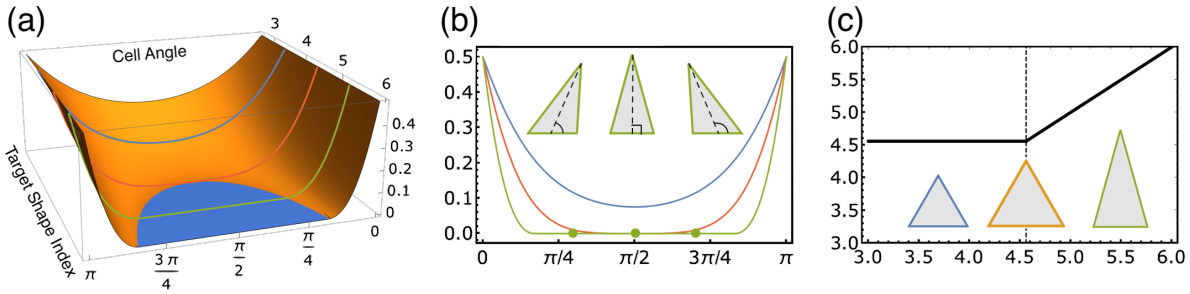

Figure 2.1—(a) Ground-state energy E_0 as function of the target shape index s_0 and tilt angle θ measured between the median and the cell base. The blue region corresponds to zero energy, reflecting the degeneracy of the ground-state in the compatible regime. The colored lines describe E_0 as function of θ for $s_0 = 3.5, 4.55901, 5.3$, corresponding to the incompatible, critical, and compatible regimes, respectively. The three curves are plotted together in (b) as function of θ, with the inset showing three different zero energy configurations corresponding to the compatible green curve. (c) Observed s vs. target perimeter s_0. In the incompatible regime $s_0 < s_0^*$ the ground-state configuration is isotropic, whereas in the compatible regime $s_0 > s_0^*$ the ground-state configuration is anisotropic and degenerate. The smaller scale of the incompatible (blue edge) cell illustrates the compromise of ground-state area and perimeter being smaller/larger relative to their target values $a < 1$, $p > s_0$.

with $a = A/A_0$, $p = P/\sqrt{A_0}$ and $r = \kappa_P/(\kappa_A A_0)$ a parameter that sets the relative cost of perimeter to area variations. This form of the energy functional has strong similarity with that of non-Euclidean shell theory, where stretching and bending terms may be incompatible due to violation of geometric compatibility conditions [139]. The absence of a stress-free configuration when $s_0 < s_0^*$ is transparent in this form, since the isoperimetric inequality states that for $s_0 < s_0^*$ there does not exist any $\mathbf{g}$ which can satisfy both $a = 1$ and $p = s_0$ simultaneously.

Before examining the mechanical response to small perturbations, we need to find the ground-state energy. This is determined by minimizing Eq. (2.4) with respect to all admissible metric tensors $\mathbf{g}$. The ground state metric $\mathbf{g}_0$ is given by

$$\mathbf{g}_0 = \arg\min_{\mathbf{g}} E(\mathbf{g}; s_0, r) \ . \tag{2.5}$$

The calculation of $\mathbf{g}_0$ for a given n-sided regular polygon as a function of (s_0, r) can be carried out analytically and is shown in Appendix 2.B for $n = 3, 4, 6$. For $s_0 < s_0^*$ there is a unique ground state corresponding to a regular polygon and a gapped energy. In this regime, referred to as the incompatible regime, the system is rigid. As $s_0 \to s_0^*$ from below, the energy gap vanishes. For $s_0 > s_0^*$ the system transitions to the compatible regime, where there is a one-parameter set of zero-energy configurations, making the tissue floppy. This is shown in Figure 2.1(a,b) where we plot the ground-state energy of a single cell as a function of its target shape index s_0 and the tilt angle between the median and the cell base, which provides a measure of shear deformation. This angle parametrizes a family of zero energy states in the compatible regime. In Figure 2.1(c) we show the observed ground state shape index s as a function of the target shape index s_0. The inset displays ground-state configurations. In the incompatible regime for $s_0 < s_0^*$, $s = s_0^*$. In the compatible regime the system can achieve both target area and perimeter, with a family of tilted polygonal shapes satisfying $s = s_0$, corresponding to the flat region in Figure 2.1(a,b). The smaller scale of the incompatible cell in Figure 2.1(c) reflects the compromise between area and perimeter costs resulting from $a < 1$ and $s > s_0$.

2.4 Linear Mechanical Response

Let us first consider a conventional elastic solid described by an energy $E(\mathbf{g})$ with a unique ground state $g_{0\mu\nu} = \delta_{\mu\nu}$ that provides the reference (undeformed) configuration. The mechanical response to a deformation is quantified in terms of the strain $\mathbf{u}$ which is defined as the deviation about the reference configuration, i.e. by writing $\mathbf{g} = \mathbf{g}_0 + 2\mathbf{u}$. Linear elasticity can then be formulated by expanding the energy around the reference

state to quadratic order in powers of the strain

$$E(\mathbf{g}) = E(\mathbf{g}_0 + 2\mathbf{u}) = \frac{1}{2} A^{\alpha\beta\gamma\delta}(\mathbf{g}_0) u_{\alpha\beta} u_{\gamma\delta} + O(\mathbf{u})^3 \ , \tag{2.6}$$

with $E(\mathbf{g}_0) = 0$. For an isotropic solid the elastic stiffness tensor $A^{\alpha\beta\gamma\delta}$ must have the form

$$A^{\alpha\beta\gamma\delta} = \lambda \mathbf{g}_0^{\alpha\beta} \mathbf{g}_0^{\gamma\delta} + \mu \left(\mathbf{g}_0^{\alpha\gamma} \mathbf{g}_0^{\beta\delta} + \mathbf{g}_0^{\alpha\delta} \mathbf{g}_0^{\beta\gamma} \right) \ , \tag{2.7}$$

and depends on only two independent degrees of freedom, namely the Lamé coefficients λ and μ. The various elastic moduli characterize the linear response to any deformation and can then be expressed in terms of λ and μ, according to the expressions given in the last column of Table 2.1.

Alternatively, one can bypass the Taylor expansion and directly calculate the energy cost for each specific deformation. This corresponds to tuning one or more of the components of $\mathbf{u}$ (denoted by δ), while leaving the others free to minimize the energy. For instance, a uniaxial deformation is imposed by fixing $u_{11} = \delta$ while leaving u_{12}, u_{22} free to adjust to minimize the energy. The deformation energy E_δ associated with the specific deformation δ then defines the corresponding elastic constant G according to

$$E_\delta = \min_{u_{\alpha\beta} \neq \delta} E(\mathbf{g}_0 + 2\mathbf{u}) = \frac{1}{2} G \delta^2 + \mathcal{O}(\delta^3) \ . \tag{2.8}$$

Of course the two procedures, i.e., the Taylor expansion and the calculation of the energy cost of specific deformations according to Eq. (2.8), are equivalent for a conventional elastic solid. Both routes show that the response to any deformation can be described in terms of only two independent parameters.

Howevere, the situation is quite different for the VM. To make this apparent it is useful to first consider the incompatible regime, where there is a unique ground state

configuration $g_{0\mu\nu} = c^2\delta_{\mu\nu}$, corresponding to a regular n-sided polygon. The constant c is determined by energy minimization and is the real solution of a cubic equation, given in App. 2.7 for $n = 3, 4, 6$. One may therefore be tempted to define the linear elastic response of the VM in the incompatible regime using the Taylor expansion of Eq. (2.4). Furthermore, since the reference configuration, i.e. $\mathbf{g}_0$, is isotropic, then so is the elastic stiffness tensor $A^{\alpha\beta\gamma\delta}$, which has the form given in Eq. (2.7) and is entirely determined by the two coefficients λ and μ, given by

$$\begin{aligned} \lambda &= \frac{\sqrt{3}}{4} + \frac{9r}{8c}(3s_0 - 7\ell) \ , \\ \mu &= \frac{9r}{8\ell}(3\ell - s_0) \ . \end{aligned} \tag{2.9}$$

A direct calculation of the deformation energy associated to a specific deformation, i.e., a path in $\mathbf{u}$ space, defines the associated elastic modulus G according to

$$\begin{aligned} E(\mathbf{g}) &= \min_{u_{\alpha\beta}\neq\delta} \left(\frac{1}{2}\left(a(\mathbf{g}_0 + 2\mathbf{u}) - 1\right)^2 + \frac{r}{2}\left(p(\mathbf{g}_0 + 2\mathbf{u}) - s_0\right)^2 \right) \\ &= E_0(\mathbf{g}_0) + \frac{1}{2}G(s_0, r)\delta^2 + \mathcal{O}(\delta^3) \ . \end{aligned} \tag{2.10}$$

The elastic constants calculated analytically with this second procedure agree well with the results of numerical simulations, as shown in Figure 2.2. They depend on the path taken in configuration space and cannot simply be expressed in terms of two independent parameters. In particular, they are not related to those of Eq. (2.9) obtained via Taylor expansion, which in turn do not agree with numerical simulations. This demonstrates that the VM energy is non-analytic near the incompatible ground state and a Taylor expansion does not apply.

In the compatible regime the ground state is degenerate, as shown in Figure 2.1(a), where the flat region corresponds to a continuous set of rest configurations [86, 123] or zero modes. This means that when subject, for instance, to a small uniaxial or

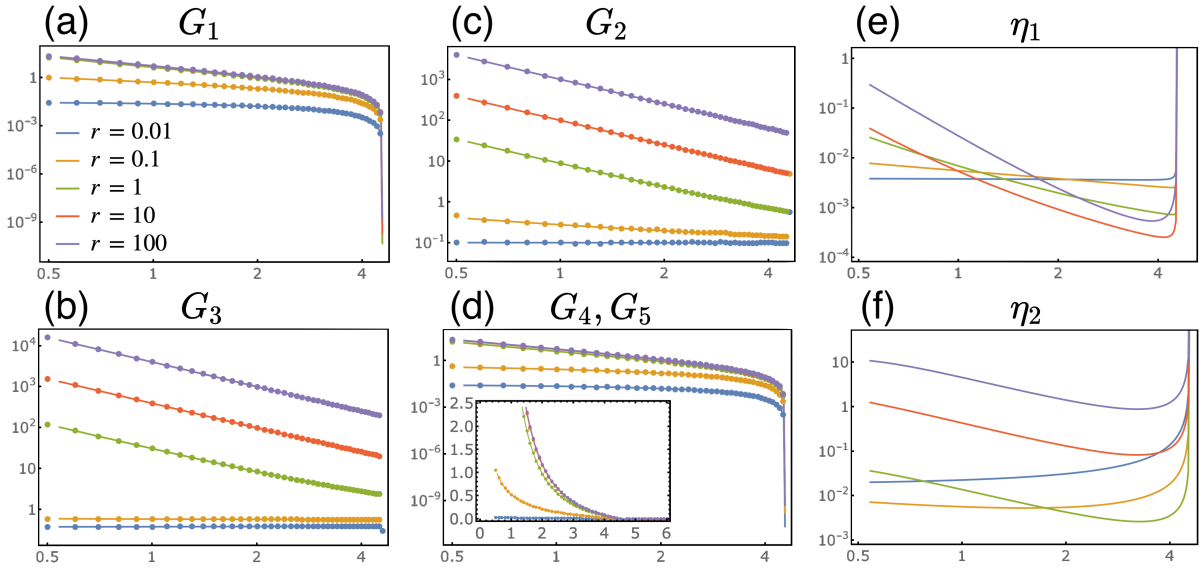

Figure 2.2—(a-d) Comparison of analytical (solid) and numerical (points) elastic moduli of an $n = 3$ VM as functions of target shape parameter s_0 on a log-log scale. The compatible/incompatible transition is at $s_0^* = 2\ 3^{3/4}$. The inset of (d) shows G_4 and G_5 on a linear scale, highlighting the vanishing of the measured response, beyond the critical shape parameter. The moduli were calculated for various values of rigidity ratio, ranging from $r = 0.01$ to $r = 100$. (e,f) Deviation from elasticity according to Eq.(2.11) as function of shape index for various values of the rigidity ratio r. For $r \gg 1$ perimeter deformations are more costly than area deformation and one observes significant deviations from conventional linear elasticity. The deviations are smaller in the opposite limit of $r \ll 1$, where the energy is dominated by the area term.

shear deformation, the system can accommodate the deformation by finding a new zero energy configuration corresponding to the deformed shape, resulting in vanishing elastic constant G. The elastic constants corresponding to a specific deformation can still be calculated using the procedure defined in Eq. (2.10) and vanish whenever the deformed state corresponds to one of the degenerate ground states. At sufficient finite strain the system will eventually be unable to accommodate the deformation by simply exploring the family of degenerate ground states, resulting in finite shear and uniaxial elastic constants above a critical strain.

Thus, we have shown that the linear response of the VM depends on the protocol of the deformation. For instance, the response to a uniaxial dilation/compression depends on whether or not we allow the system to also spontaneously shear during the deformation. This type of behavior has similarities with the odd elasticity of active solids [130], as both systems exhibit spontaneously induced shear in response to isotropic dilation/compression. In the next section we quantify the numerous ways in which the protocol-dependent linear VM elasticity differs from the linear elasticity of a Hookean solid.

Tissue Moduli				
	Deformation	Fixed	Free	Linear elastic solid
G_1	Uniaxial	u_{11}	u_{12}, u_{22}	$\frac{4\mu(\lambda+\mu)}{\lambda+2\mu}$
G_2	Uniaxial	$u_{11}=0, u_{22}$	u_{12}	$\lambda+2\mu$
G_3	Area	$u_{11}=u_{22}$	u_{12}	$4(\lambda+\mu)$
G_4	Shear	$u_{11}=-u_{22}$	u_{12}	4μ
G_5	Shear	u_{12}	u_{11}, u_{22}	4μ

Table 2.1: Elastic moduli for five different deformation protocols. The last column shows the expressions in terms of the Lamé coefficients λ and μ for the case of a linear elastic solid in $2D$, where μ is the shear modulus and $\lambda+2\mu$ the compression modulus.

2.5 Breakdown of linear elasticity

For bookkeeping purposes we define a set of elastic constants G_i, for $i = 1, ..., 5$, corresponding to the various deformation protocols as enumerated in Table 2.1. To quantify deviations from isotropic linear elasticity we define two dimensionless parameters, η_1 and η_2, given by

$$\begin{aligned} \eta_1 &\equiv \frac{G_3\, G_4}{4G_2\, G_1} - 1 \ , \\ \eta_2 &\equiv 1 - \frac{4G_2 - G_3}{G_4} \ . \end{aligned} \tag{2.11}$$

Both vanish identically for a linear isotropic elastic solid, where the different G_i's are related to one another as in Table 2.1.

In Figure 2.2 we plot η_1 and η_2 as functions of s_0 for various values of r. Here one sees systematic deviations from linear elasticity that diverge at the critical shape index. This shows that two measurements of mechanical response are insufficient to determine the response of the VM to generic deformations, and thus linear elasticity is an ill-defined approximation even for infinitesimal deformations. Thus unlike a conventional solid whose linear mechanical response can be characterized by two mechanical measurements, the VM requires, in principle, a measurement for each specific deformation.

To appreciate the deviation from conventional linear elasticity it is instructive to focus on the critically compatible case for a triangular polygon with $s_0 = s_0^*$. In this case the triangle is compatible, and there is only one configuration satisfying $a = 1$ and $p = s_0$ simultaneously, corresponding to an equilateral triangle. The associated ground state has zero energy and is unique.

We first calculate the response to area deformations by imposing $u_{11} = u_{22} = \delta$ and letting u_{12} be selected by energy minimization. Figure 2.3(a) shows the energy as a function of imposed area strain δ and shear strains u_{12}, with the blue curve indicating the

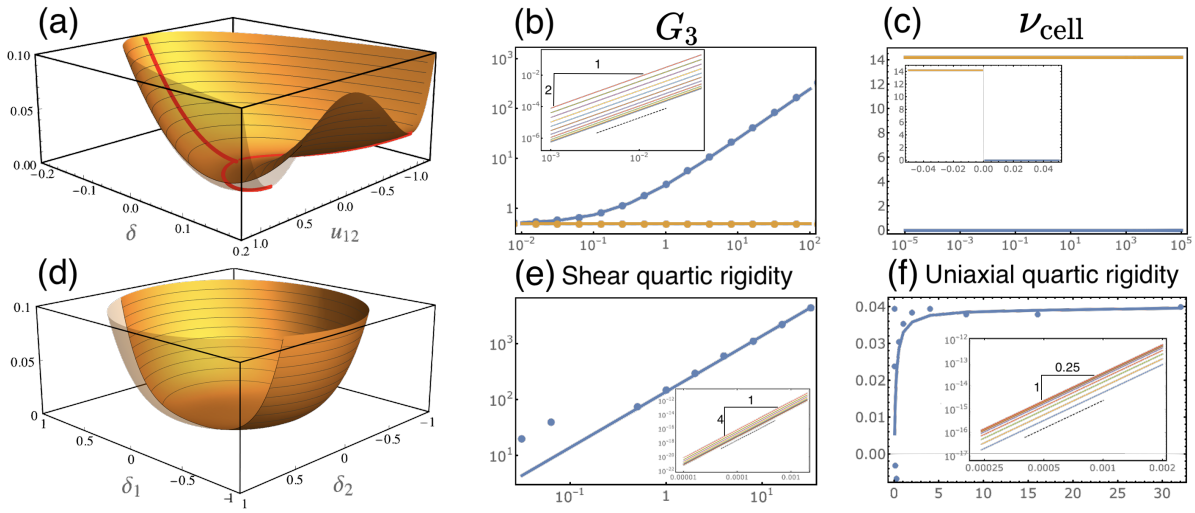

Figure 2.3—Energy landscape and mechanical properties of critically compatible triangular cell model. (a) Energy as function of imposed area and shear strains, showing an asymmetric response to area compression and tension. (b) Resistance to area deformation as function of rigidity ratio for tensile (blue) and compressive (yellow) area strain, compared with VM numeric results (dots). Inset shows the log-log plots of energy-strain curves. (c) The cell-ratio defined in (2.12) as function of rigidity ratio. Inset shows the cell ratio as function of imposed strain for a given rigidity ratio, confirming that it is well defined material property. (e) Energy landscape for area preserving deformations as function of the two shear strain modes, presenting a flat landscape with vansishing quadratic rigidity and finite quartic rigidity. (e) Quartic rigidity as function of rigidity ratio, with inset showing log-log plots of the energy-strain curves confirming the quartic dependence of energy in strains. (f) Quartic order rigidity as function of rigidity ratio (quadratic rigidity vanishes) compared with VM numeric results (dots). Inset shows the energy-strain curves on a log-log scale validating the quartic dependence of energy in strain.

energy minimizer for a fixed area deformation δ. We see that tensile deformations ($\delta > 0$) induce no shear while compression ($\delta < 0$) yields finite induced shear. The bifurcation of the red curve at the global minimum indicates spontaneous symmetry breaking in the shear response. The asymmetry of the response to area deformations is displayed in Figure 2.3(b) which shows G_3 as a function of the rigidity ratio r for compressive (yellow) and tensile (blue) deformations. The insets show log-log plots of energy-strain curves for the tensile case, validating the quadratic dependence of energy on strain.

To quantify the magnitude of the induced shear we define a measure analogous to the

Poisson ratio relating induced shear to imposed area deformation. The naïve measure u_{12}/δ is found to depend on the imposed strain δ and thus it is not a material property. Instead one may define the cell-ratio

$$\nu_{\text{cell}} = u_{12}^2/\delta \ . \tag{2.12}$$

This quantity is plotted in Figure 2.3(c) and captures the asymmetry between tensile and compressive deformations, with $\nu_{\text{cell}} = 0$ for tensile forces and $\nu_{\text{cell}} \neq 0$ for compressive forces. The inset of Figure 2.3(c) shows ν_{cell} for a specific r as a function of δ, confirming that this parameter is indeed a well defined material property independent of the magnitude δ. Importantly, the cell-ratio quantifies the coupling between bulk and shear deformations, which is absent in an isotropic linear elastic solid.

Next, we study the response to (area preserving) pure shear deformation by imposing $u_{12} = \delta$ and letting $u_{11} = -u_{22}$ to be selected by energy minimization, or vice versa. The plot of the energy as a function of the shear deformations shown in Figure 2.3(d) confirms that the two shear modes are decoupled as in classical elasticity. A log-log plot of the energy-strain curve for one shear mode and various values of r is shown in inset of Figure 2.3(e), revealing an inherently nonlinear quartic dependence that is in contrast to linear elasticity. The quartic rigidity is plotted in Figure 2.3(e) on a linear scale.

Finally, we test the response to a uniaxial strain and discover that, similar to the shear response, the quadratic rigidity vanishes and the response is quartic. The quartic rigidity is plotted as function of rigidity ratio in Figure 2.3(f) and the inset shows energy-displacement curves on log-log scale.

In summary, this section has shown how linear elasticity completely fails to describe the linear response of the VM to small deformations in both the compatible and the incompatible regimes. First, for $s_0 < s_0^*$ the assumption that the energy is analytic and

can be expanded as in linear elasticity leads to an isotropic elastic tensor that depends on two elastic moduli. Direct measurements of elastic response, both analytic and numeric, contradict linear elasticity and thus contradict the assumption that the elastic energy is analytic. At the critical point $s_0 = s_0^*$, the response to area deformations is asymmetric, violating reciprocity. Second, the response to shear deformations exhibits quartic rigidity, violating the superposition principle even for infinitesimal deformations. Finally, we uncovered an anomalous coupling between area and shear deformations, with a spontaneous breaking of symmetry in the shear response to isotropic dilations. This is reminiscent of the recently discovered odd-ratio that quantifies area-shear coupling in a generalized linear elasticity of active solids [130].

In the next section we explore the origin of the failure of linear elasticity using a visual representation of the problem. For that purpose we start with a representation of the classical elastic model using a triangular lattice of masses and springs and then implement the geometrical representation for the VM.

2.6 Visual representation of the failure of linear elasticity

2.6.1 Elastic triangle

To introduce the pictorial representation of deformations in configuration space we first consider a common microscopic model for elastic solids, which is a lattice of masses and springs. In $2D$ a triangular lattice of identical masses and springs leads, in the coarse-grained limit, to homogeneous and isotropic linear elasticity [55, 140]. As previously mentioned, the response to uniform loads on a uniform VM of identical triangular cells is equivalent to the response of a single triangle. Therefore we may consider a single

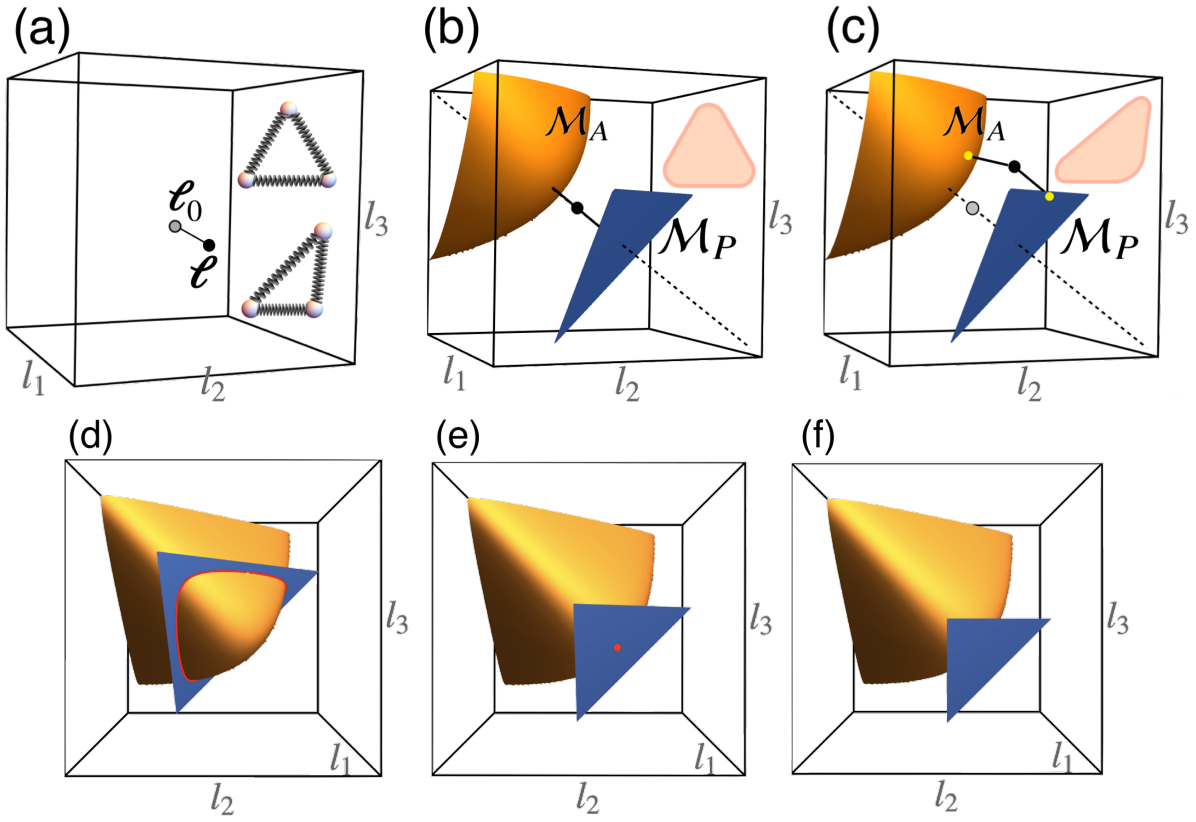

Figure 2.4—Visualizing elastic and cell models in configuration space. (a) An elastic triangle made of masses and springs. The rest and deformed configurations are marked by the gray and black points correspondingly. The mechanical energy is a measure for the distance of the configuration $\boldsymbol{\ell}$ from $\boldsymbol{\ell}_0$. (b) A triangular cell model with rest area and perimeter. $\mathcal{M}_P$ is the set of all configurations satisfying the rest perimeter and $\mathcal{M}_A$ is the set of all configurations satisfying the rest area. The black point is the energy ground-state with its exact position depending on the rigidity ratio. (c) a deformed triangular cell model, illustrating the content of the mechanical energy is measuring the joint distance from the two surfaces. The yellow points are hidden internal degrees of freedom that are selected to minimize the distance from $\mathcal{M}_P$ and $\mathcal{M}_A$. (d) Floppy cell with $s_0^* < s_0$: The intersecting curve represents a continuous set of triangles satisfying both P_0 and A_0 simultaneously. (e) Critically rigid cell with $s_0^* = s_0$ having one configuration that satisfy are and perimeter simultaneously. (f) $\mathcal{M}_A$ and $\mathcal{M}_P$ are disjoint, hence no triangle can satisfy both conditions and it is therefore frustrated.

triangle made of three identical masses and harmonic springs with rest lengths l_0. The rest configuration defines a point in configuration space, denoted by $\ell_0 = (l_0, l_0, l_0)$ and shown as a gray point with its associated equilateral triangle in Figure 2.4(a). An arbitrary deformed state is denoted $\ell = (\ell_1, \ell_2, \ell_3)$ and shown as a black point and associated deformed triangle in Figure 2.4(a). Deformation along the $\mathbf{n}_a = \frac{1}{\sqrt{3}}(1,1,1)$ direction correspond to area deformation, i.e., response to pressure changes, and deformations along the perpendicular plane spanned by $\mathbf{n}_1 = \frac{1}{\sqrt{2}}(1,-1,0), \mathbf{n}_2 = \frac{1}{\sqrt{2}}(0,1,-1)$ correspond to shear deformations. Deviations from the rest configuration cost energy proportional to $\delta\ell^2$, with $\delta\ell = \ell - \ell_0$. When expressed geometrically the rest and actual configurations can be represented by reference and actual (or induced) metrics $\mathbf{g}_0$ and $\mathbf{g}$, respectively, and the energy can be expanded in powers of $u = \frac{1}{2}(\mathbf{g} - \mathbf{g}_0)$ as in Eq. (2.6), with $A^{\alpha\beta\gamma\delta}$ as in Eq. (2.7). Importantly, the energetic response to a generic deformation along a given direction in configuration space is insensitive to the orientation, as expected from a quadratic expansion. In addition, there is no coupling between bulk and shear deformations; for example $A^{1112} = 0$.

2.6.2 VM triangle

I now implement the same visual representation described above for an elastic triangle for instead the case of a triangular VM cell, that is a triangle defined by its target area and perimeter. Contrary to the elastic triangle, the terms in the cell energy Eq. (2.1) penalize geometric deformations of area and perimeter, which do not uniquely determine a configuration of a triangular polygon. Instead, these geometric constraints target define two constraint surfaces in configuration space. The area term penalizes deviations from the target area, and identifies a $2D$ manifold of equal area configurations denoted by $\mathcal{M}_A$ and shown as an orange surface in Figure 2.4(b,c). The perimeter term penalizes

deviations from the target perimeter, which identifies a $2D$ manifold of equi-perimetric configurations $\mathcal{M}_P$ shown as a blue surface in Figure 2.4(b,c). The black point in Figure 2.4(b) represents the ground-state configuration that is achieved in the incompatible regime by balancing area and perimeter deviations. Contrary to classical elasticity which measures the distance of a point in configuration space from a reference point, the cell energy measures the joint distance from two target surfaces. This introduces additional hidden degrees of freedom to the deformations, as shown in Figure 2.4(c) where the energy of the deformed configuration (black point) is measured by selecting the closest (yellow) points on the target manifolds $\mathcal{M}_A, \mathcal{M}_P$.

The state of the tissue is determined by the relative location of the two surfaces in configuration space. In Figure 2.4(d-f) we show three different situations where the two surfaces cross each other along a curve, at a point, or not at all, corresponding to a floppy ($s_0^* < s_0$), critically rigid ($s_0^* = s_0$), and frustrated cell ($s_0 < s_0^*$), respectively. The ground-state is a point located along the $\mathbf{n}_a$ direction in between the surfaces, with its exact position depending on the rigidity ratio r: for $r \gg 1$ ($r \ll 1$) the cell is dominated by perimeter (area) term and the ground-state is closer to $\mathcal{M}_P$ ($\mathcal{M}_A$). Zero energy states exist only if the two surfaces intersect as in Figure 2.4(d,e). When the two surfaces are disjoint as in Figure 2.4(f), the joint distance of any point in space from the surfaces, that is the energy, is necessarily non-zero, reflecting the energy gap and the emergent rigidity of the cell.

Keeping this mind, it is then evident why a standard quadratic expansion of the energy relative to the ground-state, marked by the black dot in Figure 2.4(b), fails. Upon imposing an area preserving deformation, that is deforming the configuration perpendicular to $\mathbf{n}_a = \frac{1}{\sqrt{3}}(1,1,1)$, the energetic cost should arise directly from the perimeter term. Perimeter and area are, however, both conserved to linear order by a shear deformation, and the first non vanishing contribution comes from the quartic term in an expansion

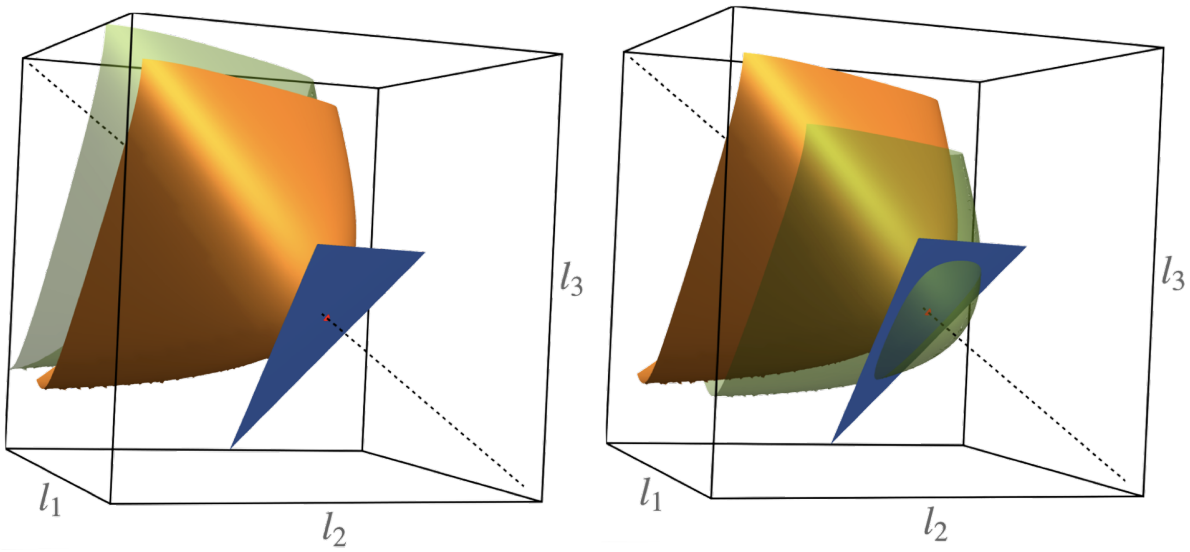

Figure 2.5—Area deformation in a critically rigid triangular cell. The rest surfaces $\mathcal{M}_A$ and $\mathcal{M}_P$ intersect at a point marked by red dot, forming the zero energy ground-state. Area deformation is imposed by constraining the configuration to lie on a different equi-areal surface. (a) Area tension - the equilibrium sits along the (1,1,1) direction in between the constraining green surface and the perimeter surface $\mathcal{M}_P$, thus remaining isotropic. The energy involves both area and perimeter deviations. (b) Area compression, leading to intersection of the constraining green surface with $\mathcal{M}_P$. The selected configuration is therefore on the intersecting curve with zero perimeter energy and induced shear strain.

in powers of the strain. On the other hand, area deformations costs energy already at quadratic order. Therefore, a direct calculation of the elasticity tensor leads to a zero shear modulus and finite bulk modulus, and the vanishing of the former fails to describe the linear mechanical response.

Another geometric visualization makes this argument more transparent. Given a deformed state ℓ we denote the ground-state by ℓ_0 and the closest points on $(\mathcal{M}_P, \mathcal{M}_A)$ by (ℓ_p, ℓ_a), marked by yellow points in Figure 2.4(c). Clearly, ℓ_p, ℓ_a are functions of ℓ. Linear elasticity, that is measuring the energy as the distance from ℓ_0, is equivalent to measuring the joint distance from $\ell_p(\ell_0), \ell_a(\ell_0)$. We note that an imposed shear deformation $\delta\ell$ corresponds to a displacement in configuration space parallel to the perimeter preserving surface $\mathcal{M}_P$. In this case, since $\mathcal{M}_P$ is flat, $\ell_p(\ell) = \ell_p(\ell_0) + \delta\ell$, that is the closest point on $\mathcal{M}_P$ is displaced to the same order as the deformation, thus contributing to the energy at the same order as the linear elastic contribution, and thus cannot be neglected. In other words, the failure of linear elasticity reflects the fact that $\mathcal{M}_P$ is flat.

The breakdown of linear elasticity is normally accompanied by breakdown of reciprocity, which in turn relies on the property of linear superposition of elastic fields [141]. In the VM, however, we find a stronger violation of linear elasticity and reciprocity that emerges from non-analyticity of the ground-state energy. To demonstrate this, assume a critically compatible triangle with target perimeter $P_0 = 3$ and target area $A_0 = \sqrt{3}/4$. The triangle in this case is compatible, and there is only one configuration satisfying A_0 and P_0 simultaneously: an equilateral triangle of edge length $l = 1$, with zero energy. In Figure 2.5(a,b) the orange and blue surfaces represent those set by target area and perimeter, and intersect at the single point corresponding to the ground-state. Now consider an infinitesimal area deformation. Area expansion corresponds to constraining the cell configuration to lie on the green surface in Figure 2.5(a). In this case the perimeter necessarily deviates from its target value, and the closest point on $\mathcal{M}_P$ remains

isotropic. In contrast, an area compression corresponds to the situation shown in Figure 2.5(b), where the green surface describing the deformed area and the target perimeter surface intersect, resulting in zero perimeter energy and finite degenerate area energy. Therefore the system spontaneously breaks the symmetry by selecting a deformed state corresponding to finite shear of fixed magnitude and arbitrary orientation. Furthermore, the resistance to area compression depends only on area rigidity whereas area tension depends on both area and perimeter rigidities. This is in complete agreement with the analytical and numerical results obtained in Figure 2.3.

Finally, the visual representation in Figure 2.5 clarifies why the definition of the cell-ratio given in Eq. (2.12) is independent of the imposed strain and therefore constitutes a material property. Figure 2.5(b) shows that the imposed area strain δ measures the translation of the green surface, and the induced shear strain is the distance between the undeformed state, marked by the red point, and the curve where the green surface and the blue manifold $\mathcal{M}_P$ intersect. For small δ the part of the green surface that intersect with $\mathcal{M}_P$ can be approximated as a spherical cup. The relation between its radius of curvature R, and the imposed and induced strains is

$$(R-\delta)^2 + u_{12}^2 = R^2 \tag{2.13}$$

and for small δ we get

$$\frac{u_{12}^2}{\delta} = 2R \equiv \nu_{\text{cell}} \ . \tag{2.14}$$

The cell-ratio quantifying the coupling between imposed area strain and induced shear strain is thus a geometric measure of the curvature of the surface$\mathcal{M}_A$. Numeric simulations and analysis confirm that this definition is well defined and independent of the imposed strain magnitude, as shown in Figure 2.3(c).

2.7 Summary and Discussion

In summary, this chapter has shown that the mechanical response of the VM to even infinitesimal deformations deviates qualitatively from linear Hookean elasticity. This deviation is not surprising in the compatible regime, where there is a continuum of degenerate ground states, but is most striking in the incompatible regime, where the VM has a single ground-state and responds elastically. In this case one may therefore expect Hookean elasticity to be a valid approximation for describing linear response. We have seen, however, that this is not the case.

In both compatible (floppy) and incompatible (solid) regimes the response of the VM to small deformations depends qualitatively on the protocol of the deformation. In the compatible/floppy phase small uniaxial stretches cost zero energy if the system is allowed to change shape by spontaneous shear, but cost finite energy when shearing is forbidden, thereby reflecting an anomalous coupling between bulk and shear deformations. The compatible/floppy state can therefore accommodate imposed strains with zero stress by spontaneous shear up to a critical value of the external strain.

In the incompatible/solid phase there is a single ground-state and the origin of deviation from linear elasticity is more subtle. To understand what drives this failure, we have developed a graphic representation of the mean-field of the VM that illustrates the existence of hidden degrees of freedom. This geometric representation shows that the elastic solid holds two distinct sets of reference configurations defined by two constraint surfaces (associated with target area and target perimeter) that may be either compatible or incompatible with each other. When compatible, the system is fluid in the sense that it can explore a manifold of degenerate zero energy states and accommodate deformations with no energetic cost, at least below a critical strain. When the two reference states are incompatible, the system is rigid and has a finite ground state energy determined

by the distance between the two sets of reference states that cannot be simultaneously accommodated. The existence of this finite energy or pre-stress provides a definition of geometric rigidity. Upon deformation, the system can adjust this relative distance, resulting in a nonlinear and nonreciprocal elastic response. The strongest deviation from linear elasticity occur at the critical point or critically compatible state, where the system has a single non-frustrated ground-state, yet reciprocity is violated, an anomalous coupling between bulk and shear deformations emerges, and quartic rigidity is observed in response to specific deformations.

This chapter has quantified the deviations from linear elasticity in both regimes by examining the linear response to various deformation protocols. We have shown that the analytical derivation of a linear elastic theory of the VM via Taylor expansion for small strains is inconsistent with a analytical direct calculation of the linear response and with numerical simulations.

In the present work, we have restricted ourselves to a mean-field theory that examines the linear response of the VM to spatially uniform deformations, where all cells respond in the same way. The identification of hidden degrees of freedom demonstrates that analyzing the response of non-uniformly deformed tissue, e.g., the response of the tissue to the contraction of a single cell, requires a generalized elastic framework. Importantly, it validates the formulation proposed in earlier work [86] by my collaborator, where he suggested that both the ground state and deformation of the VM can be captured by an energy functional that measures the joint distance of the geometric state of the system described by the metric tensor $\mathbf{g}$ from two sets of reference states quantified by metrics $\bar{\mathbf{g}}_A, \bar{\mathbf{g}}_P$,

$$E(\mathbf{g}) = \min_{\bar{\mathbf{g}}_A \in G_A} \min_{\bar{\mathbf{g}}_P \in G_P} \left(\frac{1}{2} \|\mathbf{g} - \bar{\mathbf{g}}_A\|^2 + \frac{1}{2} \|\mathbf{g} - \bar{\mathbf{g}}_P\|^2 \right) . \tag{2.15}$$

It was shown in [86] that this energy functional yields the rigidity transition and cap-

tures the response of the VM to uniaxial deformations. Recent work has additionally proved [123] that a rigorous coarse-graining of the discrete triangular VM converges yields the continuum model proposed in [86].

The relevance of the work detailed in this chapter goes beyond the scope of tissue mechanics in two main directions. First, this work provides a new route for the design of mechanical meta-materials with extreme properties. Specifically, the unusual mechanical properties of the tissue VM stem directly from the geometry of the reference surfaces in Figure 2.4. This suggests that one could design materials with extreme mechanical behavior by constructing a cellular network where each cell has a specific local energetic response, controlled by the geometry of the reference surfaces. Second, this work challenges the well-established paradigm in physics that response to small perturbations can be analyzed via a Taylor's expansion about the ground state, and that its failure can be corrected by taking into account higher orders terms, which lead to complex nonlinear physics. The VM provides a realization of a class of system where Taylor's expansion fails unless the reference states are incorporated as dynamical variables. This work suggests a new framework for formulating the elasticity of underconstrained system by describing them via quadratic energy functionals where the available (and possibly incompatible) reference states are incorporated as dynamical fields. The identification of ground states and elastic response then requires additional minimization with respect to such reference states.

The failure of linear elasticity raises questions about other properties of underconstrained elastic media, such as the interactions between structural defects and their role into tissue "melting". This work, together with the general framework proposed in Ref. [86], forms the basis for analyzing these question, which is reserved for future studies.

Appendix 4.A VM numerical simulations

To test the analytical results, my collaborator Michael Staddon simulated numerically a VM with a regular lattice of triangular cells, implementing the model in Surface Evolver [142]. Periodic boundaries are used to avoid boundary effects, with periodic lengths L_x, L_y and a shear length L_{xy} such that $(x, y) = (x + mL_x + nL_{xy}, y + nL_y)$, where m and n are integers. For a given shape index s_0 and rigidity ratio r we first find the ground state using a gradient descent method to minimize energy over the vertex positions and the periodic boundary lengths L_x and L_y, with $L_{xy} = 0$.

From this ground state, we calculate the tissue moduli G_i, $i = 1...5$, using the same procedures for u_{11}, u_{12}, and u_{12} (see Table 2.1). The periodic lengths are transformed as $L_x \to L_x(1 + u_{11})$, $L_y \to L_y(1 + u_{22})$, and $L_{xy} \to u_{12}L_y$. We then minimize energy under this strain by updating vertex positions and free strain parameters. The modulus G is then calculated as $E = E_0 + \frac{1}{2}G\delta^2$ where E is the mean energy per cell, E_0 is the ground state energy per cell, and δ is the strain magnitude. Unless otherwise state, a value of $\delta = 0.001$ is used. In Figure 2.6 we show the energy minimizing configuration of a unit cell before and after shear deformation.

Appendix 2.B Analytical calculation of ground states

It is instructive to display the calculation of the ground states for a quadrilateral ($n = 4$), where the isoperimetric ratio is $s_0^* = 4$. In this case the derivation is transparent and can be carried out analytically.

The metric tensor can be parametrized in terms of the (dimensionless) lengths ℓ_1 and ℓ_2 of opposite parallel sides of the quadrilateral and the angle θ between adjacent sides

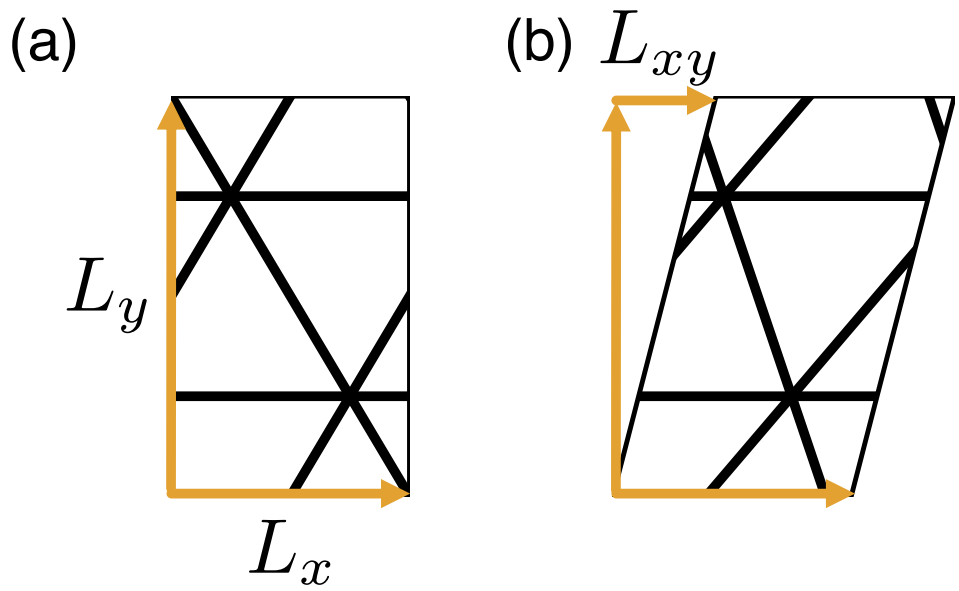

Figure 2.6—Numerical simulations. (a) Image of numerical simulations with no shear. The periodic boundary are defined by a parallelogram with horizontal length L_x and vertical length L_y. (b) Image of a sheared tissue, with shear length L_{xy}

as

$$g_{ij} = \begin{pmatrix} \ell_1^2 & \ell_1\ell_2\cos\theta \\ \ell_1\ell_2\cos\theta & \ell_2^2 \end{pmatrix} \tag{2.16}$$

with $p = 2(\ell_1 + \ell_2)$ and $a = \ell_1\ell_2\sin\theta$. We choose $0 \leq \theta \leq \pi/2$. Inserting this into the mean-field energy Eq. (2.4), we obtain

$$E = \frac{1}{2}\left(\ell_1\ell_2\sin\theta - 1\right)^2 + \frac{r}{2}\left(2(\ell_1 + \ell_2) - s_0\right)^2 . \tag{2.17}$$

The ground states are obtained by finding the metric that minimizes the energy. This gives three equations in three unknowns,

$$\begin{aligned} \frac{\partial E}{\partial \ell_1} &= \left(\ell_1\ell_2\sin\theta - 1\right)\ell_2\sin\theta + 2r\left[2(\ell_1 + \ell_2) - s_0\right] = 0 , \\ \frac{\partial E}{\partial \ell_2} &= \left(\ell_1\ell_2\sin\theta - 1\right)\ell_1\sin\theta + 2r\left[2(\ell_1 + \ell_2) - s_0\right] = 0 , \\ \frac{\partial E}{\partial \theta} &= \left(\ell_1\ell_2\sin\theta - 1\right)\ell_1\ell_2\cos\theta = 0 . \end{aligned} \tag{2.18}$$

Clearly the compatible state $a = 1$ and $p = s_0$ identically satisfies all three equations. This solution requires

$$\begin{aligned} \ell_1 \ell_2 \sin\theta &= 1 \ , \\ 2(\ell_1 + \ell_2) &= s_0 \ , \end{aligned} \tag{2.19}$$

with solution

$$\begin{aligned} \ell_1 &= \frac{s_0}{4} + \frac{1}{4}\sqrt{s_0^2 - \frac{s_0^{*2}}{\sin\theta}} \ , \\ \ell_2 &= \frac{s_0}{4} - \frac{1}{4}\sqrt{s_0^2 - \frac{s_0^{*2}}{\sin\theta}} \ , \end{aligned} \tag{2.20}$$

provided

$$\sin\theta \geq (s_0^*/s_0)^2 \ . \tag{2.21}$$

or $s_0 > s_0^*/\sqrt{\sin\theta}$. In other words for any value of $s_0 > s_0^*$ the compatible solution is a family of quadrilaterals with $a = 1$, $p = s_0$ and tilt angle θ varying in the range specified by Eq. (2.21). At $s_0 = s_0^*$ there is a single solution corresponding to a square with $\theta = \pi/2$ and $\ell_1 = \ell_2 = 1$.

When $\theta = \pi/2$, the last of equations (2.18) is identically satisfied. For $s_0 < s_0^*$ there is then a state with $\ell_1 = \ell_2 = \ell$ given by the solution of

$$\ell^3 + (8r - 1)\,\ell - 2s_0^* r = 0 \ . \tag{2.22}$$

This is the incompatible regime. There is a single ground state corresponding to a regular square and the energy is gapped. If $r \gg 1$, corresponding to the case where perimeter deformations are much more costly than area deformation, Eq. (2.22) has solution $\ell \simeq s_0/4$, corresponding to $p \simeq s_0$ and $a \simeq s_0^2/16$, with $p/\sqrt{a} \simeq 4 = s_0^*$. In the opposite limit of $r \ll 1$ we find $\ell \simeq 1$, corresponding to $a \simeq 1$ and $p \simeq 4$, with $p/\sqrt{a} \simeq 4 = s_0^*$. In general the compatible cell has $p > s_0$ and $a < 1$, with $p/\sqrt{a} = s_0^*$ for all $s_0 \leq s_0^*$.

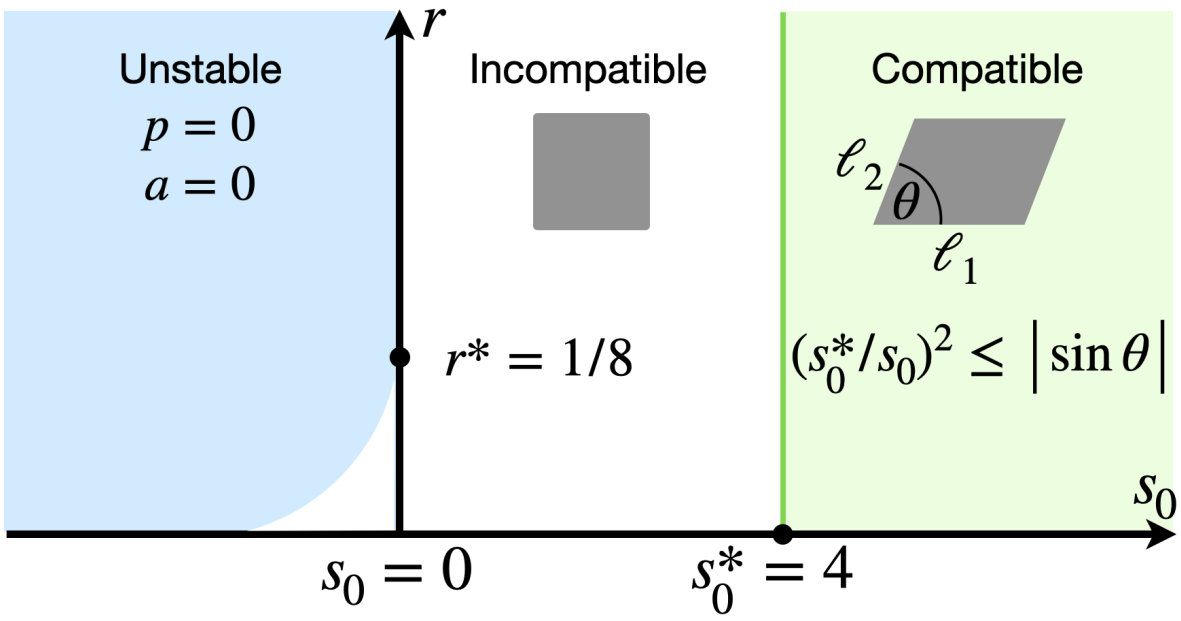

Figure 2.7—Mean-field phase diagram for a 4-sided VM in the (s_0, r) plane. For $s_0 > s_0^* = 4$ the ground state is compatible, corresponding to a family of zero-energy quadrilaterals parametrized by the tilt angle θ. At the critical point $s_0 = s_0^*$ there is a unique ground state corresponding to a square cell with $a = 1$ and $p = 4$. For $s_0 < s_0^*$ the system cannot satisfy both area and perimeter constraints and the ground state is a square with side determined by the real solution of the cubic equation (2.22). The incompatible regime extends into the region $s_0 < 0$ for $r < r^*$. The blue region corresponds to a collapsed cell with $a = p = 0$.

The solution $\ell = 0$ corresponds to a collapsed cell with $a = p = 0$ and minimum energy $E_m = (1 + r s_0^2)/2$. Imposing that $E(\ell) > E_m$, where ℓ is the solution of Eq. (2.22), yields the constraint $\ell > \ell_m$, with $\ell_m = 6 r s_0/(2 s_0^* r - 1) > 0$. Using this condition it can be shown that, as demonstrated in Ref. [45], the system is unstable, corresponding to a collapsed cell, for $r \leq 1/8$ and $s_0 < -\frac{2}{r}\left(\frac{1-8r}{6}\right)^{3/2}$. The corresponding phase diagram is shown in Fig. 2.7.

In general, one can calculate the incompatible ground state for any n-sided polygonal cell by noting that in this regime the ground-state metric is isotropic and can be written

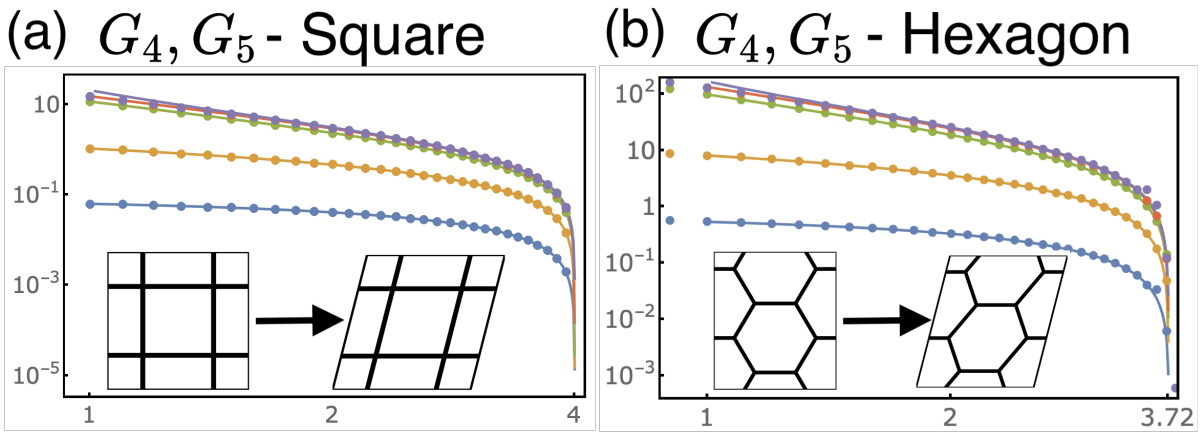

Figure 2.8—Extension of Figure 2.2 to square and hexagonal tissue model: Comparison of analytical (solid) and numerical (points) elastic moduli of an (a) $n = 4$ and (b) $n = 6$ VM as functions of target shape parameter s_0 on a log-log scale. The compatible/incompatible transition is at $s_0^* = 4$ and $s_0^* = 192^{1/4} \approx 3.72$ respectively.

as

$$\mathbf{g}_0 = \ell^2 \begin{pmatrix} 1 & 0 \\ 0 & 1 \end{pmatrix} \tag{2.23}$$

with ℓ to be determined by energy minimization. Upon substituting $\mathbf{g} = \mathbf{g}_0$ in Eq. (2.4), the energy E_n of an n-side cell reads

$$\begin{aligned} E_3 &= \frac{1}{2}\left(\frac{\sqrt{3}}{4}\ell^2 - 1\right)^2 + \frac{1}{2}r\left(3\ell - p_0\right)^2 , \\ E_4 &= \frac{1}{2}\left(\ell^2 - 1\right)^2 + \frac{1}{2}r\left(4\ell - p_0\right)^2 , \\ E_6 &= \frac{1}{2}\left(\frac{3\sqrt{3}}{2}\ell^2 - 1\right)^2 + \frac{1}{2}r\left(6\ell - p_0\right)^2 . \end{aligned} \tag{2.24}$$

The value of ℓ that minimizes the energy is the solution of a cubic equation given in

Eq. (2.22) for $n = 4$ and by the following equations for $n = 3, 6$

$$\begin{aligned} \ell^3 + \ell\left(96r - \frac{4}{\sqrt{3}}\right) - 32s_0 r = 0 \ , \quad n = 3 \ , \\ 9\ell^3 + \ell\left(24r - 2\sqrt{3}\right) - 4s_0 r = 0 \ , \quad n = 6 \ . \end{aligned} \tag{2.25}$$

The mechanical response to small perturbations relative to the ground state for a triangular VM is shown in Figure 2.2 where analytical and numerical results are compared and are in very good agreement. In Figure 2.8 one may compare numerical and analytical calculations of the shear modulus for square and hexagonal tissue VM.

Chapter 3

Non-affine linear response of the vertex model

This chapter is adapted from a 2023 Soft Matter article [143] co-authored with Michael Moshe, Michael Staddon, Mark Bowick, and M.Cristina Marchetti. Theoretical work was performed by Michael Staddon and myself, and simulations by Michael Staddon, with M. Cristina Marchetti, Mark J. Bowick, and Michael Moshe providing mentorship, manuscript editing, guidance, and support.

The linear elastic response of an ordered hexagonal vertex model to external deformations has been examined through calculations of the shear and bulk moduli [46, 68, 126]. Staple *et al.* [46, 126] evaluated the elastic moduli and first demonstrated the vanishing of the shear modulus in the compatible state of the vertex model, populated by a sea of freely deforming hexagons. A re-dressing of their work (within our context and notation) on the energy ground states for a hexagonal vertex model is given in Fig. 3.1. In chapter 2, we showed that the vanishing of both shear and Young moduli in the soft regime stems from the degeneracy of the compatible ground states, which allows the deformed tissue to spontaneously shear to a new compatible ground state to accommodate the external deformation [126]. We additionally discovered that the response is highly singular at the critical point demarcating the two regimes, with a breakdown of linear elasticity and anomalous coupling between compression and shear, as quantified by the development of a new elastic constant, the cell ratio [126].

The previous chapter and aforementioned studies only allow for affine deformations of the cells. This approximation can be viewed as appropriate for determining the short-time response of the vertex model to strain. The vertex model has, however, additional degrees of freedom and can relax stress by moving vertices in a non-affine way. Murisic *et al.* [68] incorporated these effects into a vertex model consisting of a uniform hexagonal cells by considering the hexagonal lattice as the union of two sub-lattices with a microscopic shift between them and found that the shear modulus is 2/3 softer than previously reported. Tong *et al.* [129] used simulations to measure the shear storage modulus and viscosity in both ordered and disordered model tissues.

In this chapter, we expand upon previous work by incorporating simple *non-affine* deformations in the single cell response. Using a mean field model for a hexagonal lattice, we derive analytic expressions for all the linear elastic moduli of the tissue, and verify these results using simulations. We show that, away from the critical point, the

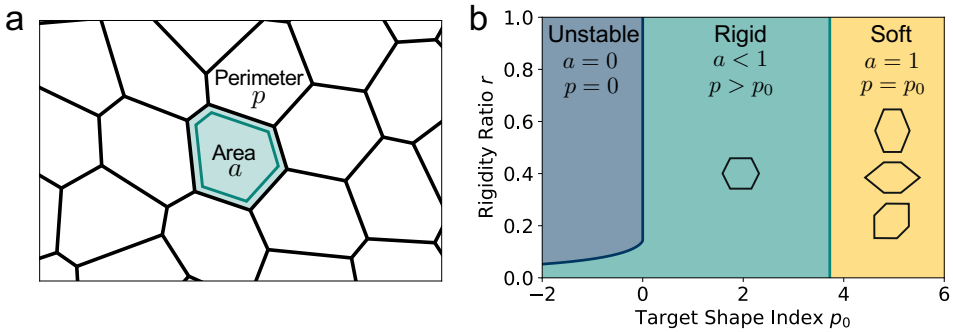

Figure 3.1—The vertex model for epithelia. (a) (a) The apical surface of an epithelium is modeled by a polygonal tiling, with each polygon representing a cell. (b) Vertex model phase diagram in the s_0, r plane. Within the blue region cells are unstable and collapse. Within the green region the tissue is in an incompatible state, with neither preferred perimeter nor area achieved, and the ground state is a regular hexagonal lattice. The tissue acts like a solid in response to shear. Within the yellow region both preferred perimeter and area are achieved and cells have a degenerate ground state and the tissue has zero shear modulus. The cell shapes show example energy minima, where a cell may elongate, increase its pointiness using the angle ϕ, or increasing its shear tilt angle θ as described in chapter 1 [126], in order to increase its perimeter while maintaining unit area.

elastic constants of a regular VM of hexagonal cells satisfy the standard relations of two-dimensional elasticity of isotropic solids. Despite this Hookean relationship, the mechanical linear response exhibits robust non-affine contributions that can significantly reduce the elastic constants, as known to happen in amorphous solids [144, 145, 146, 147]. For instance, the bulk modulus can be softer in the rigid state than in the soft fluid-like state and jumps discontinuously across the solid to fluid transition. We highlight several novel behaviors of vertex model elasticity, such as negative Poisson's ratio and a softening of the tissue as the ratio of cell area to perimeter stiffness increases. We verify our analytical results using numerical vertex model simulations of a regular tissue consisting of hexagonal cells.

The remainder of the chapter is organized as follows. In Section 3.1 we state the vertex model simulation and deformation protocol to extract various elastic constants. In Section 3.2 we introduce the VM and its mean-field implementation used in the present

work, and present a new derivation of the ground states that allows us to quantify the degeneracy of the compatible regime. In Section 3.3, after highlighting the distinction between the affine and non-affine deformations allowed in our model, we present results for all the elastic constants. We conclude in Section 3.4 with a brief discussion.

3.1 Vertex model: simulation and deformation protocol

3.1.1 The vertex model of epithelia

In this chapter we study the same vertex model as presented in chapter 1 (see Eq. (1.1)). We consider a hexagonal network (see Fig. 3.1) instead of a triangular one like in chapter 2. For the convenience of the reader, we briefly re-state the model and assumptions here.

Let before, we neglect topological rearrangements to focus on the role of geometry. Thus both our theory and simulations results correspond to a hexagonal polygonal tiling with fixed topology. We further simplify the model by assuming that all cells have the same preferred area $A_{\alpha 0} = A_0$ and all edges have the same tension $\Lambda_{ij} = \Lambda$. The interfacial energy can then be written in terms of the cell perimeter, $\sum_{\langle ij \rangle} \Lambda L_{ij} = \frac{1}{2} \sum_\alpha \Lambda P_\alpha$, where the factor of $\frac{1}{2}$ arises because the interfacial energy of each edge is shared by two cells. The tissue energy can then be recast in the form

$$E_{\text{tissue}} = \frac{1}{2} \sum_\alpha K(A^\alpha - A_0)^2 + \frac{1}{2} \sum_\alpha \Gamma(P^\alpha - P_0)^2 + E_0 \,, \tag{3.1}$$

where $P_0 = -\frac{\Lambda}{2\Gamma}$ is the preferred perimeter, and E_0 is a constant term obtained from completing the square. Since we care about the gradient of energy and not the absolute

value, we discard E_0 in the following.

Finally, we work in dimensionless units by normalizing the energy with KA_0^2 and lengths with $\sqrt{A_0}$. The dimensionless tissue energy is then given by

$$E_{\text{tissue}} = \frac{1}{2}\sum_{\alpha}(a^{\alpha}-1)^2 + \frac{1}{2}\sum_{\alpha} r(p^{\alpha}-s_0)^2, \tag{3.2}$$

where $a^{\alpha} = A^{\alpha}/A_0$, $p^{\alpha} = P^{\alpha}/\sqrt{A_0}$, $r = \Gamma/KA_0$ is the rigidity ratio, and $s_0 = P_0/\sqrt{A_0}$ is the target shape index of the cell.

3.1.2 Deformation Protocol

To numerically obtain the elastic moduli, we simulate the mechanical response of the vertex model under different deformations using a tissue of 4 hexagonal cells in a periodic box of lengths $L_x(0)$ and $L_y(0)$, and area $A(0) = L_x(0)L_y(0)$ determined by energy minimisation, and implemented in the Surface Evolver software [142]. For the incompatible regime, the ground state is a regular hexagonal cell. For the compatible regime, while the ground state is degenerate, we use a hexagon with 120° angles between edges and with the edge lengths determined by energy minimisation. First, we use an intermediate rigidity ratio of $r = 0.1$, and test the response across a range of preferred values of the target shape index, from $s_0 = 0$ to $s_0 = 4.6$, covering both the compatible and incompatible regimes.

To calculate the shear modulus, we deform the ground state (Fig. 3.2 top-left) by applying an initially affine deformation to vertices and the boundaries: $x_i(\epsilon) = (1 + \epsilon/2)x_i(0)$, $y_i(\epsilon) = (1 + \epsilon/2)^{-1}y_i(0)$, and $L_x(\epsilon) = (1 + \epsilon/2)L_x(0)$ and $L_y(\epsilon) = (1 + \epsilon/2)^{-1}L_y(0)$, where $\epsilon = 0.001$ (Fig. 3.2 top-middle). We then allow the vertex positions to relax to an energy minima (Fig. 3.2top-middle), and record the change in tissue energy δE before and after the deformation. The shear modulus is then numerically

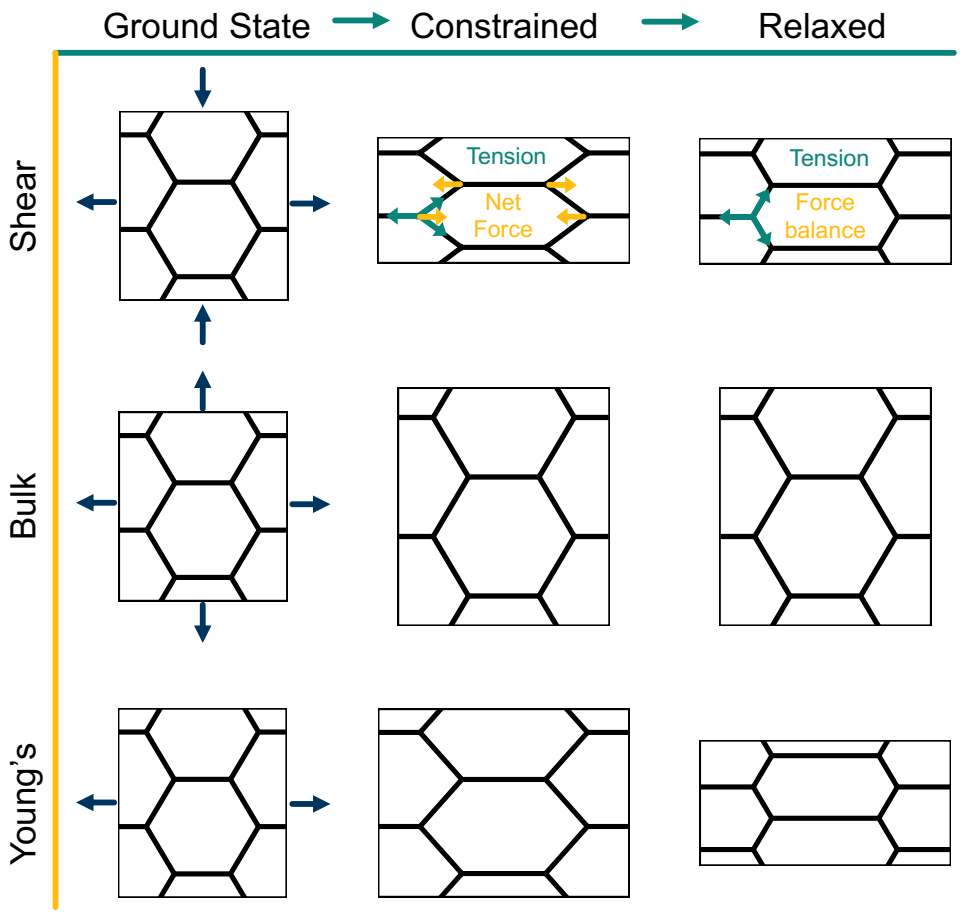

Figure 3.2—Strain protocols for measuring elastic moduli of the vertex model. (Top, Middle, Bottom) From the ground state, the periodic box lengths and vertex positions are transformed and constrained according to an affine transformation, shown by the arrows. From the constrained state, the system is relaxed according to tissue-scale or box constrained. (Top) The shear modulus is calculated by applying a shear transformation to the box. In the constrained state, every edge has the same tension, producing a net force on the vertices, hence this is not a force-balanced state. After relaxation, forces are balanced through a non-affine transformation on the vertices. During relaxation the box size is fixed. (Middle) The bulk modulus is calculated by applying an isotropic expansion to the box and vertices. During relaxation the box size is fixed. (Bottom) The Young's modulus and Poisson's ratio are calculated by applying a uniaxial strain to the box and vertices. During relaxation the height of the box may change and vertices may move.

estimated by $G = \frac{1}{A(0)} \frac{2\delta E}{\epsilon^2}$.

In the ground state of the incompatible regime, cell edges are under tension and meet at 120° angles. After the initial affine deformation, the angles change and the tissue is no longer in a force-balanced configuration (Fig. 3.2 top-middle). As we allow the tissue to relax, it responds with a non-affine deformation; vertices which are of the same y-coordinate alternate between moving left and moving right during relaxation, returning the angles between edges to a stable 120° configuration (Fig. 3.2 top-right). Such a deformation cannot be described by a single affine transformation, but rather by two affine transformations applied to different subsets of vertices [68].

To demonstrate the importance of this relaxation step, we report the response to two types of deformation protocols: (i) "constrained" deformations which are obtained where after deformation of the bounding box the cell vertices are not allowed to move to minimise the energy of the tissue, and (ii) "relaxed" deformations where the vertices are allowed to adjust their position to achieve force balance and the global tissue shape remains controlled by the geometry of the deformed box. Note that in the compatible regime the relaxed state can also be achieved by allowing the tissue to change its global shape [126], and the resulting linear elastic constants are the same.

For an intermediate rigidity ratio $r = 0.1$, we find that the shear modulus decreases as s_0 increases and becomes zero at the transition to the compatible regime. In particular, the relaxation step allows cells to decrease their perimeter, and thus energy, resulting in a relaxed shear modulus that is softer than in the constrained case (Fig.3.3a). In the compatible regime, the tissue is initially under no tension since the target perimeter is achieved. Upon straining the tissue, the perimeter increases and tissue energy increases. If tissue's cells cannot respond then the larger the initial perimeter, the higher the change, resulting in constrained shear modulus that increases with s_0. However, when the tissue is able to relax, the vertices move to reduce the perimeter until the target perimeter is

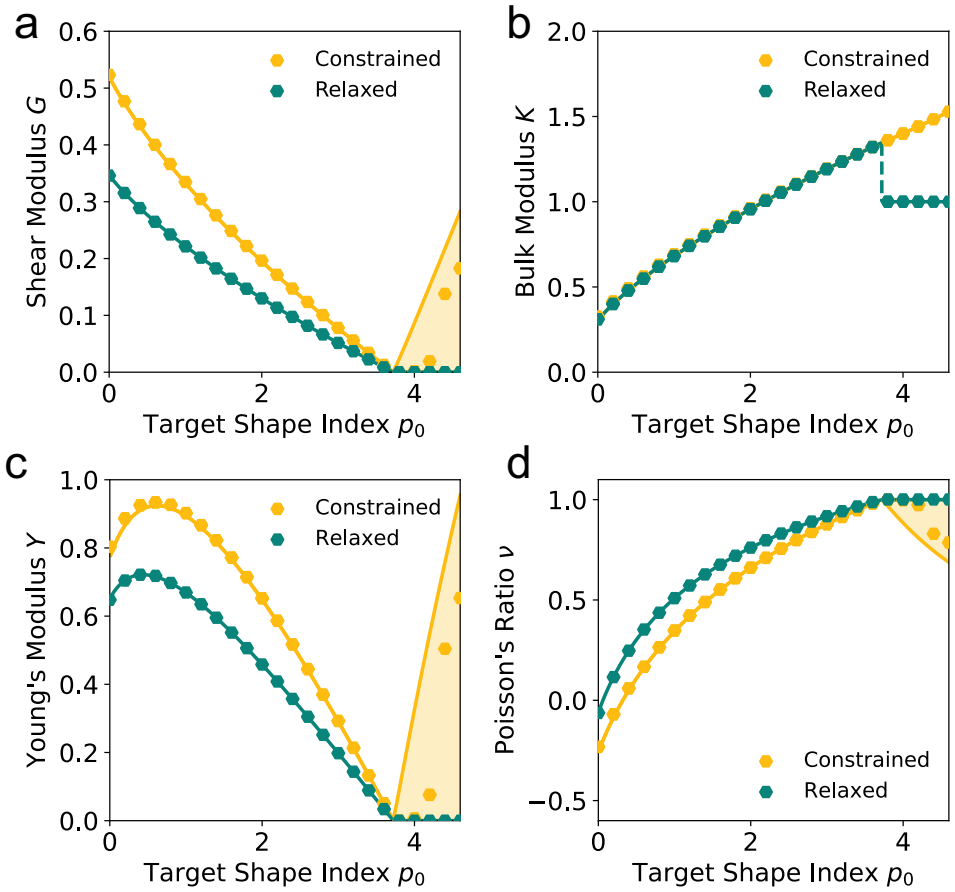

Figure 3.3—Non-affine deformations allow for a softer mechanical response. (a) Shear modulus G, (b) bulk modulus K, (c) Young's modulus Y, and (d) Poisson's ratio ν against target shape index s_0 for a rigidity ratio $r = 0.1$. The constrained values represent elastic moduli where vertices are constrained by the given deformation. The relaxed values lines represent the moduli allowing for non-affine deformations, where vertices may relax, subject to the boundary conditions. Dots represent simulated values. Lines represent analytic values. Shaded regions show the range of possible values in the constrained case, depending on the initial shape of the cells.

achieved again, allowing for the net energy to remain constant, leading to a zero shear modulus.

To calculate the bulk modulus, we apply the isotropic transformation $x_i(\epsilon) = (1+\epsilon)^{\frac{1}{2}} x_i(0)$, $y_i(\epsilon) = (1+\epsilon)^{\frac{1}{2}} y_i(0)$, and $L_x(\epsilon) = (1+\epsilon)^{\frac{1}{2}} L_x(0)$ and $L_y(\epsilon) = (1+\epsilon)^{\frac{1}{2}} L_y(0)$, where $\epsilon = 0.001$, such that $A(\epsilon) = (1+\epsilon)A(0)$. During the relaxation step, we allow the vertices to move, with the box lengths fixed. The bulk modulus is then given by $K = \frac{1}{A(0)} \frac{2\delta E}{\epsilon^2}$.

In the incompatible regime, force balance requires a constant 120° angle between edges, thus the tissue expands isotropically. We find that the bulk modulus increases as the target shape index s_0 increases, and is equal between the relaxed and constrained cases (Fig.3.3b).

In the compatible regime, the deformation initially increases the perimeter. During the relaxation step, the tissue responds in a non-affine way to restore its perimeter to its preferred value and so energy change only arises from the area term and we have a bulk modulus $K = 1$. Interestingly, this is lower than the bulk modulus in the incompatible regime just before the transition and thus, there is a discontinuity in the bulk modulus as s_0 passes the transition point. In contrast, the constrained case is unable to relax the cells' perimeters and so has a higher bulk modulus and does not exhibit the discontinuity (Fig.3.3b).

Next, we apply a uniaxial deformation to calculate the Young's modulus and Poisson's ratio: $x_i(\epsilon) = (1+\epsilon)x_i(0)$ and $L_x(\epsilon) = (1+\epsilon)L_x(0)$ (Fig. 3.1c). We then allow the vertex positions and box height $L_y(\epsilon)$ to relax to minimise energy. The Young's modulus is given by $Y = \frac{1}{A(0)} \frac{2\delta E}{\epsilon^2}$ and the Poisson's ratio by $\nu = -\frac{(L_y(\epsilon) - L_y(0))/L_y(0)}{(L_x(\epsilon) - L_x(0))/L_x(0)}$. Note that this definition of the Poison's ratio is equivalent to that in 2D elasticity and therefore its values are limited between $-1 < \nu < 1$. The extreme case $\nu = 1$ corresponds to incompressible system, analogous to the case of $\nu_{3d} = 0.5$ for incompressible 3D materials.

Again, the tissue undergoes a similar non-affine relaxation as under shear strain, reducing the Young's modulus compared to the constrained case (Fig. 3.3c). In this case, though, we find that the Young's modulus is non-monotonic. For s_0 close to zero, the Young's modulus increases as s_0 increases. For higher s_0, increasing s_0 further decreases the Young's modulus towards zero at the transition point, after which the Young's modulus is zero. However, in the constrained case the Young's modulus increases after the transition point due to the increased bulk and shear moduli. Interestingly, the Poisson's ratio is negative for small s_0 and increases towards a value of 1 as s_0 increases, before remaining 1 in the compatible regime (Fig. 3.3c). In the constrained case, the Poisson's ratio is actually lower than in the relaxed case for small s_0, in particular, in the compatible case the Poisson's ratio decreases as s_0 increases while for a relaxed tissue it remains 1.

This phenomena highlights the counter-intuitive nature of VM mechanics. In classical elasticity $\nu = 1$ corresponds to incompressible solids, commonly considered as very stiff. Here we find that the tissue approaches $\nu = 1$ for higher values of s_0 corresponding to compatible tissue with floppy response. This seeming contradiction is resolved by noting that in this limit cells can accommodate rest area and perimeter simultaneously and therefore upon deformation their area remains intact, just as in incompressible solids.

The simulations highlight the complex mechanical behaviour of the vertex model to applied tissue-level strains, both in its elastic moduli and the vertex-level non-affine deformations while relaxing the energy. The non-affine relaxation step allows the tissue to reduce its elastic moduli in the compatible regime. In particular, while the shear and Young's moduli are zero at the transition point, increasing p_0 increases the moduli in the constrained case, while they remain zero in the relaxed case. However, the simulations do not give an intuitive understanding for why the bulk modulus is discontinuous, or why we can get a negative Poisson's ratio. Thus, in the remainder of the paper, we develop

a mean-field theory of the vertex model that can account for non-affine relaxation of the tissue under strain to derive analytic expressions for the elastic moduli and understand the source of the complex phenomena mentioned above.

3.2 Vertex model: mean-field theory and ground states

3.2.1 Mean-field theory of vertex model

To understand the numerical results, we construct a mean-field theory by assuming that all cells responds equally. Additionally, we parametrize the non-affine pathway by which cells may respond to relax imposed deformations and by reducing their perimeter. Since all cells are assumed identical, the tissue energy is just $E_{\text{tissue}} = NE$ and one can simply consider the energy E of a single cell, given by

$$E = \frac{1}{2}(a-1)^2 + \frac{1}{2}r(p-s_0)^2. \tag{3.3}$$

Each cell consists of horizontal edges of length l_1 and diagonal edges of length l_2, with ϕ the angle between horizontal and diagonal edges (Fig. 3.4a). This parameterization captures the behavior of the tissue observed in our numerical simulations, where it is the angle between edges that changes during relaxation. Although cells have additional degrees of freedom, the description in terms of these three degrees of freedom is sufficient to capture the ground states of the tissue VM, and the response of the tissue under shear and bulk deformations in simulations (Fig. 3.2). To both examine the ground states and the response to deformation, it is convenient to parametrize each cell in terms of the height h and width w, as shown in Fig. 3.4a, given by

$$h = 2l_2 \sin\phi \ , \quad w = l_1 - l_2 \cos\phi \ . \tag{3.4}$$

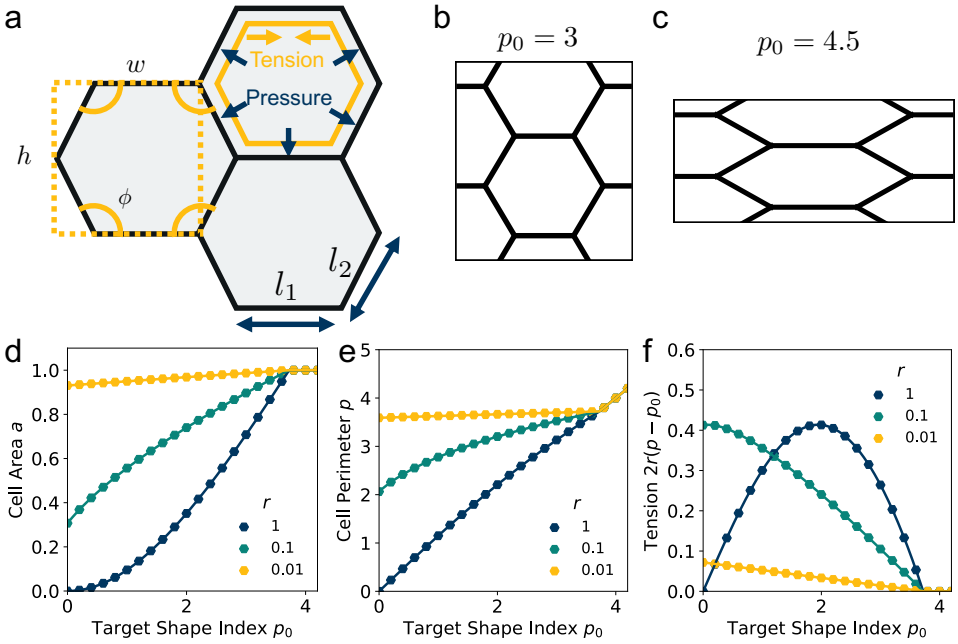

Figure 3.4—Shape parameterization of the vertex model and ground states. (a) Schematic of the vertex model and cell shape parametrization. Cells are defined by the lattice height h, width w, and angle between edges ϕ. (b) The ground state in the solid state is a regular hexagonal lattice, with $\phi = 2\pi/3$. (c) The ground state used in the soft state with $\phi > 2\pi/3$. (d - f) Cell area (d), cell perimeter (e), and edge tension (f) vs target shape index p_0 for various values of the rigidity ratio r. Dots represent simulated values, lines are the analytical results.

Each cell then contributes an area $a = wh$ to the tissue. We stress that the angle ϕ is distinct from the shear tilt angle θ introduced previously in chapter 2 [126], where cells may tilt or untilt in order to change their perimeter. While the shapes obtained from an initial regular hexagon by varying the shear tilt angle θ correspond to affine deformations of the hexagon, those parametrized by ϕ generally correspond to non-affine deformations of the regular hexagon. Inverting Eqs. (3.4), we obtain

$$l_1 = w + \frac{1}{2}h\cot\phi \,, \tag{3.5}$$

$$l_2 = \frac{1}{2}h\csc\phi \,. \tag{3.6}$$

Cell area and perimeter can then be written as

$$a = hw \,, \tag{3.7}$$

$$p = 2w + hf(\phi) \,, \tag{3.8}$$

where

$$f(\phi) = \frac{2+\cos\phi}{\sin\phi} \,, \tag{3.9}$$

resulting in an energy

$$E = \frac{1}{2}(hw-1)^2 + \frac{1}{2}r(2w + hf(\phi) - s_0)^2 \,. \tag{3.10}$$

This form makes it evident that the VM energy is underconstrained as area and perimeter do not uniquely determine cell shape.

3.2.2 Ground states

The ground state configurations are obtained by minimizing the energy with respect to the cell width w, height h, and angle ϕ and are solutions of the three coupled equations

$$\frac{\partial E}{\partial \phi} = hrf'(\phi)(2w + hf(\phi) - s_0) = 0 \,, \tag{3.11}$$

$$\frac{\partial E}{\partial h} = w(hw - 1) + rf(\phi)(2w + hf(\phi) - s_0) = 0 \,, \tag{3.12}$$

$$\frac{\partial E}{\partial w} = h(hw - 1) + 2r(2w + hf(\phi) - s_0) = 0 \,. \tag{3.13}$$

As shown in the previous chapter, we find a transition at $s_0 = s_0^*$ between two distinct states. For a regular lattice of n-sided polygons s_* is given by the isoperimetric value $s_0^*(n) = \sqrt{4n\tan(\pi/n)}$, with $s_0^*(6) = \sqrt{8\sqrt{3}} \approx 3.72$. The isoperimetric inequality $p \geq s_0^*(n)$ provides a lower bound on the perimeter of a regular n-sided polygon for given area [124]. For $s_0 > s_0^*(n)$ the cell is in a geometrically compatible regime, where both preferred area and perimeter may be achieved in the plane, and the tissue has zero shear modulus [46, 68, 86, 125] (Fig. 3.1b). For $s_0 < s_0^*(n)$ the cell is in an incompatible regime, where both preferred area and perimeter cannot be simultaneously satisfied, and the tissue behaves like a solid by resisting shear deformation [45, 86, 98, 126]. The corresponding ground state of the tissue is a lattice of identical hexagonal cells (Fig. 3.1b). As s_0 is further lowered the cell may become unstable and collapse to zero area and perimeter (Fig. 3.1b). Additionally, in a small range of parameters near the collapsing region more exotic ground states exist, with mixed lattices of square and octagonal, or dodecahedral and triangular cells providing lower energy than hexagonal cells [46].

Compatible State, $s_0 > s_0^*(6)$

For $s_0 > s_0^*(6)$ Eqs. (3.11) are identically solved by $hw = 1$ and $p = 2w + hf(\phi) = s_0$, and the zero ground state energy vanishes (Fig. 3.4c-e). We refer to this situation as the compatible state. The ground state configuration is a family of 6-sided polygons parametrized by the angle ϕ, with

$$h = \frac{s_0 \pm \sqrt{s_0^2 - 8f(\phi)}}{2f(\phi)} \,, \tag{3.14}$$

$$w = \frac{s_0 \mp \sqrt{s_0^2 - 8f(\phi)}}{4} \,, \tag{3.15}$$

where both roots are acceptable solutions for a given value of ϕ, corresponding to either tall and thin or short and wide cells. It is evident from Eq. (3.14) and Eq. (3.15) that such a solution exists provided $s_0^2 \geq 8f(\phi)$. The function $f(\phi)$ has a minimum at $\phi = \frac{2\pi}{3}$, with $f(\frac{2\pi}{3}) = \sqrt{3}$ corresponding to $s_0 = 2^{\frac{3}{2}}3^{\frac{1}{4}} = s_0^*(6)$. At this value of s_0 there is a single zero energy solution that corresponds to a hexagon of unit area. For $s_0 > s_0^*$ there is degenerate continuum of zero energy solutions corresponding to deformed hexagons of unit area, perimeter s_0 and $\phi \in \left[\frac{2\pi}{3}, \phi_m(s_0)\right]$, with ϕ_m determined by $s_0^2 = 8f(\phi_m)$ (Fig. 3.4c). There exist many other parameterizations that can give ground state shapes in the compatible regime, for example, cells becoming tall and thin, cells decreasing the angle ϕ to increase their perimeter, or cells tilting as in the previous chapter [126].

Incompatible State, $s_0 < s_0^*(6)$

For $s_0 < s_0^*$ the cell cannot simultaneously realize the target area and perimeter. We refer to this situation as the incompatible state. Eq. 3.11 requires $f'(\phi) = 0$, with solution $\phi = \frac{2\pi}{3}$, such that $f(\phi) = \sqrt{3}$. An intuitive explanation for this fixed angle is that all edges are under identical tension, and so by force balance a junction of three edges must

have equally spaced angles. Eqs. (3.12) and (3.13) then imply that $\sqrt{3}h = 2w$. This gives a perimeter $p = 4w$ and area $a = \frac{2}{\sqrt{3}}w^2 = p^2/8\sqrt{3}$, which means that the cells are regular hexagons in the incompatible state (Fig. 3.4b).

We can combine Eqs. (3.12) and (3.13) to obtain a cubic equation for the perimeter

$$p^3 + \left(\frac{r s_0^{*4} - 2 s_0^{*2}}{2}\right) p - \frac{r s_0^{*4}}{2} s_0 = 0 \,, \tag{3.16}$$

with $s_0^{*2} = 8\sqrt{3}$ and $a = p^2/s_0^{*2}$. The cubic equation can be solved perturbatively in the limit of low and high rigidity ratio r.

At low rigidity ratio, i.e., $r \ll 1/p_*^2$, we find

$$p = s_0^* - s_0^{*2}\left(\frac{s_0^* - s_0}{4}\right) r + \mathcal{O}(r^2) \,, \tag{3.17}$$

$$a = 1 - s_0^*\left(\frac{s_0^* - s_0}{2}\right) r + \mathcal{O}(r^2) \,. \tag{3.18}$$

The cell remains close in shape to a hexagon of unit area, with a reduction of the perimeter relative to the value p_* (Fig. 3.4d-e). The tension, given by $2r(p - s_0) = 2r\,(s_0^* - s_0) + \mathcal{O}(r^2)$, decreases monotonically as s_0 increases and vanishes at $s_0 = s_0^*$, where the cell reaches the compatible state and is under no tension (Fig. 3.4f). If s_0 becomes too small, the stable configuration collapses to a point with zero area and perimeter (Fig. 3.1b).

For high rigidity ratio, i.e., $r \gg 1/s_0^{*2}$, the perimeter and area can be expanded in inverse powers of r, with the result

$$p = s_0 + \frac{2 s_0}{s_0^{*2}}\left(1 - \frac{s_0^2}{s_0^{*2}}\right)\frac{1}{r} + \mathcal{O}\left(\frac{1}{r^2}\right) \,, \tag{3.19}$$

$$a = \frac{s_0^2}{s_0^{*2}} + \frac{4 s_0^2}{s_0^{*4}}\left(1 - \frac{s_0^2}{s_0^{*2}}\right)\frac{1}{r} + \mathcal{O}\left(\frac{1}{r^2}\right) \,. \tag{3.20}$$

In this limit the cell shape index is close to the target shape index (Fig. 3.4d-e). The

tension $2r(p - s_0) = \frac{4s_0}{s_0^{*2}}\left(1 - \frac{s_0^2}{s_0^{*2}}\right) + \mathcal{O}\left(\frac{1}{r}\right)$ is nonmonotonic in s_0, increasing from almost no tension at $s_0 = 0$ before decreasing as s_0 approaches s_0^* (Fig. 3.4f). As the rigidity ratio increases the tension saturates to the value $\frac{4s_0}{s_0^{*2}}\left(1 - \frac{s_0^2}{s_0^{*2}}\right)$, which has a maximum value of $2^{\frac{3}{2}}3^{-\frac{7}{4}} \approx 0.414$ at $s_0 = 8/\sqrt{3} \approx 2.149$ (Fig. 3.4d). For $s_0 \leq 0$, the cell collapses to a point with zero area and perimeter (Fig. 3.4b).

Finally, we note that when topological transitions are allowed, tissues may also unjam and undergo a solid-to-liquid phase transition when cell rearrangements cost zero energy. In disordered realizations of the VM, the unjamming transition occurs at $s_0 \approx 3.81$, a value close to, but slightly larger than $s_0^*(5)$ [48]. Intuitively, for the tissue to rearrange in a T_1 transition with zero energy barrier, two hexagonal cells must momentarily lose an edge and become pentagons while still maintaining their preferred perimeter and area. Cell motility can further promote fluidity and lower the transition point, as explained in Ref. [39].

3.3 Mechanical response of the vertex model

3.3.1 Deformations protocol

It is evident from Eq. (3.10) that area and perimeter (or equivalently height and width of the box shown in Fig. 3.4a) do not uniquely specify a polygonal shape. In the compatible regime there is a family of zero energy shapes corresponding to either tilted polygonal shapes obtained by affine deformations or non-affinely deformed polygons parametrized by the angle ϕ. In the incompatible regime, if only affine deformations are allowed, both the ground state and each deformed state are unique for fixed area and perimeter. Allowing non-affine deformations introduces, however, additional degrees of freedom that can lower the energy for a given set of parameters.

In the following we examine the response of a tissue initially in a ground state to an externally imposed strain. The deformation is imposed globally on the tissue by changing the shape of the bounding box. Such a deformation uniformly changes the shape of the cells and generally results in a state where individual vertices are no longer force balanced (Fig. 3.2 top-middle). We will refer to this state as the "constrained" deformed state. Due to the presence of hidden degrees of freedom the system can, however, lower its energy and relax to a state of local force balance. In the compatible regime this relaxation can occur via motion of the vertices that correspond to non-affine deformations (Fig. 3.2 top-right). In the compatible regime the relaxation can occur either via non-affine deformations with fixed box shape or through a global tilting of the tissue, which entails affine cell deformations, as previoulsy discussed in chapter 2. [126]. The elastic constants measured in the "relaxed" state of the compatible regime are the same for the two relaxation protocols.

Operationally, constrained deformations are achieved by first fixing either the cell height, width, or both, and then transforming the vertices according to the given deformation, as done in Staple *et al.* [46]. We prevent spontaneous tilting of the tissue, which, as discussed in chapter 2, can be used to soften the mechanical response using only affine deformations in the compatible regime [126].

We next evaluate the various elastic moduli of the vertex model. As we will see below, a new result of our work [143] is that in the incompatible regime cells can find new deformed states by relaxing through non-affine deformations (Fig. 3.2), resulting in a softer response than obtained in previous studies [46] (Fig. 3.3).

3.3.2 Shear Modulus

To calculate the shear modulus of the tissue, we apply an area-preserving pure shear deformation, corresponding to $w \to w(1+\epsilon/2)$ and $h \to h(1+\epsilon/2)^{-1}$, with ϵ the strain. We allow for a non-affine deformation to relax the tissue by minimising energy with respect to the angle ϕ for each value of strain (Fig. 3.4). The shear modulus is defined as

$$G = \frac{1}{a}\frac{\partial^2}{\partial\epsilon^2}\left(\min_{\phi} E\right)\Big|_{\epsilon=0} . \tag{3.21}$$

As area is preserved under pure shear, we only need to consider the energy cost due to changes in perimeter.

Compatible State, $s_0 > s_0^*$

In the compatible case, cells can accommodate shear and maintain their area and perimeter at the target values $a = 1$ and $p = s_0$ by changing shape, i.e., by adjusting the angle ϕ to a value other than $2\pi/3$. The perimeter of the deformed cell is given by $p(\epsilon, \phi) = 2w(1+\epsilon/2) + hf(\phi)/(1+\epsilon/2)$. The cell can maintain $p = s_0$ by deforming to a new compatible ground state corresponding to an angle ϕ^* given by the solution of $p(\epsilon, \phi^*) = s_0$. Clearly the energy remains zero, demonstrating that the shear deformation cost no energy and

$$G = 0 \tag{3.22}$$

for all rigidity ratios and $s_0 > s_0^*$ (Fig. 3.5a). This of course only holds up to a maximum value of strain determined by the angle $\phi_m(s_0)$. Beyond this value the fluid-like compatible tissue stiffens and acquires a finite shear modulus, as mentioned by [101], and recently by [125].

However, if the shape of the cell is constrained then applying a shear transformation

could increase the perimeter. To calculate the shear modulus under an affine transformation, we must consider the changes to the cell perimeter from its initial configuration. The shear modulus is defined by

$$G_{\text{affine}} = \frac{1}{a}\left.\frac{\partial^2 E}{\partial \epsilon^2}\right|_{\epsilon=0} = \frac{1}{a} r \left.\left(\frac{\partial^2 p}{\partial \epsilon^2}(p - s_0) + \left(\frac{\partial p}{\partial \epsilon}\right)^2\right)\right|_{\epsilon=0} . \tag{3.23}$$

and since for $\epsilon = 0$ we have $a = 1$ and $p = s_0$ this simplifies to

$$G_{\text{affine}} = r \left.\left(\frac{\partial p}{\partial \epsilon}\right)^2\right|_{\epsilon=0} . \tag{3.24}$$

Since an affine transformation also changes the angle between the edges, we must consider the effect of the transformation on each edge when calculating the change in perimeter. The length of the two edges shown in Fig. 3.4a change as

$$l_1(\epsilon) = l_1(0)\left(1 + \frac{\epsilon}{2}\right) \tag{3.25}$$

and

$$l_2(\epsilon) = l_2(0)\left(\left(1 + \frac{\epsilon}{2}\right)^2 \cos^2\phi + \left(1 + \frac{\epsilon}{2}\right)^{-2} \sin^2\phi\right)^{\frac{1}{2}}; \tag{3.26}$$

with first derivatives

$$\frac{\partial l_1}{\partial \epsilon} = \frac{1}{2} l_1(0) \tag{3.27}$$

and

$$\frac{\partial l_2}{\partial \epsilon} = \frac{1}{2} l_2(0) \frac{\left(1 + \frac{\epsilon}{2}\right)\cos^2\phi - \left(1 + \frac{\epsilon}{2}\right)^{-3}\sin^2\phi}{\left(\left(1 + \frac{\epsilon}{2}\right)^2 \cos^2\phi + \left(1 + \frac{\epsilon}{2}\right)^{-2}\sin^2\phi\right)^{\frac{1}{2}}}; . \tag{3.28}$$

Thus

$$\frac{\partial p}{\partial \epsilon}|_{\epsilon=0} = l_1(0) + 2 l_2(0)(\cos^2\phi - \sin^2\phi) \tag{3.29}$$

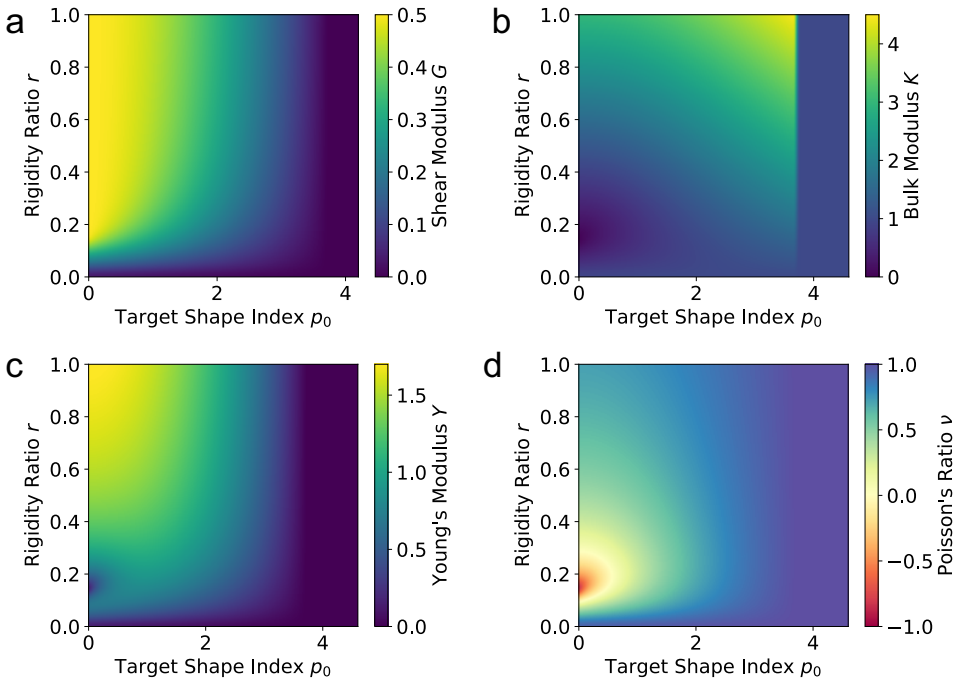

Figure 3.5—Elastic moduli of the vertex model. (a) Shear modulus, (b) bulk modulus, (c) Young's modulus, and (d) Poisson's ratio against target shape index s_0 and rigidity ratio r.

and

$$G_{\text{affine}} = r\left(l_1(0) + 2l_2(0)(\cos^2\phi - \sin^2\phi)\right)^2 \ . \tag{3.30}$$

The cell angle ϕ defines a family of solutions with $\sqrt{3} < f(\phi) < p_0^*/8$, as does the choice between the $\pm$ branch in our solution for cell height and, and so we obtain a range of values of the constrained shear modulus, and thus Young's modulus and Poisson's ratio, as ϕ is varied. We find that as p_0 is increased, the minimum shear modulus in the constrained case remains 0 while the maximum possible shear modulus increases (Fig. 3.3a).

Incompatible Case, $s_0 < s_0^*$

In the incompatible case cell edges are under uniform tension. By force balance, this implies that the angle between edges remains $\phi = \frac{2\pi}{3}$ even under small deformations

at the tissue scale. The ground state configuration is a regular hexagon with perimeter $p = 2w + \sqrt{3}h$. Using Eq. (3.24) and the relations for height and width in terms of the perimeter, $h = \frac{1}{2\sqrt{3}}p$ and $w = \frac{1}{4}p$, we obtain

$$G = \frac{r(p - s_0)p}{4a} \ . \tag{3.31}$$

In the rigid, incompatible state the shear modulus is a monotonically increasing function of r and vanishes at the transition $s_0 = s_0^*$ (Fig. 3.3a, Fig. 3.5a), in agreement with earlier results [68]. The non-affine deformations of the relaxed tissue allow for a softer response of the tissue, with the shear modulus being a factor of 3/2 stiffer when only considering vertices constrained by the affine shear strain [101, 46], as confirmed by simulations (Fig. 3.3a).

For small rigidity ratio ($r \ll 1/s_0^{*2}$), we can expand G in powers of r, with the result

$$G = \frac{1}{4}s_0^*(s_0^* - s_0)r + \mathcal{O}(r^2) \ . \tag{3.32}$$

The opposite limit of large rigidity ratio ($r \gg 1/s_0^{*2}$) yields

$$G = \frac{1}{2}\left(1 - \frac{s_0^2}{s_0^{*2}}\right) - \frac{1}{s_0^{*6}}\left(s_0^{*2} - s_0^2\right)^2 \frac{1}{r} + \mathcal{O}\left(\frac{1}{r^2}\right) \ . \tag{3.33}$$

3.3.3 Bulk Modulus

To calculate the bulk modulus, we change the area $a \to a(1+\epsilon)$ by rescaling the height $h \to h(1+\epsilon)^{\frac{1}{2}}$ and width $w \to w(1+\epsilon)^{\frac{1}{2}}$, and allow the angle ϕ to vary to minimize the deformation energy. The bulk modulus is then given by

$$K = \frac{1}{a}\frac{\partial^2}{\partial\epsilon^2}\left(\min_{\phi} E\right)\Big|_{\epsilon=0} \ , \tag{3.34}$$

with

$$\frac{\partial^2 E}{\partial \epsilon^2} = a^2 + r(p - s_0)\frac{\partial^2 p}{\partial \epsilon^2} + r\left(\frac{\partial p}{\partial \epsilon}\right)^2 . \tag{3.35}$$

To evaluate this expression we need to consider separately the compatible and incompatible states.

Compatible state, $s_0 > s_0^*$

We have previously shown that in the compatible case the angle ϕ can adjust to maintain a fixed cell perimeter under small deformations as dictated by local force-balance. Thus $\frac{\partial p}{\partial \epsilon}\big|_{\epsilon=0} = 0$ and $\frac{\partial^2 p}{\partial \epsilon^2}\Big|_{\epsilon=0} = 0$, and the bulk modulus is simply

$$K = 1 \tag{3.36}$$

for all r and $s_0 > s_0^*$ (Fig. 3.3b, Fig. 3.5b).

By contrast, if we allow for only affine deformations then the perimeter expands isotropically $p(\epsilon) = (1+\epsilon)^{\frac{1}{2}} p(0)$. In this case $\frac{\partial p}{\partial \epsilon}\big|_{\epsilon=0} = \frac{1}{2}p(0)$ and $\frac{\partial^2 p}{\partial \epsilon^2}\Big|_{\epsilon=0} = -\frac{1}{4}p(0)$, giving a bulk modulus equal to

$$K_{\text{affine}} = 1 + \frac{1}{4} r s_0^2, \tag{3.37}$$

which can be significantly higher than the non-affine result for high r, emphasising the need to consider non-affine displacements (Fig. 3.2).

Incompatible State, $s_0 < s_0^*$

In the incompatible state for $s_0 < s_0^*$ the angle that minimizes energy remains $\phi = \frac{2\pi}{3}$ for small perturbations to cell height and width to ensure tension balance at the cell vertices. The cell then expands isotropically, such that $p(\epsilon) = (1+\epsilon)^{\frac{1}{2}} p(0)$, resulting in

a bulk modulus

$$K = a + \frac{1}{4a} rps_0 \tag{3.38}$$

shown in Fig. 3.3b and Fig. 3.5b. We note that as s_0 approaches the critical value $s_0^*(6)$ from below, the bulk modulus has the value $\lim_{s_0 \to s_0^{*-}} \mathrm{K} = 1 + \frac{1}{4}\mathrm{r}s_0^{*2}$. On the other hand, in the compatible regime $K = 1$. Thus the bulk modulus exhibits a jump discontinuity at the critical point separating compatible and incompatible states. In contrast, if vertex positions are fixed by uniform dilation without relaxation, the bulk modulus is continuous and higher in the compatible region (Fig. 3.3b).

In the limit of low rigidity ratio ($r \ll 1/s_0^{*2}$), we find

$$K = 1 + \frac{1}{4} s_0^*(3s_0 - 2s_0^*)r + \mathcal{O}(r^2) \, . \tag{3.39}$$

The bulk modulus increases with s_0 up to the critical value, at which point it discontinuously jumps to 1 for all $s_0 > s_0^*$, independent of r. Interestingly, for $s_0 < \frac{2}{3}s_0^*$ the bulk modulus of the incompatible solid is lower than that of the compatible fluid, suggesting that contractility can actually reduce the bulk stiffness of the tissue. Additionally, increasing the rigidity ratio further reduces the bulk modulus for low s_0.

In the limit of high rigidity ratio ($r \gg 1/s_0^{*2}$), we find

$$K = \frac{1}{4} s_0^{*2} r + \left(\frac{3}{2} \frac{s_0^2}{s_0^{*2}} - \frac{1}{2} \right) + \mathcal{O}\left(\frac{1}{r} \right) \, . \tag{3.40}$$

Thus the bulk modulus increases with the rigidity ratio.

We find that for low s_0 the bulk modulus can be significantly lower in the rigid than in the fluid state, which can affect the rate of spreading monolayers [148]. This is due to the fact that at small p_0 cells have a smaller area while the energy required to deform

the cell is proportional to the square of the area change. Therefore it costs more energy to strain a single cell than to strain two cells with half the area, similar to the reduction in effective stiffness obtained when springs are placed in series.

The bulk modulus is also a non-monotonic function of the rigidity ratio. For small r the bulk modulus decreases with r as the size of the cell decreases, reaching a minimum near $r = 2/s_0^{*2} \approx 0.144$ before increasing linearly in r for high r, due to the growing contribution from the perimeter elasticity.

3.3.4 Young's Modulus and Poisson's Ratio

Next we calculate the Young's modulus and Poisson's ratio (Fig. 3.2 bottom row) by stretching the width of the cell $w \to w(1+\epsilon)$ while allowing the cell height h and angle ϕ free to minimize the energy. The Young's modulus is defined as

$$Y = \frac{1}{a}\frac{\partial^2}{\partial \epsilon^2}\left(\min_{h,\phi} E\right)\Big|_{\epsilon=0} \tag{3.41}$$

and the Poisson's ratio as

$$\nu = -\frac{1}{h}\frac{\partial h}{\partial \epsilon} = -\frac{w}{h}\frac{\partial h}{\partial w}. \tag{3.42}$$

To evaluate Y and ν we use the relationship between the linear elastic constants, $Y = \frac{4KG}{K+G}$ and $\nu = \frac{K-G}{K+G}$, which have been shown to hold away from the critical point.

Compatible state, $s_0 > s_*$

In the compatible state, the ground state degeneracy allows the cell to achieve the target shape index and area for small strain by reducing cell height and finding values of the angle ϕ different from $2\pi/3$, i.e., by changing its shape, with no energetic cost. As a

result for $s_0 > s_*$ we find

$$Y = 0 \ , \qquad \nu = 1 \ . \tag{3.43}$$

for all r (Fig. 3.3c-d, Fig. 3.5c-d). When constrained to affine only deformations, the Young's modulus can take a range of values from zero to a maximum value which increases with p_0, due to the increasing shear modulus. Similarly, the Poisson's can range from a maximum of 1 to a minimum value which decreases with p_0.

Incompatible case, $s_0 < s_*$

It has been shown that away from the critical point the elastic constants of the VM satisfy the familiar relation of linear elasticity of isotropic solids [126]. We can therefore use the relations $Y = \frac{4KG}{K+G}$ and $\nu = \frac{K-G}{K+G}$ to evaluate Y and ν in the incompatible regime, with the result

$$Y = (p - s_0)\frac{rp\,(4a^2 + rps_0)}{a(4a^2 + rp^2)} \ , \tag{3.44}$$

$$\nu = 1 - \frac{2rp(p - s_0)}{4a^2 + rp^2} \ . \tag{3.45}$$

We find that the Young's modulus is a non-monotonic function of both target shape index and rigidity ratio (Fig. 3.3c, Fig. 3.5c). The nonmonotonicity with s_0 is most pronounced at intermediate values of r, where at small s_0 the Young's modulus increases, rather than decrease, with increasing s_0.

At both high and low rigidity ratio, the Poisson's ratio remains close to 1 for all s_0, indicating that the cell preserves its area under deformations (Fig. 3.3d, Fig. 3.5d). At intermediate values of the rigidity ratio and small s_0, the nonmonotonicity of the Young's modulus results in a negative Poisson's ratio, which indicates that a tissue stretched in the x-direction, also expands in the y-direction.

In comparison to the constrained response, we find that the relaxed response gives a softer Young's modulus for all rigidity ratio and target shape index values, since the shear modulus is also softer by a factor of $\frac{2}{3}$ (Fig. 3.3c). Similarly, the Poisson's ratio is higher in the compatible state for all $s_0 < s_0^*$ (Fig. 3.3d).

In the limit of low rigidity ratio ($r \ll 1/s_0^{*2}$), the Young's modulus and Poisson's ratio are given by

$$Y = s_0^*(s_0^* - s_0)r + \mathcal{O}(r^2) \,, \tag{3.46}$$

$$\nu = 1 + \frac{1}{2}s_0^*(s_0 - s_0^*)r + \mathcal{O}(r^2) \,, \tag{3.47}$$

showing that when s_0 is increased towards the critical point from the solid side ($s_0 \to s_0^{*-}$) the Young's modulus vanishes and the Poisson's ratio increases towards 1.

In the limit of high rigidity ratio ($r \ll 1/s_0^{*2}$), we obtain approximate expression by expanding in $1/r$ as

$$Y = 2\left(\frac{s_0^{*2} - s_0^2}{s_0^{*2}}\right) + \mathcal{O}\left(\frac{1}{r}\right) \,, \tag{3.48}$$

$$\nu = 1 - \frac{4(s_0^{*2} - s_0^2)}{s_0^{*4}}\frac{1}{r} + \mathcal{O}\left(\frac{1}{r^2}\right) \,. \tag{3.49}$$

The Young's modulus also has a maximum value of 2 at $s_0 = 0$.

3.3.5 Origin of negative Poisson's ratio

We can understand why certain cell parameters give a positive or negative Poisson's ratio by looking at how the energy gradient with respect to cell height changes as we change the cell width. The gradient $\frac{\partial E}{\partial h}$ can be thought of as the effective force acting on

the height of the cell, given by

$$\frac{\partial E}{\partial h} = w(hw - 1) + \sqrt{3}r(2w + \sqrt{3}h - s_0). \tag{3.50}$$

In the ground state, this will be zero. Then, if we vary the cell width but keep the height fixed we can measure the change in force as

$$\frac{\partial^2 E}{\partial w \partial h} = 2hw - 1 + 2\sqrt{3}r. \tag{3.51}$$

When this value is positive, then as cell width is increased, the effective force acting on cell height increases and so the cell height will decrease as it relaxes to the energy minimum. Consequently, the sign of this value is the same sign as the Poisson's ratio.

The second term $2\sqrt{3}r$ comes from the perimeter contribution in the VM and accounts for energy changes due to perimeter elasticity. Since $p \geq s_0$, the cell is under tension and the perimeter term aims to shrink the cell. Increasing the width further increases the perimeter and so tension increases, providing more force to shrink the cell. Thus, the perimeter elasticity always acts to shrink the cell and contributes to a positive Poisson's ratio.

The first term, $2hw - 1 = 2a - 1$, represents the energy change due to area elasticity. We can write this as $2w(h - 1/2w)$, which we can think of as an spring like force with stiffness $2w$ and target height $1/2w$. As width increases, the height becomes closer to the target height, reducing the strain. At the same time, the effective stiffness $2w$ increases, increasing the pressure. Thus there is a trade off between less restoring force on the cell area versus increased effectiveness of changes in cell height. The net effect on whether this increases or decreases the perimeter depends on the size of the cell area: when cell area $a < \frac{1}{2}$ the area term acts to increase cell height when width is increased, and for

$a > \frac{1}{2}$ the area term reduces the cell height.

For high rigidity ratio, the perimeter term dominates and so an increase in cell width leads to a reduction in cell height. For low rigidity ratio, the area term dominates and the cell area is close to 1 (Fig. 3.4d), thus an increase in cell width reduces the area pressure and cell height decreases. However, in the intermediate regime for low s_0 cell area is small, meaning the area term acts to increase cell width, and the area contribution and perimeter contributions are of comparable size, resulting in negative Poisson's ratio.

We can calculate the transition to a negative Poisson's ratio exactly at $s_0 = 0$, which corresponds to the situation where the contribution to cell edge tension from cortical contractility and cell-cell adhesion precisely balance. In this limit the equation for the ground state perimeter, Eq. 3.16, becomes

$$p\left(p^2 + \frac{rs_0^{*4} - 2s_0^{*2}}{2}\right) = 0 \tag{3.52}$$

with solution

$$p = s_0^*\sqrt{1 - \frac{1}{2}rs_0^{*2}}\,. \tag{3.53}$$

$$a = \left(1 - \frac{1}{2}rs_0^{*2}\right) \tag{3.54}$$

for $r < 2/s_0^{*2} \approx 0.144$. For $r > 2/s_0^{*2}$ the cell is unstable and collapses to zero area. We can calculate whether cell height increases or decreases when width is increased by calculating how the effective force on the height, $\frac{\partial E}{\partial h}$, changes with width. Substituting our formula for area we find

$$\frac{\partial^2 E}{\partial h \partial w} = 1 - \frac{3}{4}rs_0^{*2} = 1 - 6\sqrt{3}r \tag{3.55}$$

where we have used $s_0^{*2} = 8\sqrt{3}$. Thus for $r > \frac{4}{3}s_0^{*2} \approx 0.096$ and $s_0 = 0$ the tissue has a negative Poisson's ratio.

3.4 Conclusions

This chapter focused on the linear response of the 2D vertex model consisting of a hexagonal polygonal tiling by calculating the shear modulus, bulk modulus, Young's modulus and Poisson's ratio, using a mean-field approach that allows for a class of non-affine deformations, which agree well with numerical simulations. Approximate expressions are provided in the limit of high and low rigidity ratio. These calculations match previous results showing a rigidity transition controlled by purely geometric effects and tuned by the target shape index s_0.

For cells in the incompatible case, $s_0 < s_* \approx 3.772$, the tissue has a finite shear modulus which decreases with s_0. For cells in the compatible case, $s_0 > s_0^*$, the shear modulus becomes zero for all s_0. However, when the tissue is constrained by the deformation protocol, the result is a stiffer mechanical response to shear in the incompatible case, and the compatible case can have a finite shear modulus, which depends on the initial configuration of the cells, and that increases with s_0. The constrained cases correspond to the elimination of cell shape zero modes.

The bulk modulus of the tissue increases with s_0 in the incompatible regime, and then has a jump discontinuity at $s_0 = s_0^*$, where it changes from a larger value in the solid state to a value of 1 in the fluid state. In the incompatible case, cells perimeters increase upon isotropic expansion of the tissue, but in the compatible regime cells can change shape to preserve their perimeter under small changes in area. However, this discontinuity is not observed when the tissue is constrained. Additionally, in the incompatible regime the bulk modulus can decrease below 1 for small rigidity ratio, r. This indicates that cell

contractility can reduce the stiffness of the tissue, resulting in a larger bulk modulus in the "soft" phase than in the "solid" phase.

Under uniaxial strain, we find the Young's modulus of the tissue can be non-monotonic with respect to s_0, initially increasing and then decreasing towards zero in the incompatible case. The Poisson's ratio can become negative for small s_0 and intermediate rigidity ratio, as cells can reduce their energy more by increasing their area through an orthogonal expansion, than by reducing their perimeter. Within the compatible regime, the tissue has zero Young's modulus and Poisson's ratio equal to one. However, when only constrained deformations are allowed the tissue can have a finite Young's modulus in the compatible regime, similar to the shear modulus.

The results of this chapter highlight the complex linear elastic behaviour that can arise from the simplest version of the vertex model due to its underconstrained nature. For simplicity, we have assumed that cells are regularly arranged and that we only have small strains. This analysis might be most applicable in tissues with a regular crystalline structure, such as the *Drosophila* pupal wing [100] However, it would be interesting to extend these sort of calculations to the case of disordered cell networks.

The principal take home message of this chapter is the importance of allowing for unconstrained degrees of freedom, in this case non-affine deformations, to relax the system and give a softer mechanical response to strain. The constrained case may be thought of as the short-time response of the tissue to strain, and the relaxed case as the long-time limit. Although the specific non-affine mechanical pathways presented here are unique to hexagons, an analogous non-affine mechanical mode is observed to be in disordered tissues such as Drosophila and are known as "isogonal modes" [53].

Finally, one should note that the emergence of rigidity observed in this work draws a direct link with the rigidity of mechanical frames and granular models, where mechanical stability occurs at critical coordination number, or at finite strains, and are normally

accompanied by a discontinuous jump in the bulk modulus. Nevertheless, the results of this chapter show that geometric incompatibility is a crucial ingredient that has to be taken into account for an estimation of the critical coordination number, and is left for a future work [149, 150].

In conclusion, the work in this chapter demonstrates that the vertex model, thought of as a collection of geometric constraints rather than a reference ground state structure, can engender interesting, tunable, linear mechanical responses. In particular, the linear response exhibits a strong non-affine contribution under uniaxial compression and shear, as well as a negative Poisson's ratio. Typically, these two phenomena in crystalline solids require special lattice constructions, whereas in the vertex model exotic mechanical response can be achieved by tuning the relative competition between area and perimeter constraints via r and geometric compatibility via the target shape index s_0.

Chapter 4

Nonlinear response and role of curvature in the vertex model

This chapter is adapted from a 2023 Soft Matter article [151] co-authored with Michael Moshe, Michael Staddon, and M.Cristina Marchetti. Theoretical work was performed by myself, and simulations by Michael Staddon, with M. Cristina Marchetti and Michael Moshe providing mentorship, manuscript editing, guidance, and support.

In the previous chapters we saw how individual cell shape can determine tissue scale mechanical proprieties via a mean field treatment of the vertex model. Furthermore, despite that the mean field approach neglects cell-to-cell rearrangements and tissue inhomogeneities, we found fairly good agreement with vertex model simulations which allow for individual cells to respond differently and also include a tissue boundary.

Importantly, the vertex model exhibits zero modes that exist at the level of a single cell. This is made more evident by assuming all cell edges have identical adhesion and contractility, the VM energy reduces to penalizing harmonic deviations away from a target area A_0 and target perimeter P_0 (see Eq. (2.1)).

In chapters 2 and 3 we utilized this shape degeneracy to parametrize mechanical pathways for a tissue to relax stresses from imposed deformations. These pathways could not be deduced based off the energy ground state configuration nor the polygonal tiling structure like in conventional elasticity. Instead, the degeneracy is reflected in the form of the energy and these pathways were inserted by hand and energy minimization with these "hidden" degrees of freedom.

In chapters 2 and 3 a careful study of the linear response of the VM to mechanical deformations was provided, and in general the mechanical response of the vertex model is well studied, for instance see Refs. [45, 46, 68]. However,the non-linear response relatively less so. Recent work showed that the VM exhibits shear-thickening in the compatible regime [125, 152]. In the same vein, this chapter presents a careful study of the non-linear elasticity of the VM under finite dilation and compression via a mean-field approach and simulations. Previously, in chapter 1, the onset of compatibility in the vertex model at s_0^* showed anomalous elasticity as reflected by an asymmetric bulk modulus under dilation and compression, as well as coupling between stretching and shear modes [122].

In this chapter, I show that the asymmetry of the bulk modulus continuously extends away from s_0^* under finite compression and dilation. In particular, the vertex model

exhibits a dilation-hardening for compatible tissues and a compression-softening of incompatible tissues for finite critical strain. The hardening (softening) nonlinear response to dilation (compression) is reflected by a jump (drop) discontinuity of the bulk modulus and is associated with the sudden lifting (onset) of zero-modes.

These results are of particular importance to systems that are residually stressed, such as cell layers with spatially varying cell geometry or curved tissue, where they may result in a shift of the critical s_0^*. In general, understanding the mechanisms through which tissues fine-tune their rigidity in response to areal re-scaling is relevant to several biological processes, such as tissue growth, shrinkage, response to applied deformations, and in particular to shape changes where 2D tissue layers spontaneously fold into 3D curved states [153, 154, 155]. In previous chapters a strong emphasis was made between the vertex model's rigidity transition at a critical target shape index s_0 and the isoperimetric inequality. The inequality is a purely mathematical statement about the limitations which space set on shape. Unlike Euclidean space which is scale invariant, curved spaces have a length scale associated with their curvature. In 2D surfaces embedded in 3D Euclidean space this is given by the radius of curvature. This breaks the scale invariance in the isoperimetric inequality. For instance, for closed curves on a sphere of radius R the inequality is modified to be [124]

$$s_0^{*2} - \frac{A}{R^2} \leq \frac{P^2}{A} \tag{4.1}$$

Under certain assumptions a version of this inequality exists for polygons on both positively and negative intrinsically curved surfaces. Numerical studies of the vertex model have confirmed that intrinsic curvature plays a role in the jamming and unjamming of cells [156, 54, 157], reflecting the inherently geometric nature of the model.

Based on insight from the planar 2D non-linear elasticity, this chapter utilizes the

mean field theory to predict how local compression/dilation due to intrinsic curvature shifts the transition between rigid and floppy states in curved tissue.

The organization of the chapter is as follows: in section 4.1 I introduce our mean-field VM, which describes 2D tissue elasticity at the single cell level. Section 4.2 outlines the calculation of the non-linear bulk modulus of the mean-field model and discusses simulation results. In section 4.3 I give a description of complementary numerical methods used to test our mean field theory. In section 4.4 I present a Landau energy argument to elucidate the connection between the asymmetry of the bulk modulus and the finite critical strain that controls the onset/lifting of zero-modes. Section 4.5 uses the results from mean field theory to predict the effective critical shape index for cells on a curved surface. I show that the prediction for the rigidity transition in curved geometry agrees well with numerical simulations by Sussman [156]. I conclude with a brief discussion in section 4.6.

4.1 Mean-field theory of ordered vertex model

As in chapters 2 and 3, the mean field theory considers a uniform regular 2D tiling where all cells respond identically to applied deformations. This approximation can capture the response of tissues subjected to uniform constraints or loads, and only relevant details of the set-up are briefly repeated here. Details of the mean field model are given in appendix 4.6, and the reader is advised to refer to Ref. [122] or chapters 1 and 2 for more details. The tissue energy is the sum of the energies of identical individual cells, and therefore the mean field approach reduces the VM to a single polygonal cell. All bulk tissue properties, such as elastic moduli, are calculated at the single cell level. The simulations are carried out for a lattice of regular polygons. For concreteness, simulations and mean field theory are for hexagonal cells unless stated otherwise. All results hold

analogously for other polygons.

Lengths are rescaled by $\sqrt{A_0}$ and the tissue energy per cell is rescaled by $\kappa_A A_0^2$, with κ_A the area stiffness, such that the energy per cell contains only two dimensionless free parameters and is given by

$$E = \frac{1}{2}(a-1)^2 + \frac{r}{2}(p-s_0)^2 \ , \tag{4.2}$$

where $r \equiv \frac{\kappa_P}{\kappa_A A_0}$ is the rigidity ratio, $s_0 \equiv \frac{P_0}{\sqrt{A_0}}$ the target shape index, and a and p are the actual area and perimeter of the cell.

To parameterize cell shape degrees of freedom, we work with a Cartesian coordinate system (X, Y) encompassing the cell with Y along the height, and X along the width, as shown in Fig. 4.1. The area and perimeter of a cell are purely geometric objects, and shape changes under various deformations can be computed given a transformation law.

Like before in chapter 3, externally imposed dilation and compression are implemented via an overall re-scaling of the cell's height h and width w via the transformation

$$w \to w(1+\epsilon) \ , \tag{4.3}$$

$$h \to h(1+\epsilon) \ , \tag{4.4}$$

with $\epsilon \in (-1, 1)$. In response to the strain, the cell may also spontaneously shear while maintaining the imposed rescaled area, as shown in Fig 4.1. This "tilt" is a self-shear parameterized as

$$w \to w + th \ , \tag{4.5}$$

$$h \to h \ , \tag{4.6}$$

where $t(\theta) \equiv \tan(\theta)$ parametrizes the shape degeneracy of cells. In addition, hexagonal

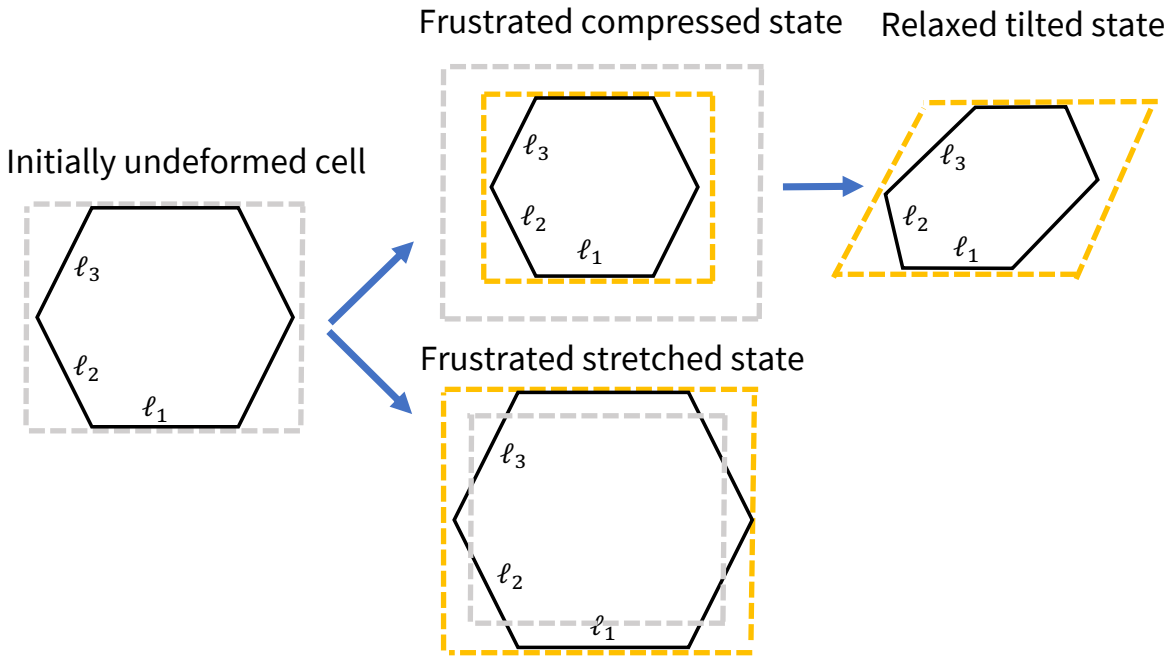

Figure 4.1—Under compression/dilation a cell may respond via a self-shear transformation by tilting either right or left. For example, at the rigidity transition, $s_0 = s_0^*$, both compression and dilation induce perimeter and area tension. Only under compression, however, cells can relax perimeter tension by changing shape, while simultaneously preserving area.

cells can also respond via non-affine deformations, which are known to reduce the shear and Young's moduli in the incompatible regime [143]. This study precludes non-affine pathways for cell response as previous work in chapter 2 showed that this approximation captures well the response to isotropic compression/dilation [122].

The deformed energy of an isotropically dilated or compressed cell is then given by

$$E(\epsilon, \theta; s_0, r) = \frac{1}{2}\left[\ell^2(1+\epsilon)^2 - 1\right]^2 + \frac{r}{2}\left[p(\epsilon, \theta, \ell) - s_0\right]^2 \ , \tag{4.7}$$

where $\ell(s_0, r)$ is the rescaled undeformed characteristic cell size (see appendix 4.6 for

details) and the deformed perimeter is

$$p(\epsilon,\theta,\ell) = \frac{\sqrt{2}\ell}{3^{3/4}}(1+\epsilon)\Bigg(2\sqrt{1+t(\theta)^2} + \sqrt{1+(t(\theta)-\sqrt{3})^2} + \sqrt{1+(t(\theta)+\sqrt{3})^2}\Bigg) . \tag{4.8}$$

If we set $\epsilon = 0$ and minimize with respect to θ we recover the results of Ref. [122]: the ground state energy is gapped for $s_0 < s_0^*$ and vanishes for $s_0 \geq s_0^*$, with a manifold of degenerate shapes, or zero-modes, parametrized by θ. To study the response to $\epsilon \neq 0$ we minimize θ as a function of applied strain in a manner analogous to our study of the linear response [122]. Formally, the energetic response is given by

$$E = \min_{\theta} E(\epsilon,\theta;s_0,r). \tag{4.9}$$

Because height and width are fixed by dilation/compression the energy minimization is 1D and corresponds to solving,

$$\left.\frac{\partial E}{\partial\theta}\right|_{s,r,\epsilon} = (p-s_0)\left.\frac{\partial p}{\partial\theta}\right|_{s_0,r,\epsilon} = 0 . \tag{4.10}$$

This equation has two solutions: either a cell utilizes shape degeneracy via θ so that the perimeter accommodates both dilation/compression *and* target shape index s_0, or the perimeter is totally set by dilation/compression with no tilt response. The relevant energy minimizing solution is a function of s_0, r and ϵ.

4.2 Nonlinear elasticity

The non-linear response under finite dilation and compression is characterized by the bulk modulus, defined as

$$K = \frac{1}{2a_{\text{cell}}} \left(\frac{\partial^2}{\partial \epsilon^2} \min_{\theta_{\min}} E(\epsilon, \theta; s_0, r) \right)_{s_0, r, \epsilon} \tag{4.11}$$

where $a_{\text{cell}} = \frac{3\sqrt{3}}{2}\ell^2$ is the rescaled cell area. Evaluating Eq. 4.11 at $\epsilon = 0$ yields the linear response, whereas a finite ϵ gives the non-linear response under finite strains. The minimization with respect to θ must be carried out before differentiation because the self-shear is implicitly dependent on ϵ via Eq. 4.10.

In the incompatible solid state, $(s_0 < s_0^*)$, we find that the mean field model and simulations exhibit a discontinuous drop in the bulk modulus at a critical compression. The discontinuity occurs due to a spontaneous self-shear of the cell which allows the perimeter tension to vanish. Conversely, under dilation the bulk modulus remains continuous as a function of strain, as shown in Fig. 4.2A. Increasing r shifts the critical strain to higher values, reflecting how a higher perimeter tension may support higher compression before giving way to spontaneous self-shear.

In the compatible floppy state, $(s_0 > s_0^*)$, the bulk modulus is continuous under any finite compression but exhibits a discontinuous jump at a critical strain upon dilation, as shown in Fig. 4.2B. At sufficient dilation, the zero-modes of the degenerate ground state are "exhausted", resulting in a frustrated and thereby rigid state. Unlike the incompatible state, the critical dilation is insensitive to r.

At the transition, s_0^*, both dilation hardening and compression softening are present for arbitrarily small strains, and reflect an asymmetry of the response to area rescaling. To quantify the asymmetry of the response, we show in Fig. 4.2C the difference between

dilation and compression bulk modulus ΔK as a function of s_0 for various values of the dilation/compression strain. For s_0 near the critical value, s_0^*, the asymmetry persists away from the critical point even for modest values of the strain (> 0.002). Note that the curve ΔK vs. s_0 is also not symmetric about the $s_0 = s_0*$ axis; this is due to the fact that the critical strain depends on r in the incompatible state, but not in the compatible state.

The origin of the bulk modulus discontinuity can be in part understood by writing the explicit expression for K obtained from Eq. 4.11

$$K = \frac{1}{2a_{\text{cell}}}\left[a^2 + r\big[p(\theta_{min}) - s_0\big]\frac{\partial^2 p(\theta_{min})}{\partial\epsilon^2} + r\left(\frac{\partial p(\theta_{min})}{\partial\epsilon}\right)^2\right]. \tag{4.12}$$

The contribution due to perimeter tension, $r\big(p(\theta_{min}) - s_0\big)$, in the solid phase vanishes if cells can accommodate target perimeter and imposed compression simultaneously via self-shear, resulting in a discontinuous drop of the bulk modulus. Conversely, in the floppy phase sufficient dilation will result in a sudden contribution from perimeter tension. In the following section, we formulate a Landau-type energy analysis to understand how dilation/compression can trigger or suppress zero-modes associated with shape deformation under dilation and compression.

4.3 Simulation protocol

My collaborator Michael Staddon performed numerical simulations of the deformation protocol in the incompatible regime ($s_0 < s_0^*(6)$) using a tissue of 4 hexagonal cells in a periodic box of lengths L_x and L_y. The cells consisted of regular hexagons with $l_1 = l_2 = l_3$ determined by energy minimization. This also determines the periodic box lengths. A strain of size ϵ is applied by mapping all vertex positions $x \to x(1+\epsilon)$ and

$y \to y(1+\epsilon)$ and the box $L_x \to L_x(1+\epsilon)$, $L_y \to L_y(1+\epsilon)$. After straining the system, the energy is minimized with respect to the vertex positions within the new box size. The measurement of the bulk modulus is defined as $K = \frac{1}{L_x L_y}\frac{2\delta E}{\epsilon}$, where δE is the change in minimum energy before and after strain. The simulations were performed with the Surface Evolver software [142].

4.4 Landau energy expansion

To understand how compression or dilation may trigger or lift shape degeneracy I treat θ as an order parameter for the onset of shape degeneracy. In other words, a finite θ signals that cells can adjust their shape to accommodate imposed strains, while $\theta = 0$ when cells remain rigid and do not change shape in response to external strain.

Upon expansion of the energy given by Eq. (4.7) in power of θ to quartic order one finds,

$$E(\epsilon, \theta; s_0, r) = E(\epsilon, s_0, r) + \frac{\alpha}{2}\theta^2 + \frac{\beta}{4}\theta^4 + \mathcal{O}(\theta^6) \,, \tag{4.13}$$

where

$$\alpha = 3\sqrt{3} r \ell_\epsilon \left(\ell_\epsilon - \frac{s_0}{s_0^*(6)} \right) \,, \tag{4.14}$$

$$\beta = \frac{107\sqrt{3}}{32} r \ell_\epsilon \left(\ell_\epsilon - \frac{89}{107}\frac{s_0}{s_0^*(6)} \right) \,, \tag{4.15}$$

and $\ell_\epsilon \equiv \ell(1+\epsilon)$. Minimization of this approximate θ^4 energy gives two solutions: (i) $\theta_{\min} = 0$ for $\alpha > 0$, and (ii) $\theta_{\min} = \pm\sqrt{\frac{|\alpha|}{\beta}}$ for $\alpha < 0$. The Landau expansion highlights the role of strain ϵ as tuning parameter between the cell responding with $\theta_{\min} = 0$ or by spontaneously tilting via a shear of $\theta_{\min} = \pm\sqrt{\frac{|\alpha|}{\beta}}$. The form of α reflects an asymmetric

response between compression versus dilation. From α one can extract the critical strain, ϵ_*, which controls the onset/lifting of shape degeneracy.

$$\epsilon_* = \frac{1}{\ell}\frac{s_0}{s_0^*(6)} - 1 \tag{4.16}$$

The vanishing of the critical strain at the critical shape index coincides with the the failure of linear elasticity for any applied strain [122]. Note that the expansion implies a tricritical point. Specifically, $\beta < 0$ occurs around the transition point $s_0 \approx 3.72$ either for large compression of $\epsilon \approx -0.17$, or for smaller strains deep in the floppy/compatible regime, around $s_0 \approx 4.47$. However, the Landau expansion considered here only considers a single pathway, via θ, by which cells may respond to moderately imposed strains. To handle larger deformations one would need to increase the expansion and/or incorporate other affine and non-affine pathways of cell-level response. Thus $\beta > 0$ defines the limits for which the above expansion is valid.

In the compatible regime $\ell = 1$ because target area is always achieved. Additionally, ϵ_* is independent of the rigidity ratio r. Whereas in the incompatible regime ϵ_* depends on r through ℓ.

We input the cell response via $\theta_{\min}$ into the energy and expand in powers of strain ϵ.

$$\begin{aligned} E(\epsilon; s_0, r) =& \min_\theta E(\epsilon, \theta; s_0, r) && (4.17)\\ =& \min_\theta E(\epsilon, s_0, r) + \frac{\alpha}{2}\theta^2 + \frac{\beta}{4}\theta^4 + \mathcal{O}(\theta^5, \epsilon^3) && (4.18)\\ =& E_0 + \frac{1}{2}\left(\frac{\partial^2 E(\theta_{\min})}{\partial \epsilon^2}\right)\epsilon^2 + \mathcal{O}(\epsilon^3)\ . && (4.19) \end{aligned}$$

In the final line the harmonic coefficient contains contributions from θ which reduce the overall response of the tissue. If we do not minimize over θ before expanding in ϵ, the resultant deformed energy does not incorporate the self-shear response due to cell shape

changes. A summary of the consequences of the additional degree of freedom θ on the

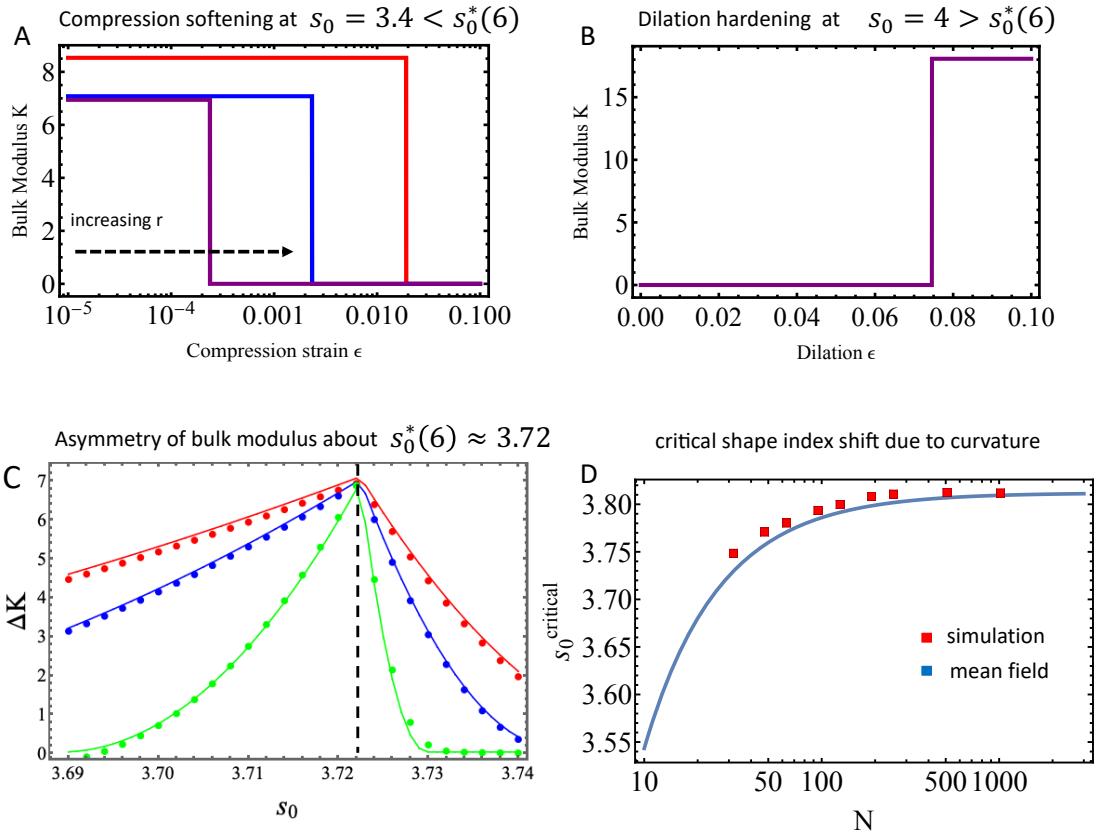

Figure 4.2—Panel A shows the mean field non-linear bulk modulus versus compressive strain in the incompatible regime for $r = 1, 10, 100$. A sudden discontinuous softening occurs at a critical strain ϵ_*. Panel B shows the hardening of the mean field bulk modulus at a critical dilation in the compatible regime. Note that in the incompatible regime ϵ_* depends on r and is thereby sensitive to the balance between perimeter and areal elasticity, whereas in the compatible regime, the critical strain is only a function of the shape index. Panel C compares the mean field model (solid line) to simulation (dots) and shows the difference in the linear response between dilation and compression for strain magnitudes $\epsilon = |0.01|, |0.006|, |0.002|$ in red, blue and green, respectively. The the asymmetry of the response decays continuously away from the critical shape index. Panels A,B, and C corresponds to hexagons. Panel D shows the effective critical shape index for a random tiling of N cells on a sphere of radius $R_{\mathcal{G}} = \sqrt{\frac{N}{4\pi}}$. The mean field prediction is for pentagons, whereas the simulation data are for a disordered VM taken from Ref [156].

response are as follows: In the incompatible regime, the $\theta_{\min} = 0$ solution corresponds to

a linear response in the solid state (see Fig. 4.4), whereas $\theta_{\min} = \pm\sqrt{\frac{|\alpha|}{\beta}}$ corresponds to the softer renormalized nonlinear response at critical compression strain. On the other hand, in the compatible regime, the linear response is always given by $\theta_{\min} = \pm\sqrt{\frac{|\alpha|}{\beta}}$ which allows the perimeter tension to vanish. The hardening under finite dilation occurs at a critical dilative strain ϵ_* and corresponds to a switch from $\theta_{\min} = \pm\sqrt{\frac{|\alpha|}{\beta}}$ to $\theta_{\min} = 0$, resulting in a higher response. This hardening phenomena is due to the cell's inability to access degenerate ground states to accommodate large dilation.

4.4.1 Strain dependent critical shape index

So far the mean-field model has predicted how compression (dilation) controls the onset (lifting) of shape degeneracy. The rigidity of the solid is defined by the absence of zero modes at the single-cell level. Therefore the mean field treatment suggests that dilation and compression shift the rigidity transition of the vertex model.

The shifted critical shape index is determined by the condition $\alpha(s_0, \epsilon) = 0$. Solving for s_0 yields a simple linear relationship between the effective critical point and strain

$$s_0^{\text{critical}} = s_0^*(n)\ell(1+\epsilon) \,, \tag{4.20}$$

where we used the modified version of Eq. 4.14 for n-gons (see appendix 5.C). Note that the absence of rigidity does not mean absence of residual stresses, as area tension may still be finite. This is reminiscent of the simultaneous existence of zero-modes and states of self stress [158], as well as the simultaneous onset of soft modes and geometric frustration [159, 160]. From Eq. 4.20 we construct a phase diagram in Fig. 3 showing how both tuning target shape index and imposed areal strain can control the onset of rigidity.

Until now we have discussed the effect of finite strains on the value of the effective

critical shape parameter, regardless of the origin of areal strain. One possible source of strain that is highly relevant to biological tissue is the formation of local intrinsic curvature, as is the case in bronchial epithelial tissue and early stage embryos [153]. A simple toy model to understand the effect of curvature is a two-dimensional spherical tissue model. The sphere radius may induce effective tension or compression on cells depending on their total preferred area which may be smaller or larger than $4\pi R^2$. Simulations of the vertex model constrained on a sphere have in fact reported that the rigidity transition signaled by the critical target shape index is sensitive to curvature with s_0^* shifts depending on curvature magnitude and relative cell size [156].

In the rest of this chapter, I examine the effective dilation/compression induced by curvature. This is done by calculating the cell area on a curved surface relative to its flat counterpart, and define the difference between the two to set an effective areal strain. Utilizing Eq.4.20, one may then predict the critical target shape index for solid-liquid transition of curved 2D tissues.

4.5 Rigidity transition in the presence of curvature.

The mean field treatment is extended by pertubatively calculating cell area on surfaces of constant curvature in powers of $\mathcal{G}R_{\text{cell}}^2$, where $\mathcal{G}$ is the Gaussian curvature, and R_{cell} the cell radius. Regular polygons of fixed radius (defined as the distance of the centroid to a vertex) differ in area depending on the surface on which they are embedded. The mismatch in area between curved and flat cells engenders an effective strain.

All geometric information of a surface M is encoded in its metric tensor $\mathbf{g}$. For a general shape/cell on a surface, $D \subset M$, the area is defined as

$$A = \int_D \sqrt{\det g} d^2x \tag{4.21}$$

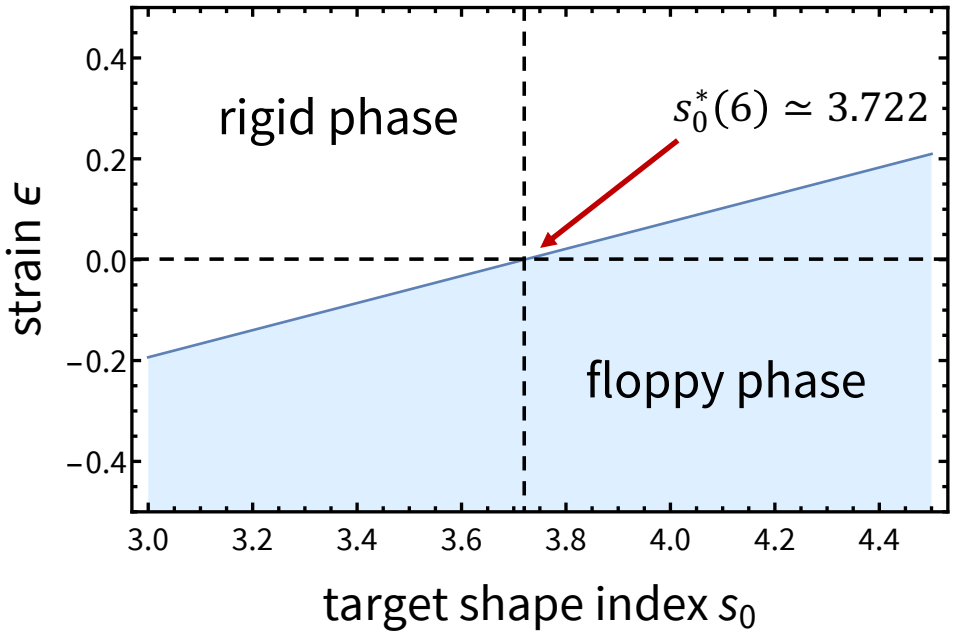

Figure 4.3—Phase diagram detailing how both target shape index and imposed compression/dilation control the floppy-rigid transition for hexagons as described by Eq. 4.20 for rigidity ratio $r >> 1$.

In this presentation it is clear that the determinant of the metric serves as a weight which accounts for the local compression/dilation between points. Unlike the planar setting of the mean field model where the surface's metric is trivial, i.e. $g_{ij} = \delta_{ij}$, the metric on curved surfaces - even uniformly curved - is not homogeneous but instead is a function of space. Nonetheless, the surface metric always admits a local expansion in *normal coordinates*, (x_0, x^i) which are defined by the condition that geodesics can be locally parameterized as straight lines, i.e. $\gamma(\lambda) = (x^1\lambda, x^2\lambda)$. In these coordinates, a series expansion of the surface's metric in powers of curvature yields

$$\det(g) = 1 - \frac{\mathcal{G}}{3}|x|^2 + \mathcal{O}(|x|^3). \tag{4.22}$$

The expansion reflects how variations of the metric are tied to curvature, and is locally approximated as flat with higher order corrections. The derivation of Eq. 4.22 is given

in appendix 5.A.

In following calculation I restrict attention to surfaces of uniform curvature - constant $\mathcal{G}$ - and hence only consider flat, spherical, and saddle-like surfaces. Of course, real curved biological tissues are not uniform either due to boundary conditions or heterogeneities. The approximation is controlled by the dimensionless geometric parameter η set by the radius R_{cell} of the cell over the radius of curvature $R_{\mathcal{G}}$, $\eta \equiv \frac{R_{\text{cell}}}{|R_{\mathcal{G}}|}$, where $\mathcal{G} \equiv \pm\frac{1}{R_{\mathcal{G}}^2}$. Thus the mean field approach will hold best for tissues with moderate curvature or relativity small cells.

Area of cells on curved surfaces

Upon series expansion of the surface's metric, the cell area to quadratic order is given by,

$$\begin{aligned} A &= \int_D \sqrt{\det g} d^2x \\ &\approx \int_D d^2x - \frac{\mathcal{G}}{6}\int_D |x|^2 d^2x \ , \end{aligned} \tag{4.23}$$

The first term yields the flat cell area. The calculation may be generalized to n-sided polygons for easy comparison of various tilings. To parameterize the polygonal n-sided cell D one may decompose it into 2n triangles about the centroid as illustrated in Fig. 4.4. Details are given in Appendix 5.B. To quadratic order the area is

$$A = \bar{A}\left(1 - \frac{\mathcal{G}}{12}R_{\text{cell}}^2 f(n) + \mathcal{O}(R_{\text{cell}}^4)\right) \ , \tag{4.24}$$

where $\bar{A} = nR_{\text{cell}}^2 \cos\left(\frac{\pi}{n}\right)^2 \tan\left(\frac{\pi}{n}\right)$ is the area of the cell on a flat surface, and $f(n) \equiv \cos^2\left(\frac{\pi}{n}\right)\left(\frac{2}{3} + \frac{1}{3}\sec^2\left(\frac{\pi}{n}\right)\right)$. In the limit of either very small cell size or very small curvature, the cell area reduces to the flat case.

In the limit $n \to \infty$ the first correction yields $\frac{\mathcal{G}}{12}\pi R_{\text{cell}}^2$, which reproduces the classical result of Bertand-Diguet-Puiseux on the area comparison of 2D geodesic discs of radius R_{cell} between curved and flat spaces [161].

4.5.1 Shift of the rigidity transition

From Eq.4.24 and the form of the deformed area term in Eq. 4.7 we may write the induced dilation/compression strain set by curvature as

$$\begin{aligned}\epsilon_{\mathcal{R}}(n) &= -1 + \sqrt{1 - \frac{\mathcal{G}}{12}R_{\text{cell}}^2 f(n)} \\ &= -1 + \sqrt{1 - \cos^2\left(\frac{\pi}{n}\right)\left(\frac{2}{3} + \frac{1}{3}\sec^2\left(\frac{\pi}{n}\right)\right)\frac{\mathcal{G}}{12}R_{\text{cell}}^2}\,. \end{aligned} \tag{4.25}$$

The effective strain depends on the number of edges due to the discrete rotational symmetry of polygons: points on each edge are weighted according to their distance from the centroid. The predicted shift in the critical shape index is

$$\begin{aligned} s_0^{\text{critical}}(n, \mathcal{G}) &= s_0^*(n)\ell(n)(1 + \epsilon_{\mathcal{G}}(n)) \\ &\approx s_0^*(n)(1 + \epsilon_{\mathcal{G}}(n))\,. \end{aligned} \tag{4.26}$$

where I have set $\ell \approx 1$, which restricts our prediction near the planar critical target shape index or large rigidity ratio $r >> 1$. Eq. 4.26 is the main result of this chapter. In the next section it is tested against simulation data.

Comparison with simulation

In recent work by Sussman [156] a disordered vertex model of N cells on a uniform sphere of radius $R_{\mathcal{G}} = \sqrt{\frac{N}{4\pi}}$ was simulated for various N. At the onset of rigidity the

critical shape index was extracted and reported to vary as a function of N, which monotonically increased until plateauing at $s_0^*(5) \sim 3.812$ for large N (see Fig. 4.2 D).

To compare with simulation in Ref. [156] I re-cast $\mathcal{G}R_{\text{cell}}^2$ in terms of N and consider the mean field treatment for pentagons, $n = 5$, corresponding to the rigidity of a disordered VM in the flat case. Sussman considered a sphere of radius $R_{\mathcal{G}} = \sqrt{\frac{N}{4\pi}}$ with average cell area set to unity, i.e. $A_{\text{cell}} \equiv \frac{N}{4\pi L^2} = 1$. Since the mean field calculation is for a single cell I make the ad-hoc choice to take R_{cell} corresponding to a pentagon, which corresponds to the critical shape index in flat disordered simulations and tissues [48, 30]. Thus $5R_{cell}^2 \cos\left(\frac{\pi}{5}\right)^2 \tan\left(\frac{\pi}{5}\right) = 1 \implies R_{\text{cell}}^2 \approx \frac{1}{2.377}$ (see Eq. 4.40).

Therefore the relative ratio of cell size to radius of curvature goes as $\frac{R_{\text{cell}}^2}{R_{\mathcal{G}}^2} \approx \frac{4\pi}{2.377}\frac{1}{N}$. This yields the predicted critical shape index

$$s_0^{\text{critical}}(n = 5, N) \approx 3.812\left(1 - \frac{1.36}{N}\right)^{1/2} . \tag{4.27}$$

A comparison of this result to the simulations of Ref. [156] is shown in Fig. 4.2D.

Besides expanding to higher order, the calculation can be improved by computing the ground state characteristic cell size ℓ_0 for curved vertex models, but this is beyond the current mean field approach. Additionally, [156] reports that the shape index distribution broadens for larger $R_{\text{cell}}^2\mathcal{G}$ (smaller N) reflecting a greater diversity of polygons at the rigidity transition than the flat counterpart. Taking into account this greater diversity could help refine the curvature correction in Eq. 4.27. In particular, for large curvature other polygonal shapes besides the pentagon could be relevant for disordered systems.

4.6 Discussion

Utilizing a mean field model, this chapter has showed that the asymmetry of the linear response of the vertex model under dilation and compression continuously extends away from the critical shape index for finite strains. The asymmetry reflects how an initially rigid tissue may be sufficiently compressed to induce shape degeneracy and thereby relax perimeter tension, yielding a softer bulk modulus. Conversely, sufficient dilation applied to a compatible (floppy) cell lifts shape degeneracy, yielding an increase of the bulk modulus. Thus applied dilation and compression shift the rigidity of the VM in 2D.

Using this insight, mean field model can be extended to calculate the effective dilation/compression engendered by intrinsic curvature and thereby predict the curvature-induced shift of the rigidity transition by calculating the effective critical shape index. The prediction is compared to simulations by Sussman [156] with good qualitative agreement.

The mean field prediction, namely Eq. 4.26, provides a metric which can be applied to studying the rigidity transition in curved biological tissues in a manner analogous to studies in the flat case. For instance, as previously mentioned in chapter 1, during *Drosophila* embryo development regions of jammed and unjammed cells are have been observed to correlate with regions of low and high positive intrinsic curvature [54]. Additionally, the shift of rigidity upon compression/dilation could be tested, for instance, in experiments such as those of Ref. [28], where an epithelial monolayer is compressed or stretched via an underlying deformable substrate.

Of interest is a recent similar mean field calculation where, instead of cell area, cell perimeter is calculated on a sphere [157], and from this the shift in the critical target shape index is calculated. The authors also find good qualitative agreement with simulation, thereby further verifying the role of curvature in the rigidity transition of the vertex

model and also providing a complementary mean field approach.

Appendix 5.A Details about metric expansion

The purpose of this appendix is to give a brief explanation of the series expansion of the metric in terms of curvature. A complete and rigorous treatment may be found in many textbooks on Riemannian geometry such as in [162, 163, 164]. The metric is a second order symmetric tensor whose components are spatially dependent function of the surface. It governs all geometric data in that the distance between any two points is given by the line element

$$ds^2 = g_{ij}(x)dx^i dx^j. \tag{4.28}$$

In general, about a given point $x_0 \in M$ the components of the metric may be approximated as constants to 1st order. One may diagonalize this approximation such that the metric at x_0 is given by δ_{ij}. However, upon expanding to 2nd order the metric's components are not necessarily also spatially constant. In fact, if there exist coordinates such that the metric's expansion is spatially constant up to 2nd order then the metric is totally flat in the neighborhood, which we will briefly show below. Normal coordinates about a point x_0 are defined as coordinates which parametrize a geodesic curve, γ^i, as a straight line, i.e. local coordinates x^i such that $\gamma^i(\lambda) = x^i\lambda$, where $\gamma(0) \equiv x_0$. In these coordinates the Christoffel symbols are extracted from the geodesic equation

$$0 = \frac{d^2\gamma^i}{d\lambda^2} + \Gamma^i_{k\ell}\frac{d\gamma^k}{d\lambda}\frac{d\gamma^\ell}{d\lambda}. \tag{4.29}$$

Utilizing normal coordinates, Eq. 4.29 implies $\Gamma^i_{k\ell}(x_0) = 0$. Differentiation also yields the differential constraint equation.

$$\partial_j \Gamma^i_{k\ell}(x_0) + \partial_k \Gamma^i_{\ell j}(x_0) + \partial_\ell \Gamma^i_{jk}(x_0) = 0. \tag{4.30}$$

The Riemann curvature tensor is defined as

$$R^i_{jkl} = \partial_k \Gamma^i_{jl} - \partial_l \Gamma^i_{jk} + \Gamma^i_{pk}\Gamma^p_{kl} + \Gamma^i_{pl}\Gamma^p_{kj}. \tag{4.31}$$

From the differential constraint and the definition of R^i_{jkl}, one can show

$$\partial_l \Gamma^k_{ij} = -\frac{1}{3}\left(R^k_{ijl} + R^k_{jil}\right). \tag{4.32}$$

Symmetry of the metric implies the covariant derivative of the metric vanishes, i.e. $\nabla \mathbf{g} = 0 \implies \partial_k g_{ij} - \Gamma^p_{jk} g_{ip} - \Gamma^p_{ik} g_{jp} = 0$. The second derivative of the metric in normal coordinates is

$$\partial^2_{kl} g_{ij} = -\frac{1}{3}\left(R_{klij} + R_{jlik}\right). \tag{4.33}$$

The Taylor expansion of the metric in normal coordinates yields

$$g_{ij} = \delta_{ij} - \frac{1}{3} R_{ijk\ell} x^k x^\ell + \mathcal{O}(|x|^2). \tag{4.34}$$

Higher order terms can be generated iteratively by calculating higher order differential constraint equations from Eqs.4.30 and $\nabla \mathbf{g} = 0$. For 2D surfaces the Riemann curvature

tensor only has a single d.o.f. and admits the representation [163]

$$R_{iklj} = \mathcal{G}(g_{ik}g_{lj} - g_{ij}g_{kl}). \tag{4.35}$$

Where $\mathcal{G}$ is the Gaussian curvature. From this the Ricci tensor follows $R_{ij} \equiv g^{kl}R_{iklj} = \mathcal{G}g_{ij}$. Using the expansion of the metric, we have to lowest order

$$R_{iklj} = \mathcal{G}(\delta_{ik}\delta_{lj} - \delta_{ij}\delta_{kl}) + \mathcal{O}(|x|^2) \tag{4.36}$$

$$R_{ij} = \mathcal{G}\delta_{ij} + \mathcal{O}(|x|^2) \tag{4.37}$$

These expressions reflect that locally any surface looks either flat ($\mathcal{G} = 0$), spherical ($\mathcal{G} > 0$), or saddle-like ($\mathcal{G} < 0$). To lowest order the metric expansion about p becomes

$$g_{ij} = \delta_{ij} - \frac{1}{3}\mathcal{G}(\delta_{ik}\delta_{lj} - \delta_{ij}\delta_{kl})x^k x^l + \mathcal{O}(|x|^3) \tag{4.38}$$

and determinant yields

$$\det(g) = 1 - \frac{1}{3}\mathcal{G}|x|^2 + \mathcal{O}(|x|^3) \tag{4.39}$$

which shows how curvature induces local compression or dilation. Higher order terms contain gradients and higher order invariants of R_{ijkl}, and are completely determined by $\mathcal{G}$. It follows that if the quadratic contribution vanishes, then the metric is totally flat locally.

Appendix 5.B Pertubative polygon area expansion

To explicitly parameterize the polygonal cell D, we will consider a regular n-gon and decompose it into 2n-triangles about its centroid as pictured in Fig.4.4. Working in terms

of polar coordinates, this yields for the first term

$$\begin{aligned}\int_D d^2x &= 2n\int_0^{\frac{\pi}{n}}\int_0^{R_{\text{cell}}\cos\left(\frac{\pi}{n}\right)\sec\theta} d\theta r dr \\ &= nR_{\text{cell}}^2\cos\left(\frac{\pi}{n}\right)^2\tan\left(\frac{\pi}{n}\right)\end{aligned} \tag{4.40}$$

In the limit of $n\to\infty$ we get πR_{cell}^2, as expected for circles. Using the same coordinate system, we compute the first correction due to curvature

$$\begin{aligned}\frac{\mathcal{G}}{6}\int_D |x|^2 d^2x &= \frac{\mathcal{G}}{6}2n\int_0^{\frac{\pi}{n}}\int_0^{R_{\text{cell}}\cos\left(\frac{\pi}{n}\right)\sec\theta} d\theta r^3 dr \\ &= \frac{\mathcal{G}}{12}R_{\text{cell}}^4\cos^4\left(\frac{\pi}{n}\right)n\left(\frac{2}{3}+\frac{1}{3}\sec^2\left(\frac{\pi}{n}\right)\right)\tan\left(\frac{\pi}{n}\right)\end{aligned} \tag{4.41}$$

Appendix 5.C Mean-field vertex model

The mean field model is defined by the area and perimeter of a single cell, which is parameterized by n-edges ν_α given by

$$\vec{\nu}_\alpha \equiv \ell_0\left(\cos\left(\frac{2\pi\alpha}{n}\right),\sin\left(\frac{2\pi\alpha}{n}\right)\right) \tag{4.42}$$

Where ℓ_0 the characteristic cell edge length. The perimeter is the sum of each edge length

$$P = \sum_\alpha^n \sqrt{\vec{\nu}_\alpha\cdot\vec{\nu}_\alpha} \tag{4.43}$$

Under an affine transformation, denoted as the matrix $\mathbf{F}$, the deformed perimeter is given by

$$P = \sum_{\alpha}^{n} \sqrt{(\mathbf{F}\vec{\nu}_\alpha) \cdot (\mathbf{F}\vec{\nu}_\alpha)}. \tag{4.44}$$

The area can be calculated by the cross product

$$A = \int_D dx^2 = n|\vec{a} \times \vec{b}| \tag{4.45}$$

where $\vec{a}$ and $\vec{b}$ are defined in Fig.4.4.

The deformed are is straightforward to calculate by using the identity $|(\mathbf{F}\vec{a}) \times (\mathbf{F}\vec{b})| = \det(\mathbf{F})|\vec{a} \times \vec{b}|$. Thus under an affine transformation the deformed area can be written as

$$A = \det(\mathbf{F}) n|\vec{a} \times \vec{b}| \tag{4.46}$$

$$= \det(\mathbf{F}) \frac{n}{4} \ell_0^2 \cot\left(\frac{\pi}{n}\right). \tag{4.47}$$

The energy per cell is cast as

$$E = \frac{\kappa_A}{2} \left(\frac{n}{4} \ell_0^2 \cot\left(\frac{\pi}{n}\right) \det(\mathbf{F}) - A_0 \right)^2 + \frac{\kappa_P}{2} \left(\sum_{\alpha}^{n} \sqrt{(\mathbf{F}\vec{\nu}_\alpha) \cdot (\mathbf{F}\vec{\nu}_\alpha)} - P_0 \right)^2 \tag{4.48}$$

To non-dimensionalize we define reference lengths ℓ_A and ℓ_P such that

$$A_0 = \frac{n}{4} \ell_A^2 \cot\left(\frac{\pi}{n}\right) \tag{4.49}$$

$$P_0 = n\ell_P \tag{4.50}$$

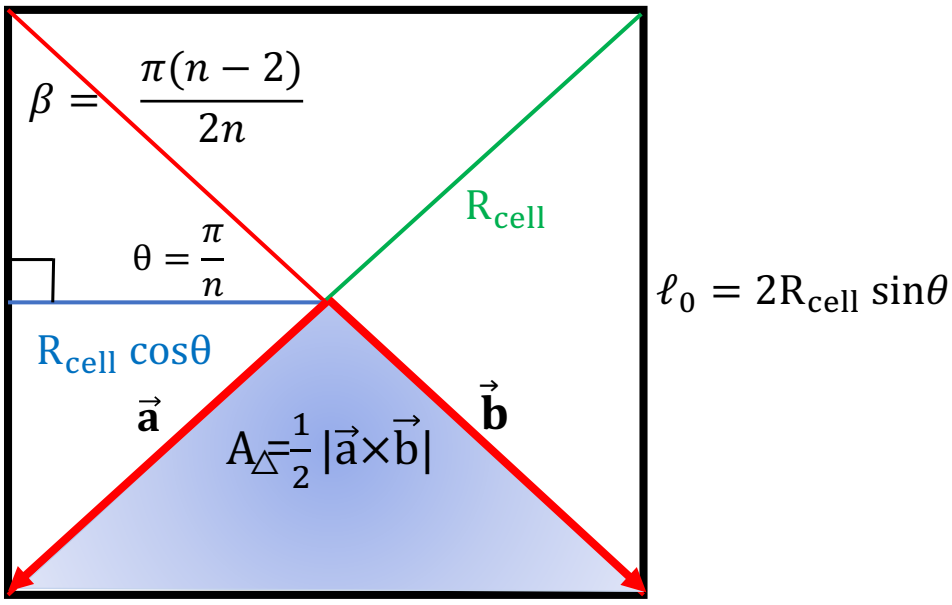

Figure 4.4—The shape of a regular polygon can be determined by the number of edges and the length of each edge. To modify and aide our calculation for various n-gons, we decompose a polygon into n triangular wedges as illustrated in the figure. Thus one may specify a regular polygon by the number edges and either the edge length ℓ_0 or cell radius R_{cell}.

And rescale energy by $\kappa_A A_0^2$, yielding

$$E = \frac{1}{2}\left(\ell^2 \det(\mathbf{F}) - 1\right)^2 + \frac{r}{2}\left(\ell \sum_{\alpha}^{n} \sqrt{(\mathbf{F}\vec{\nu}_\alpha)\cdot(\mathbf{F}\vec{\nu}_\alpha)} - s_0\right)^2 \tag{4.51}$$

Where $r \equiv \frac{\kappa_P}{\kappa_A A_0}$, $s_0 \equiv \frac{P_0}{\sqrt{A_0}}$ is the target shape index, and $\ell \equiv \frac{\ell_0}{\sqrt{A_0}}$ is the re-scaled characteristic cell edge length. In the incompatible state, the ground state corresponds to a regular polygon with ℓ_0 defined to minimize the energy. This involves solving the cubic equation defined $\frac{\partial E}{\partial \ell} = 0$. The relevant solution obeys the inequality $\ell \leq 1$ for all $s_0 \leq s_0^*$. In the compatible state energy minimization yields $\ell \equiv 1$ for choices of r and $s_0 \geq s_0^*$.

Inputting deformations

We model all cell shape distortions due to both applied deformations and cell response of the cell by linear affine transformation $\mathbf{F}$. For example, compression/dilation correspond to

$$\mathbf{F}_\epsilon = \begin{pmatrix} 1+\epsilon & 0 \\ 0 & 1+\epsilon \end{pmatrix}. \tag{4.52}$$

We also parametrize a self-shear corresponding to the cell adjusting its perimeter without changing the imposed re-scaled area by enforcing the constraint $\det\left(\mathbf{F}^{\text{cell}}\right) = 1$. This only fixes a single degree of freedom, leaving in principle three components of $\mathbf{F}_{\text{cell}}$ free. For simplicity, we only consider the the cell's response by tilting through a simple shear transformation

$$\mathbf{F}_\theta^{\text{cell}} = \begin{pmatrix} 1 & \tan(\theta) \\ 0 & 1 \end{pmatrix} \tag{4.53}$$

We set the overall transformation in the mean field model as

$$\mathbf{F} = \mathbf{F}_\theta^{\text{cell}} \cdot \mathbf{F}_\epsilon = (1+\epsilon) \begin{pmatrix} 1 & \tan(\theta) \\ 0 & 1 \end{pmatrix} \tag{4.54}$$

Chapter 5

Hydrodynamic theory of deformable particles

This chapter is adapted from Physical Review E article [165] published in 2021 with M. Cristina Marchetti. The idea was conceptualized by M. Cristina Marchetti with theoretical calculations performed by myself.

Many extended systems, such as biological tissue [166], foams [167, 168], emulsions [169, 170], and colloidal suspensions [169] can be described as collections of deformable particles. A variety of mesoscopic models have been developed to examine the role of particle shape on the structure and rheology of these soft materials.

Cellular Potts models [109, 171] and Vertex and Voronoi models [172, 173, 45] have been successfully used to describe dry foams and confluent layers of biological tissue, where cells completely cover the plane with no gaps, with extensions to three dimensions [174, 68]. These models describe cells in confluent tissues as tightly packed irregular polygons covering the plane and predict a jamming-unjamming transition tuned by a target cell shape that captures the interplay of cortex contractility and cell-cell adhesion, with the mean cell shape serving as a metric for tissue fluidity [47, 48, 39]. Vertex and Voronoi models do not, however, have a natural extension to situations where the cell packing fraction is below one, although gaps between cells have been incorporated in recent work [175, 27]. In contrast, both particle deformability and density variations can be incorporated in multi-phase field models and in models of deformable particles [176], which have been used to examine solid-liquid transitions as a function of both particle shape and density.

Less well developed are continuum descriptions of the rheology of materials where the constituents can change their shape. An important example is the classic work by Doi and Ohta that describes the dynamics of the interface between two immiscible fluids under shear, incorporating formation, rupture and deformation of droplets [72]. Continuum mechanics of confluent tissue have been constructed phenomenologically and employed to connect structure and mechanics in *Drosophila* development [177, 178]. Ishihara and collaborators formulated a continuum model that couples cell shape to mechanical deformations at the tissue scale [76]. Their work, however, only captures *simultaneous* cell anisotropy and alignment of elongated cell shapes, without distinguishing between

a tissue where cell shapes are on average isotropic and one where cells are on average anisotropic, but not aligned, as observed in simulations of Vertex/Voronoi models [39, 179]. It is in fact the single-cell anisotropy that provides an order parameter for cell jamming in Vertex and Voronoi models [47, 48, 39], where fluid states of elongated cells are obtained without nematic order of elongated cells. The importance of this distinction in a continuum theory of tissue mechanics was highlighted recently in work by one of us and collaborators [78].

In this chapter we adopt the Poisson-bracket formulation [180] to obtain continuum equations for a fluid of deformable particles in two dimensions. This method has the advantage of providing a systematic derivation of the reversible part of the hydrodynamic equations once the continuum fields have been identified. The approach considered here is inspired by work by Stark and Lubensky [181, 182] who used the Poisson-bracket approach to derive the hydrodynamics of a nematic liquid crystal. As in liquid crystals, we identify both a continuum scalar field that quantifies fluctuations of individual cell shape and a cell shape tensor field that captures both cell elongation and alignment. An important difference is that, while in passive liquid crystals molecular shape fluctuations decay on fast (non-hydrodynamic) time scales, numerical studies of both Vertex and Voronoi models of 2D confluent epithelial tissues [47, 48, 39] have shown that mean cell shape, as measured by the cell perimeter normalized by cell area, provides an order parameter for a transition between solid and liquid states. In the solid state cells are isotropic and encounter finite energy barriers for neighbor exchange. These barriers vanish in the liquid state, where cells acquire anisotropic shapes with large perimeters. The role of mean cell shape as a direct metric for tissue fluidity has been confirmed by experiments in various cell types [30, 40]. Thus shape-anisotropy fluctuations are long-lived near the transition, justifying the inclusion of this field in a hydrodynamic model. The equations derived here provide a continuum model for collections of interacting

deformable "particles" and can be adapted to describe both confluent and non-confluent systems.

The chapter is organized as follows. Section 5.1 provides the microscopic definition of the continuum fields used in the hydrodynamic model. Section 5.2 briefly summarizes the Poisson-bracket (PB) method and the calculation of the various PBs (with details given in Appendix 5.5), and discuss the reactive and dissipative contributions to the coarse-grained dynamics. The final continuum equations are displayed in Section 5.3. In Section 5.4 I discuss the form of the continuum equations for the specific case of a cellular tissue, and conclude with a brief discussion in Section 5.5. Details of the derivation of the PBs and of the mean-field free energy of the Vertex model are given in appendices.

5.1 Continuum fields

We consider a fluid whose constituents are N extended particles of arbitrary shape. The contour of each particle, referred to below as a 'cell', is described by a polygonal shape joining n vertices located at $\mathbf{r}_\mu^\alpha$, where $\mu = 1, 2, \cdots, n$ labels the vertices and $\alpha = 1, 2, \cdots, N$ labels the cells, as shown in Figure 5.1. Each cell has a total mass m_c, which we assume equally distributed among the n vertices. Note that (hence mass) proteins can often be anisotropically distributed in the interior of cells, resulting in important properties at the scale of the whole cell, such as planar cell polarity [178, 183]. The assumption of uniform mass distribution hence amounts to neglecting cell polarization. Including the dynamics of cell polarization is of course important in a number of biological situations, and will be considered in future work.

Cell shape is described by a shape tensor defined as

$$G_{ij}^\alpha = \frac{1}{n}\sum_{\mu=1}^{n} \Delta x_i^{\alpha\mu} \Delta x_j^{\alpha\mu} \ , \tag{5.1}$$

where $\Delta\mathbf{r}^{\alpha\mu} = \mathbf{r}^{\alpha\mu} - \mathbf{r}_\alpha$, with $\mathbf{r}_\alpha = \frac{1}{n}\sum_\mu \mathbf{r}^{\alpha\mu}$, and Latin indices i, j denote components. The shape tensor has been used to describe polymer conformation [184] and the structure of foams [185], as well cellular shape in epithelia [76, 78]. It quantifies area, perimeter and elongations of convex polygonal shapes composed of n vertices connected by rigid edges. The limit $n \to \infty$ corresponds to an ellipse. We define microscopic mass, momentum

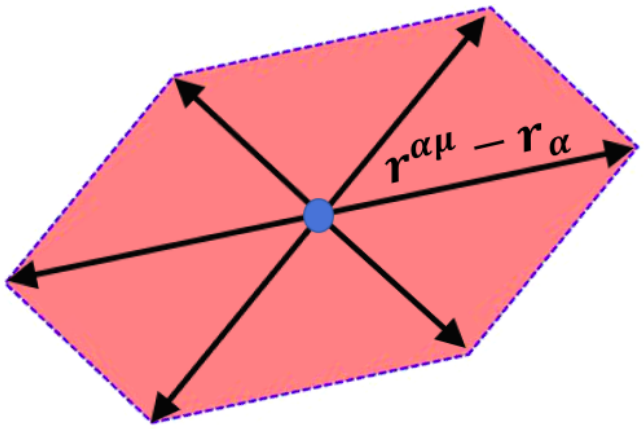

Figure 5.1—A deformable particle (referred to as a 'cell') is described as an n-sided irregular polygon defined by the positions $\mathbf{r}_{\alpha\mu}$ of its vertices, for $\mu = 1, \cdots, n$, relative to the location of the centroid $\mathbf{r}_\alpha$ of the polygon.

and cell shape density fields as

$$\hat{\rho}(\mathbf{r}, t) = \sum_{\alpha\mu} m\ \delta(\mathbf{r} - \mathbf{r}^{\alpha\mu}(t))\ , \tag{5.2}$$

$$\hat{\mathbf{g}}(\mathbf{r}, t) = \sum_{\alpha\mu} \mathbf{p}^{\alpha\mu}\ \delta(\mathbf{r} - \mathbf{r}^{\alpha\mu}(t))\ , \tag{5.3}$$

$$\hat{G}_{ij}(\mathbf{r}, t) = \sum_{\alpha} G^\alpha_{ij}\ \delta(\mathbf{r} - \mathbf{r}_\alpha(t))\ . \tag{5.4}$$

with $m = m_c/n$, and $\mathbf{p}^{\alpha\mu} = m\dot{\mathbf{r}}^{\alpha\mu}$ is the conjugate momentum. Coarse grained quantities are then defined as $\rho(\mathbf{r}, t) = [\hat{\rho}(\mathbf{r}, t)]_c$, $\mathbf{g}(\mathbf{r}, t) = [\hat{\mathbf{g}}(\mathbf{r}, t)]_c$ and $G_{ij}(\mathbf{r}, t) = \left[\hat{G}_{ij}(\mathbf{r}, t)\right]_c$ and correspond to macroscopic continuum fields describing the system on length scales large compared to both the size of the particles and their mean separation. Note that since the

microscopic single-cell shape tensor $\mathbf{G}^\alpha$ has dimensions of length squared, the density of cellular shape tensor G_{ij} is dimensionless. As we will see below, the trace of the shape tensor density provides a measure of the density of cell perimeter, while its traceless part, $\tilde{G}_{ij} = G_{ij} - \frac{1}{2}\delta_{ij}\mathrm{Tr}[\mathbf{G}]$, captures both cell anisotropy and local alignment of elongated cells.

The cellular shape tensor can be written in terms of its eigenvalues as

$$G^\alpha_{ij} = \frac{1}{2}\left(\lambda^\alpha_1 + \lambda^\alpha_2\right)\delta_{ij} + \left(\lambda^\alpha_1 - \lambda^\alpha_2\right)\left(\hat{\nu}^\alpha_i\hat{\nu}^\alpha_j - \frac{1}{2}\delta_{ij}\right) , \tag{5.5}$$

where $\lambda^\alpha_1 > \lambda^\alpha_2$ and $\hat{\nu}^\alpha$ is the eigenvector of the largest eigenvalue. Its traceless part can be written in terms of the local molecular alignment tensor, $\tilde{G}^\alpha_{ij} = (\lambda^\alpha_1 - \lambda^\alpha_2)Q^\alpha_{ij}$, where $Q^\alpha_{ij} = \left(\hat{\nu}^\alpha_i\hat{\nu}^\alpha_j - \frac{1}{2}\delta_{ij}\right)$.

For regular $n-$sided polygons, the shape tensor is diagonal with $\lambda^\alpha_1 = \lambda^\alpha_2$. In this case the cell area $A^{(n)}_\alpha$ and perimeter $P^{(n)}_\alpha$ can be expressed in terms of the invariants of the tensor $\mathbf{G}^\alpha$ as

$$A^{(n)}_\alpha = \frac{n}{2}\sin\left(\frac{2\pi}{n}\right)\sqrt{\det[\mathbf{G}^\alpha]} , \tag{5.6}$$

$$P^{(n)}_\alpha = \sqrt{2}n\sin\left(\frac{\pi}{n}\right)\sqrt{\mathrm{Tr}[\mathbf{G}^\alpha]} , \tag{5.7}$$

The derivation of Eqs. 6 and 7 is given in Appendix 5.5. Single cell anisotropy is measured by $M_\alpha = \lambda^\alpha_1 - \lambda^\alpha_2$ which vanishes for regular polygons. To quantify single-cell elongation independently of alignment of elongated cells, we follow [78], albeit with a slightly different definition of the shape tensor, and introduce an anisotropy density field defined as

$$\hat{M}(\mathbf{r}, t) = \sum_\alpha M_\alpha\delta(\mathbf{r} - \mathbf{r}_\alpha(t)) \tag{5.8}$$

and the associated coarse grained field $M(\mathbf{r},t) = [\hat{M}(\mathbf{r},t)]_c$. Work on Vertex/Voronoi models of confluent biological tissue, as well as multiphase fields models, has demonstrated the correlation between tissue fluidity and anisotropy of single-cell shape, as quantified here by M. In Vertex models, this anisotropy provides an order parameter for the solid-liquid transition [48, 39].

In the following, we construct hydrodynamic equations for a fluid of deformable particles that couple structural changes encoded in cell shape and alignment of elongated cells to flow. The dynamics of the fluid on scales large compared to the cell size and mean cell separation is described in terms of a few continuum fields: the mass density ρ, the momentum density $\mathbf{g}$, the single-cell anisotropy density M and the cell-shape tensor density G_{ij}.

5.2 Poisson-Bracket formulation of continuum dynamics

Here we briefly summarize the Poisson-bracket (PB) formalism. Consider a system whose microscopic dynamics is determined by canonically conjugate positions $\mathbf{r}^\alpha$ and momenta $\mathbf{p}^\alpha$. We describe the dynamics in terms of a few microscopic density fields $\hat{\Psi}^a(\mathbf{r},t;\{\mathbf{r}^\alpha\},\{\mathbf{p}^\alpha\})$, for $a = 1, 2, \cdots$. These fields are chosen to be either hydrodynamic fields associated with conserved quantities, broken symmetry fields, or quasi-hydrodynamic fields that decay on times scales large compared to microscopic ones. In the specific case of interest here $\{\hat{\Psi}^a\} = (\hat{\rho}, \hat{\mathbf{g}}, \hat{G}_{ij}, \hat{M})$. The dynamics of the corresponding coarse-grained fields $\Psi^a(\mathbf{r},t) = [\hat{\Psi}^a(\mathbf{r},t;\{\mathbf{r}^\alpha\},\{\mathbf{p}^\alpha\})]_c$ is governed by the equations

$$\partial_t \Psi^a(\mathbf{r},t) = V^a(\mathbf{r},t) + D^a(\mathbf{r},t) \ , \tag{5.9}$$

where V^a and D^a represent the non-dissipative and dissipative parts of the dynamics, respectively. The reactive term V^a is given by

$$V^a(\mathbf{r}) = -\int_{\mathbf{r}'} \{\Psi^a(\mathbf{r}), \Psi^b(\mathbf{r}')\} \frac{\delta \mathcal{F}}{\delta \Psi^b(\mathbf{r}')} \, , \tag{5.10}$$

where $\mathcal{F}[\{\Psi^a\}]$ is the free energy,

$$\{\Psi^a(\mathbf{r}), \Psi^b(\mathbf{r}')\} = \Big[\{\hat{\Psi}^a(\mathbf{r}), \hat{\Psi}^b(\mathbf{r}')\}\Big]_c \, , \tag{5.11}$$

and

$$\begin{aligned} \{\hat{\Psi}^a(\mathbf{r}), \hat{\Psi}^b(\mathbf{r}')\} = \quad & \sum_{\alpha i} \Big(\frac{\partial \hat{\Psi}^a(\mathbf{r})}{\partial p_i^\alpha} \frac{\partial \hat{\Psi}^b(\mathbf{r}')}{\partial r_i^\alpha} \\ & - \frac{\partial \hat{\Psi}^a(\mathbf{r})}{\partial r_i^\alpha} \frac{\partial \hat{\Psi}^b(\mathbf{r}')}{\partial p_i^\alpha} \Big) \, . \end{aligned} \tag{5.12}$$

Finally, the dissipative term in the kinetic equation is controlled by all the neglected microscopic degrees of freedom and can be written as

$$D^a(\mathbf{r}) = -\Gamma^{ab} \frac{\delta \mathcal{F}}{\delta \Psi^b(\mathbf{r})} \, . \tag{5.13}$$

The dissipation tensor Γ^{ab} is in general a functional of the $\{\Psi^a\}$ and their gradients. It is a phenomenological quantity controlled by the requirement that $\partial_t \Psi^a$ can only couple to driving forces $\frac{\delta \mathcal{F}}{\delta \Psi^b(\mathbf{r})}$ that have different sign under time reversal, to guarantee that such terms describe dissipation. Close to equilibrium it is a symmetric tensor and it must obey Onsager's principle [186].

5.2.1 Poisson brackets

The calculation of the PB of mass and momentum density is straightforward and can be found in the literature [181], with the result

$$\begin{aligned}
&\{\rho(\mathbf{r}), g_i(\mathbf{r}')\} = \rho(\mathbf{r}')\partial_i\delta(\mathbf{r}-\mathbf{r}') \ , \\
&\{g_i(\mathbf{r}), g_j(\mathbf{r}')\} = -\partial_i'[\delta(\mathbf{r}-\mathbf{r}')g_j(\mathbf{r}')] + \partial_j\delta(\mathbf{r}-\mathbf{r}')g_i(\mathbf{r}') \ ,
\end{aligned} \tag{5.14}$$

The main PBs to be calculated here are those involving the fields describing cellular shape. The details of the derivation are shown in Appendix 5.5, with the result

$$\begin{aligned}
\{G_{ij}(\mathbf{r}), g_k(\mathbf{r}')\} \quad &= \partial_k[G_{ij}(\mathbf{r}')\delta(\mathbf{r}-\mathbf{r}')] \\
&- [G_{il}(\mathbf{r})\delta_{jk} + G_{jl}(\mathbf{r})\delta_{ik}]\,\partial_l\delta(\mathbf{r}-\mathbf{r}') \ ,
\end{aligned} \tag{5.15}$$

$$\{M(\mathbf{r}), g_i(\mathbf{r}')\} = [\partial_i M(\mathbf{r})]\delta(\mathbf{r}-\mathbf{r}') - \frac{2R(\mathbf{r})}{M(\mathbf{r})}\tilde{G}_{ij}(\mathbf{r})\partial_j\delta(\mathbf{r}-\mathbf{r}') \ . \tag{5.16}$$

where we have defined $R(\mathbf{r},t) = \Big[\mathrm{Tr}[\hat{\mathbf{G}}(\mathbf{r},t)]\Big]_c$.

To calculate $\{M(\mathbf{r}), g_i(\mathbf{r}')\}$ we have used the identity $\tilde{G}^\alpha_{ik}\tilde{G}^\alpha_{kj} = \frac{M_\alpha^2}{4}\delta_{ij}$. where the tilde denotes the traceless part of a rank-2 tensor, $\tilde{G}_{ij} = G_{ij} - \frac{1}{2}\delta_{ij}\mathrm{Tr}[\mathbf{G}]$.
This allows us to write

$$M_\alpha\{M_\alpha\delta(\mathbf{r}-\mathbf{r}^\alpha), g_i(\mathbf{r}')\} = 2\tilde{G}^\alpha_{kl}\{\tilde{G}^\alpha_{kl}\delta(\mathbf{r}-\mathbf{r}^\alpha), g_i(\mathbf{r}')\} \ . \tag{5.17}$$

Finally, the other PBs can be obtained using the identity

$$\{\Psi_n(\mathbf{r}), \Psi_m(\mathbf{r}')\} = -\{\Psi_m(\mathbf{r}'), \Psi_n(\mathbf{r})\} \ . \tag{5.18}$$

5.2.2 Reactive terms

To evaluate the various contributions to the continuum dynamics, we need to specify the free energy of the system. In general, this has the form

$$\begin{aligned}\mathcal{F} &= \mathcal{F}_K + \mathcal{F}_V \\ &= \int_{\mathbf{r}} \left[\frac{\mathbf{g}^2}{2\rho} + f(\rho, M, \nabla M, G_{ij}, \nabla G_{ij}) \right] , \end{aligned} \tag{5.19}$$

where the first term is the kinetic part and the free energy density f depends on the fields and their gradients.

Using the expressions for the Poisson-brackets we can then evaluate the reactive terms V^a, with the result

$$V^\rho = -\nabla \cdot (\rho \mathbf{v}) , \tag{5.20}$$

$$\begin{aligned} V_i^g &= -\partial_j(\rho v_i v_j) - \rho \partial_i \frac{\delta \mathcal{F}_V}{\delta \rho} + (\partial_i M) \frac{\delta \mathcal{F}_V}{\delta M} + (\partial_i G_{kl}) \frac{\delta \mathcal{F}_V}{\delta G_{kl}} \\ &\quad + \partial_j \left(2 G_{jk} \frac{\delta \mathcal{F}_V}{\delta G_{ik}} - \delta_{ij} G_{kl} \frac{\delta \mathcal{F}_V}{\delta G_{kl}} \right) \\ &\quad + 2 \partial_j \left(\frac{R}{M} \tilde{G}_{ij} \frac{\delta \mathcal{F}_V}{\delta M} \right) , \end{aligned} \tag{5.21}$$

$$V_{ij}^G = -\nabla \cdot (G_{ij} \mathbf{v}) + G_{ik} \partial_k v_j + G_{jk} \partial_k v_i \ , \tag{5.22}$$

$$V^M = -\mathbf{v} \cdot \nabla M + \frac{2R}{M} \tilde{G}_{ij} \partial_i v_j . \tag{5.23}$$

The elastic and density couplings in Eq. (5.21) can be rewritten in a more familiar form as gradients of pressure and of an elastic stress. The details can be found in Appendix 5.5, where it is shown that we can write

$$-\rho \partial_i \frac{\delta \mathcal{F}_V}{\delta \rho} + (\partial_i M) \frac{\delta \mathcal{F}_V}{\delta M} + (\partial_i G_{kl}) \frac{\delta \mathcal{F}_V}{\delta G_{kl}} = -\partial_i p + \partial_j \sigma_{ij}^E \tag{5.24}$$

where the pressure p and the elastic stress σ^E_{ij}, that plays the role of the Ericksen stress of nematic liquid crystals, are given by

$$p = \rho\frac{\delta\mathcal{F}_V}{\delta\rho} - f \ , \tag{5.25}$$

$$\sigma^E_{ij} = -\frac{\partial f}{\partial\nabla_j M}\nabla_i M - \frac{\partial f}{\partial\nabla_j G_{kl}}\nabla_i G_{kl} \ . \tag{5.26}$$

The last two terms in Eq.(5.21) correspond to gradients of a reactive elastic stress σ^G_{ij}, given by

$$\sigma^G_{ij} = 2\frac{R}{M}\tilde{G}_{ij}\frac{\delta\mathcal{F}_V}{\delta M} + 2G_{jk}\frac{\delta\mathcal{F}_V}{\delta G_{ik}} - \delta_{ij}G_{kl}\frac{\delta\mathcal{F}_V}{\delta G_{kl}} \ . \tag{5.27}$$

The reactive term for the momentum density equation can then be written as

$$V^g_i = -\partial_j(\rho v_i v_j) - \partial_i p + \partial_j\left(\sigma^G_{ij} + \sigma^E_{ij}\right) \ . \tag{5.28}$$

5.2.3 Dissipative terms

There is no dissipative term for the mass density ρ if it is conserved. Dissipative terms in the momentum equation must be odd under time reversal and hence must couple to gradients of velocity. In general, shape anisotropy and alignment of elongated cells will entail anisotropic viscosity coefficients, as in the case for liquid crystals. For simplicity, here we only introduce two viscosities to account for shear (η) and bulk (η_b) deformations and write

$$D^g_i = \partial_j\sigma^D_{ij} \ , \tag{5.29}$$

with

$$\sigma^D_{ij} = 2\eta D_{ij} + \eta_b\delta_{ij}\nabla\cdot\mathbf{v} \ , \tag{5.30}$$

where D_{ij} is the symmetrized and traceless rate of strain tensor,

$$D_{ij} = \frac{1}{2}(\partial_i v_j + \partial_j v_i - \delta_{ij}\nabla \cdot \mathbf{v}) \; . \tag{5.31}$$

Dissipative couplings in the equations for the shape density tensor G_{ij} and the shape anisotropy field M must be even under time reversal and hence can couple to M, G_{ij} and their gradients. Dissipation will arise from topological rearrangements, as well as from birth/death events when density conservation is broken. In general we can write

$$D^G_{ij} = -\Gamma^{GG}_{ijkl}\frac{\delta \mathcal{F}_V}{\delta G_{kl}} - \Gamma^{GM}_{ij}\frac{\delta \mathcal{F}_V}{\delta M} \; , \tag{5.32}$$

$$D^M = -\Gamma^{MM}\frac{\delta \mathcal{F}_V}{\delta M} - \Gamma^{MG}_{ij}\frac{\delta \mathcal{F}_V}{\delta G_{ij}} \; . \tag{5.33}$$

The kinetic coefficients Γ^{ab} can generally depend on the shape tensor and anisotropy density field. To linear order in these fields, a general form is given by

$$\begin{aligned} \Gamma^{GG}_{ijkl} &= \frac{M}{2\gamma_G}\left(\delta_{ik}\delta_{jl} + \delta_{jk}\delta_{il}\right) \\ &\quad + \frac{1}{\gamma_1}\left(\delta_{ik}G_{jl} + \delta_{jk}G_{il} + \delta_{il}G_{jk} + \delta_{jl}G_{ik}\right) \; , \end{aligned} \tag{5.34}$$

$$\Gamma^{GM}_{ij} = \Gamma^{MG}_{ij} = \frac{G_{ij}}{\gamma_2} \; , \tag{5.35}$$

$$\Gamma^{MM} = \frac{1}{\gamma_M} + \frac{M}{\gamma_3} \; , \tag{5.36}$$

where the kinetic coefficients γ_i, for $i = G, M, 1, 2, 3$, encode the characteristic time scales of dissipative processes. For simplicity we have assumed $\Gamma^{GM}_{ij} = \Gamma^{MG}_{ij}$ although in general the parameters controlling the relaxation in these terms could differ. Note that the second term in Eq. (5.34) has the form introduced in Ref. [187] for the kinetic coefficient describing the relaxation of the conformation tensor in a polymer suspension.

5.3 Final equations

Putting it all together, we now write the final form of the equations we have obtained. It is convenient to write

$$\partial_i v_j = D_{ij} + \omega_{ij} + \frac{1}{2}\delta_{ij}\nabla\cdot\mathbf{v} \tag{5.37}$$

where D_{ij} is the rate of strain tensor given in Eq. (5.31) and ω_{ij} is the vorticity,

$$\omega_{ij} = \frac{1}{2}(\partial_i v_j - \partial_j v_i)\ . \tag{5.38}$$

The set of continuum equations for our fluid of deformable cells is then given by

$$\partial_t \rho = -\nabla\cdot\rho\mathbf{v}, \tag{5.39}$$

$$\rho\left(\partial_t + \mathbf{v}\cdot\nabla\right)v_i = -\partial_i p + \partial_j\left(\sigma^G_{ij} + \sigma^E_{ij} + \sigma^D_{ij}\right), \tag{5.40}$$

$$\frac{d}{dt}M = \frac{2R}{M}\tilde{G}_{ij}D_{ij} - \Gamma^{MM}\frac{\delta\mathcal{F}_V}{\delta M} - \Gamma^{MG}_{ij}\frac{\delta\mathcal{F}_V}{\delta G_{ij}}, \tag{5.41}$$

$$\frac{D}{Dt}G_{ij} = G_{ik}D_{kj} + D_{ik}G_{kj} - \Gamma^{GG}_{ijkl}\frac{\delta\mathcal{F}_V}{\delta G_{kl}} - \Gamma^{GM}_{ij}\frac{\delta\mathcal{F}_V}{\delta M}, \tag{5.42}$$

We have defined

$$\begin{aligned}\frac{d}{dt} &= \partial_t + \mathbf{v}\cdot\nabla\ ,\\ \frac{D}{Dt} &= \frac{d}{dt} - [\omega,\cdot]\end{aligned} \tag{5.43}$$

where $\frac{d}{dt}$ is the convective derivative and $[\omega,\cdot]$ is the corotational derivative [1].

The equation for the shape tensor G_{ij} contains couplings to flow vorticity and strain rate which control the tendency of extended and deformable particles to rotate with flow and align with streamlines. The shape tensor G_{ij} plays a role similar to that of the

[1] For tensors ω_{ij} and D_{ij}, the communtator is defined as $[\omega, D]_{ij} = \omega_{ik}D_{kj} - D_{ik}\omega_{kj}$

conformation tensor in a polymer suspension [184]. In fact, if we ignore the additional anisotropy density field M, the equations derived here for a fluid of deformable particles have the same structure as a one-fluid model of viscoelastic polymer solutions [187]. Unlike in models of polymer suspensions, however, the coefficient of the coupling to strain rate, known in that context as the slip parameter [184], is found to be simply equal to 1 in our PB formulation.

It is also convenient to separate the dynamics of G_{ij} in that of its trace and deviatoric part. The corresponding equations are given by

$$\frac{d}{dt}R = 2\tilde{G}_{ij}D_{ji} - \Gamma^{GG}_{iikl}\frac{\delta\mathcal{F}_V}{\delta G_{kl}} - \Gamma^{GM}_{ii}\frac{\delta\mathcal{F}_V}{\delta M}, \tag{5.44}$$

$$\begin{aligned}\frac{D}{Dt}\tilde{G}_{ij} &= RD_{ij} + \tilde{G}_{ik}D_{kj} + D_{ik}\tilde{G}_{kj} - \delta_{ij}\tilde{G}_{kl}D_{kl} \\ &\quad - \left[\Gamma^{GG} : \frac{\delta\mathcal{F}_V}{\delta\mathbf{G}}\right]^{ST}_{ij} - \left[\Gamma^{GM}\right]^{ST}_{ij}\frac{\delta\mathcal{F}_V}{\delta M}\,.\end{aligned} \tag{5.45}$$

where $[...]^{ST}$ denotes the symmetrized and traceless part of the tensor. These equations need to be completed by an expression for the free energy $\mathcal{F}_V$ in terms of the shape tensor and anisotropy density field. Such an expression of course depends on the system of interest. In the next section we consider the specific case of a model of dense biological tissues.

5.4 Cellular tissue

In this section we utilize the vertex model to complete our hydrodynamic theory to describe the interplay between cell shape and flow in confluent biological tissues, where cells are tightly packed, with no intervening gaps. As previously mentioned, Vertex and Voronoi models have been extensively used in describing cells as irregular polygons tesselating the plane [172, 173, 45]. Since the vertex model explicitly depends on geometric

quantities such as cell perimeter and area, we may naturally re-write the energy in terms of cell shape anisotropy. The relevant aspects of the model itself are briefly repeated here for convenience, with a more thorough treatment given in chapter 1.

The behavior of the tissue is controlled by an energy that describes the tendency of each cell to adjust its area A_α and perimeter P_α to target values A_0 and P_0, given by

$$E_V = \sum_\alpha \left[\frac{\kappa_A}{2} \left(A_\alpha - A_0 \right)^2 + \frac{\kappa_P}{2} \left(P_\alpha - P_0 \right)^2 \right] \ , \tag{5.46}$$

with κ_A and κ_P stiffness parameters. The first term arises from tissue incompressibility in three dimensions and the second captures the interplay of cell-cell adhesion and cortical contractility. By scaling lengths with $\sqrt{A_0}$ and energies with $\kappa_A A_0^2$, the scaled energy of each cell is given by

$$\epsilon_\alpha = \frac{1}{2} \left(a_\alpha - 1 \right)^2 + \frac{r}{2} \left(p_\alpha - s_0 \right)^2 \ , \tag{5.47}$$

with $p_0 = P_0/\sqrt{A_0}$ the target shape parameter and $r = \kappa_P/(\kappa_A A_0)$.

Numerical studies of this energy have identified a rigidity transition at a critical value s_0^* of the target shape parameter between a rigid, solid-like state for $p_0 < p_0^*$ to a fluid state for $s_0 > s_0^*$. Single-cell anisotropy as quantified by the mean cell-shape index $s = \langle P_\alpha/\sqrt{A_\alpha} \rangle$, with the brackets denoting an average over all cells, provides an order parameter for the transition. Czajkowski *et al.* [78] derived a mean-field model of this rigidity transition, albeit using a different definition of the cell shape tensor G_{ij}^α as compared to the one used here. The derivation carried out with our definition is outlined in Appendix 5.5. The result is a quartic Landau-type free energy density f_M where the the cell shape anisotropy density M plays the role of an order parameter, given by

$$f_M = \frac{\alpha(s_0)}{2} M^2 + \frac{\beta}{4} M^4 \ , \tag{5.48}$$

where $\alpha(s_0)$ vanishes at $s_0 = s_0^*$ and $\beta > 0$. The definition of the shape tensor of individual cells only affects the precise values of these parameters that also depend on the reference polygonal shape, but does not change the form of the free energy density nor the value of s_0^*. The free energy given in Eq. (5.48) is obtained by assuming small deformations from regular polygons and constant cell perimeter. It predicts a mean-field transition at $\alpha = 0$ from a state where cells are isotropic ($M = 0$) $\alpha > 0$ or $s_0 < s_0^*$ (the solid state) to a state where cells are anisotropic ($M = \sqrt{-\alpha/\beta}$) for $\alpha < 0$ or $s_0 > s_0^*$ (the liquid state).

This work suggests a phenomenological free energy for a confluent tissue that captures both fluctuations in the cell anisotropy density M that quantifies the liquid-solid transition and the shape tensor density $\tilde{G}_{ij}$ that quantifies alignment of elongated cell as

$$\mathcal{F}_c = \int_{\mathbf{r}} \left[\frac{\alpha(p_0)}{2} M^2 + \frac{\beta}{4} M^4 + \frac{K}{2} (\nabla M)^2 + \frac{\chi}{2} Tr[\tilde{\mathbf{G}}^2] + \frac{K_G}{2} (\partial_j \tilde{G}_{ik})^2 \right] . \tag{5.49}$$

We do not include terms of order $Tr[\tilde{\mathbf{G}}^2]^2$ as we do not expect any nematic order of cellular shapes in the absence of externally applied or actively generated internal stresses. Also, we have assumed constant cell perimeter, corresponding to $R = Tr[\mathbf{G}]$ =constant. In general, the various parameters in $\mathcal{F}_c$ will depend on R.

It is important to stress that $\tilde{G}_{ij}$ and M are not independent. The traceless tensor $\tilde{G}_{ij}$ can be written as

$$\tilde{G}_{ij} = S_G \left(n_i n_j - \frac{1}{2} \delta_{ij} \right) , \tag{5.50}$$

which defines the director field $\mathbf{n}(\mathbf{r}, t)$ associated with alignment of elongated cells and the magnitude S_G of orientational order. Cell alignment can only occur if cells are elongated ($M \neq 0$), hence $S_G(M)$ must vanish when $M = 0$. We assume $S_G = MS$, where S plays the role of a nematic order parameter for orientational order of elongated cells. Clearly,

S is defined only in states where M is finite.

Cell sheets commonly interact with a frictional substrate that eliminates momentum conservation. Frictional drag with the substrate generally exceeds inertial forces, and the Navier-Stokes equation for the momentum is replaced by a Stokes equation quantifying force balance on each fluid element. Within this overdamped limit, and considering a minimal form for the various dissipative kinetic coefficients, the tissue dynamics is governed by[2]

$$\partial_t \rho = -\nabla \cdot (\rho \mathbf{v}), \tag{5.51}$$

$$\xi v_i = -\partial_i p + \partial_j \left(\sigma^G_{ij} + \sigma^E_{ij} + \sigma^D_{ij} \right), \tag{5.52}$$

$$\frac{d}{dt} M = 2 \frac{R}{M} \tilde{G}_{ij} D_{ij} - \frac{1}{\gamma_M} \frac{\delta \mathcal{F}_c}{\delta M} - \frac{\tilde{G}_{ij}}{\gamma_2} \frac{\delta \mathcal{F}_c}{\delta \tilde{G}_{ij}} , \tag{5.53}$$

$$\begin{aligned} \frac{D}{Dt} \tilde{G}_{ij} &= R D_{ij} + \tilde{G}_{ik} D_{kj} + D_{ik} \tilde{G}_{kj} - \delta_{ij} \tilde{G}_{kl} D_{kl} \\ &- \frac{M}{\gamma_G} \frac{\delta \mathcal{F}_c}{\delta \tilde{G}_{ij}} - \frac{\tilde{G}_{ij}}{\gamma_2} \frac{\delta \mathcal{F}_c}{\delta M} , \end{aligned} \tag{5.54}$$

where ξ is the frictional drag and

$$\frac{\delta \mathcal{F}_c}{\delta M} = \left[\alpha + \beta M^2 \right] M - K \nabla^2 M , \tag{5.55}$$

$$\frac{\delta \mathcal{F}_c}{\delta \tilde{G}_{ij}} = \chi \tilde{G}_{ij} - K_G \nabla^2 \tilde{G}_{ij} \tag{5.56}$$

It is useful to consider a simplified form of the equations obtained by retaining only lowest order terms in fields and gradients. In this case the Stokes equation and the equations for the shape fields can be written in the explicit form

$$\Gamma \mathbf{v} = -\nabla p + \eta \nabla^2 \mathbf{v} + \eta_b \nabla \nabla \cdot \mathbf{v} + \nabla \cdot \sigma^G , \tag{5.57}$$

[2]We consider here uniaxial systems.

$$\frac{d}{dt}M = 2\frac{R}{M}\tilde{G}_{ij}D_{ij} - \frac{1}{\gamma_M}\left[\alpha + \beta M^2\right]M + D\nabla^2 M \ , \tag{5.58}$$

$$\begin{aligned}\frac{D}{Dt}\tilde{G}_{ij} &= RD_{ij} + \tilde{G}_{ik}D_{kj} + D_{ik}\tilde{G}_{kj} - \delta_{ij}\tilde{G}_{kl}D_{kl} \\ &- rM\tilde{G}_{ij} + D_G\nabla^2\tilde{G}_{ij} \ ,\end{aligned} \tag{5.59}$$

where $D = \Gamma_M K$, $D_G = \Gamma K_G$, $r = \chi/\gamma_G + \alpha/\gamma_2$ and

$$\sigma^G_{ij} = 2R(\alpha + \beta M^2)\tilde{G}_{ij} + \frac{1}{2}\delta_{ij}\chi S^2_G \ . \tag{5.60}$$

The single-cell anisotropy field M here plays the role of tissue fluidity. The first term on the RHS of Eq. (5.58) captures the fact that shear deformations, coupled to local cell alignment, can increase cell anisotropy, and thereby drive fluidification. The second term describes relaxation towards the ground state as controlled by the tissue free energy, with a cost for spatial variations in local fluidity controlled by the stiffness D. The reactive terms in Eq. (5.59) describe flow alignment of elongated cell shape. The term proportional to r describes changes of cell shape tensor due to dissipative processes, such as topological rearrangements, at a rate proportional to the tissue fluidity M. The last term in Eq. (5.59) describes the stiffness against deformations of local cell alignment. The prefactor to $\tilde{G}_{ij}$ in Eq. (5.60) represents the zero-frequency tissue shear modulus and vanishes at the transition point, corresponding to fluidization of the tissue.

Finally, in a confluent tissue the cell number density $n = \rho/m_c$ is slaved to the mean cell area $\langle A_\alpha \rangle$ with $n = 1/\langle A_\alpha \rangle$. For cells that are only slightly deformed from regular polygons, $\langle A_\alpha \rangle \simeq \sqrt{\det[\mathbf{G}]} \approx \mathrm{Tr}[\mathbf{G}]$, where we have used Eq. (5.65). The density equation, Eq (5.51), can therefore equivalently be written as an equation for the cell area

or for $|G| \equiv \det[\mathbf{G}]$, given by

$$(\partial_t + \mathbf{v} \cdot \nabla) |G| = |G| \nabla \cdot \mathbf{v} \, . \tag{5.61}$$

5.5 Conclusion

Using the Poisson-bracket formalism, we have derived hydrodynamic equations for a fluid of deformable particles in two dimensions. Shape fluctuations are described by two continuum fields: (i) a coarse-grained scalar field that captures single-particle anisotropy, and (ii) a shape tensor field that quantifies both particle elongation and nematic alignment of elongated particles.

We have specifically applied the model to sheets of dense biological tissue, where, as discussed in chapters 1 and 2, the onset of single-cell anisotropy is identified as an order parameter for a solid-liquid transition driven by the interplay of cortex contractility and cell-cell adhesion [48, 39]. In other words, in confluent tissue single-cell anisotropy is effectively an experimentally accessible measure of the rheological properties of the tissue, with isotropic cell shapes identifying the solid or jammed state and anisotropic shapes corresponding to a liquid. Previous work has examined the dynamics of a coarse-grained cell shape tensor and its coupling to mechanical stresses [76]. This work did not, however, distinguish between a tissue of elongated, but isotropically oriented cells and one where the cells are elongated and also aligned in a state with nematic liquid crystalline order. The new ingredient of the work presented in this chapter is to distinguish the dynamics of tissue fluidity, as quantified by the single-cell anisotropy field, from that of cell-cell alignment, and examine the interplay between flow, which can be either externally applied or induced by internal active processes, fluidity and possible nematic order of cell shapes. The equations detailed within this chapter hence provide a starting point

for quantifying the rheology of biological tissue. Future extension needed to develop a complete framework of tissue rheology include the coupling to the dynamics of polarized cell motility and the inclusion of structural rearrangements arising from cell division and death. Additionally, these equations can be further modified to incorporate how imposed deformations shift the transition between solid and fluid states as explained in chapter 4 where we saw how compression/dilation can shift the vertex model between solid and floppy states, as well as the finite shearing which can rigidify a fluidized vertex model [125].

Finally, the equations developed here provide a hydrodynamic model for fluids of deformable particles, capable of accounting for both the dynamics of small shape deformations and density changes.

Appendix 3.A Useful identities

The eigenvalues of a 2×2 symmetric matrix G_{ij} are given by

$$\lambda_{1,2} = \frac{1}{2}(G_{xx} + G_{yy}) \pm \frac{1}{2}\sqrt{(G_{xx} - G_{yy})^2 + 4G_{xy}^2}\,, \tag{5.62}$$

and

$$\lambda_1 - \lambda_2 = \sqrt{(G_{xx} - G_{yy})^2 + 4G_{xy}^2}\,, \tag{5.63}$$

$$\lambda_1 \lambda_2 = G_{xx}G_{yy} - G_{xy}^2\,. \tag{5.64}$$

One can straightforwardly then show that the following identities hold

$$(\lambda_1 - \lambda_2)^2 = [\mathrm{Tr}\mathbf{G}]^2 - 4\det\mathbf{G}\,, \tag{5.65}$$

$$(\lambda_1 - \lambda_2)^2 = 2\mathrm{Tr}[\mathbf{G}^2] - [\mathrm{Tr}\mathbf{G}]^2 = 2\mathrm{Tr}[\tilde{\mathbf{G}}^2]\,. \tag{5.66}$$

Finally, for a regular polygon, G_{ij} is always diagonal and thus $\lambda_1 = \lambda_2 = \lambda$. In this case Eq. (5.65) gives $\mathrm{Tr}\mathbf{G} = 2\sqrt{\det \mathbf{G}}$. For small deformations from a regular polygon $\mathrm{Tr}\mathbf{G} \sim 2\sqrt{\det \mathbf{G}}$, which implies that we can think of $\mathrm{Tr}\mathbf{G}$ as either a measure of square of cell perimeter or a measure of cell area.

Appendix 3.B Elastic Stress and Pressure

It is convenient to rewrite some of the term in the reactive part $\mathbf{V}^g$ of the momentum density equation given in Eq. (5.21) to express them as gradients of pressure and an elastic stress. The goal is to rewrite the following terms

$$\delta V_i^g \equiv -\rho\partial_i \frac{\delta \mathcal{F}_V}{\delta \rho} + (\partial_i M)\frac{\delta \mathcal{F}_V}{\delta M} + (\partial_i G_{kl})\,\frac{\delta \mathcal{F}_V}{\delta G_{kl}}\,. \tag{5.67}$$

By relating functional derivatives of $\mathcal{F}_V$ to derivatives of the free energy density f, which is a function of the hydrodynamic fields and their gradients, we can write

$$-\rho\nabla_i \frac{\delta \mathcal{F}_V}{\delta \rho} = -\nabla_i\left(\rho\frac{\partial f}{\partial \rho}\right) + \frac{\partial f}{\partial \rho}\nabla_i \rho\,, \tag{5.68}$$

$$\begin{aligned}(\nabla_i M)\frac{\delta \mathcal{F}_V}{\delta M} &= (\nabla_i M)\left(\frac{\partial f}{\partial M} - \nabla_j \frac{\partial f}{\partial \nabla_j M}\right)\\ &= \frac{\partial f}{\partial M}\nabla_i M - \nabla_j\left[(\nabla_i M)\frac{\partial f}{\partial \nabla_j M}\right] + \frac{\partial f}{\partial \nabla_j M}\nabla_i(\nabla_j M)\,,\end{aligned} \tag{5.69}$$

$$\begin{aligned}(\nabla_i G_{kl})\,\frac{\delta \mathcal{F}_V}{\delta G_{kl}} &= (\nabla_i G_{kl})\left(\frac{\partial f}{\partial G_{kl}} - \nabla_j \frac{\partial f}{\partial \nabla_j G_{kl}}\right)\\ &= \frac{\partial f}{\partial G_{kl}}\nabla_i G_{kl} - \nabla_j\left[(\nabla_i G_{kl})\frac{\partial f}{\partial \nabla_j G_{kl}}\right] + \frac{\partial f}{\partial \nabla_j G_{kl}}\nabla_i(\nabla_j G_{kl}).\end{aligned} \tag{5.70}$$

Combining these three terms, and using

$$\nabla_i f = \frac{\partial f}{\partial \rho}\nabla_i \rho + \frac{\partial f}{\partial M}\nabla_i M + \frac{\partial f}{\partial \nabla_j M}\nabla_i(\nabla_j M) + \frac{\partial f}{\partial G_{kl}}\nabla_i G_{kl} + \frac{\partial f}{\partial \nabla_j G_{kl}}\nabla_i(\nabla_j G_{kl}) \tag{5.71}$$

we can write

$$\delta V_i^g = -\nabla_i p + \nabla_j \sigma_{ij}^E \tag{5.72}$$

in terms of the pressure p and an elastic stress σ_{ij}^E, given by

$$p = \rho\frac{\partial f}{\partial \rho} - f \ , \tag{5.73}$$

$$\sigma_{ij}^E = -\frac{\partial f}{\partial \nabla_j M}\nabla_i M - \frac{\partial f}{\partial \nabla_j G_{kl}}\nabla_i G_{kl} \ . \tag{5.74}$$

The stress σ_{ij}^E plays the role of the Ericksen stress of nematic liquid crystals.

Appendix 3.C Evaluation of Poisson-brackets

First we show the details of the calculation of the fundamental PB $\{G_{ij}^\alpha \delta(\mathbf{r}-\mathbf{r}^\alpha), g_k(\mathbf{r}')\}$. To evaluate the PB we use the following

$$\frac{\partial \Delta x_i^{\alpha\nu}}{\partial x_j^{\beta\mu}} = \delta^{\alpha\beta}\delta_{ij}\left(\delta^{\mu\nu} - \frac{1}{n}\right) \ , \tag{5.75}$$

$$\frac{\partial}{\partial x_j^{\beta\mu}}\delta(\mathbf{r}-\mathbf{r}^\alpha) = -\frac{\delta^{\alpha\beta}}{n}\partial_j \delta(\mathbf{r}-\mathbf{r}^\alpha) \ , \tag{5.76}$$

$$\begin{aligned}\delta(\mathbf{r}-\mathbf{r}^\alpha) &= \delta(\mathbf{r}-\mathbf{r}^{\alpha\mu}-\Delta\mathbf{r}^{\alpha\mu}) \\ &= \delta(\mathbf{r}-\mathbf{r}^\alpha) - \Delta x_i^{\alpha\mu}\partial_i\delta(\mathbf{r}-\mathbf{r}^{\alpha\mu}) + \mathcal{O}(\Delta x^2\nabla^2) \ .\end{aligned} \tag{5.77}$$

We write

$$\{G_{ij}^{\alpha}\delta(\mathbf{r}-\mathbf{r}^{\alpha}),g_k(\mathbf{r}')\}=-\sum_{\beta,\nu}\frac{\partial G_{ij}^{\alpha}\delta(\mathbf{r}-\mathbf{r}^{\alpha})}{\partial x_k^{\beta\nu}}\delta(\mathbf{r}'-\mathbf{r}^{\beta\nu})\ . \tag{5.78}$$

Then

$$\frac{\partial G_{ij}^{\alpha}\delta(\mathbf{r}-\mathbf{r}^{\alpha})}{\partial x_k^{\beta\nu}}=-\frac{1}{n}\delta^{\alpha\beta}G_{ij}^{\alpha}\partial_k\delta(\mathbf{r}-\mathbf{r}^{\alpha})+\frac{1}{n}\delta^{\alpha\beta}\delta(\mathbf{r}-\mathbf{r}^{\alpha})\left(\delta_{ik}\Delta x_j^{\alpha\nu}+\delta_{jk}\Delta x_i^{\alpha\nu}\right)\ . \tag{5.79}$$

Inserting Eq.(C5) into Eq.(C4) and using that $\sum_{\mu}\Delta\mathbf{r}^{\alpha\mu}=0$, we obtain

$$\begin{aligned}\{G_{ij}^{\alpha}\delta(\mathbf{r}-\mathbf{r}^{\alpha}),g_k(\mathbf{r}')\}&=G_{ij}^{\alpha}\left[\partial_k\delta(\mathbf{r}-\mathbf{r}^{\alpha})\right]\frac{1}{n}\sum_{\nu}\delta(\mathbf{r}'-\mathbf{r}^{\alpha\nu})\\&-\delta(\mathbf{r}-\mathbf{r}^{\alpha})\frac{1}{n}\sum_{\nu}\left[\delta_{ik}\Delta x_j^{\alpha\nu}+\delta_{jk}\Delta x_i^{\alpha\nu}\right]\delta(\mathbf{r}'-\mathbf{r}^{\alpha\nu})\ .\end{aligned} \tag{5.80}$$

Finally, using

$$\begin{aligned}\delta(\mathbf{r}-\mathbf{r}^{\alpha\nu})\quad&=\delta(\mathbf{r}-\mathbf{r}^{\alpha}-\Delta\mathbf{r}^{\alpha\nu})\\&\approx\delta(\mathbf{r}-\mathbf{r}^{\alpha})-\Delta x_k^{\alpha\nu}\partial_k\delta(\mathbf{r}-\mathbf{r}^{\alpha})\ ,\end{aligned} \tag{5.81}$$

we obtain

$$\begin{aligned}\{G_{ij}^{\alpha}\delta(\mathbf{r}-\mathbf{r}^{\alpha}),g_k(\mathbf{r}')\}&=G_{ij}^{\alpha}\delta(\mathbf{r}'-\mathbf{r}^{\alpha})\partial_k\delta(\mathbf{r}-\mathbf{r}^{\alpha})\\&+\delta(\mathbf{r}-\mathbf{r}^{\alpha})\left[\delta_{ik}G_{jl}^{\alpha}+\delta_{jk}G_{il}^{\alpha}\right]\partial_l'\delta(\mathbf{r}'-\mathbf{r}^{\alpha})\ .\end{aligned} \tag{5.82}$$

From this one can immediately obtain Eq. (5.15).

To evaluate the PB $\{M(\mathbf{r}),g_k(\mathbf{r}')\}$ we let $G_{ij}^{\alpha}=\frac{I_\alpha}{2}\delta_{ij}+\tilde{G}_{ij}^{\alpha}$, with $I_\alpha=\hat{G}_{kk}^{\alpha}$ and

$\tilde{G}^\alpha_{ij} = M_\alpha \left(\nu^\alpha_i \nu^\alpha_j - \frac{1}{2}\delta_{ij}\right)$ and use the following identities

$$\tilde{G}^\alpha_{ik}\tilde{G}^\alpha_{kj} = \frac{M^2_\alpha}{4}\delta_{ij} \,, \tag{5.83}$$

$$\tilde{G}^\alpha_{ik}\tilde{G}^\alpha_{ki} = \frac{M^2_\alpha}{2} \,. \tag{5.84}$$

We can then write

$$M_\alpha\{M_\alpha\delta(\mathbf{r}-\mathbf{r}^\alpha), g_k(\mathbf{r}')\} = 2\tilde{G}^\alpha_{ij}\{\tilde{G}^\alpha_{ij}\delta(\mathbf{r}-\mathbf{r}^\alpha), g_k(\mathbf{r}')\} \,. \tag{5.85}$$

Using Eq. (5.82), we find[3]

$$\begin{aligned}
\{\tilde{G}^\alpha_{ij}\delta(\mathbf{r}-\mathbf{r}^\alpha), g_k(\mathbf{r}')\} &= \tilde{G}^\alpha_{ij}\delta(\mathbf{r}'-\mathbf{r}^\alpha)\partial_k\delta(\mathbf{r}-\mathbf{r}^\alpha) \\
&+\delta(\mathbf{r}-\mathbf{r}^\alpha)\left[\delta_{ik}\tilde{G}^\alpha_{jl} + \delta_{jk}\tilde{G}^\alpha_{il} - \delta_{ij}\tilde{G}^\alpha_{kl}\right]\partial'_l\delta(\mathbf{r}'-\mathbf{r}^\alpha) \\
&+\frac{I_\alpha}{2}\left(\delta_{ik}\delta_{jl} + \delta_{jk}\delta_{il} - \delta_{ij}\delta_{kl}\right)\delta(\mathbf{r}-\mathbf{r}^\alpha)\partial'_l\delta(\mathbf{r}'-\mathbf{r}^\alpha).
\end{aligned} \tag{5.86}$$

and

$$\begin{aligned}
\{M_\alpha\delta(\mathbf{r}-\mathbf{r}^\alpha), g_k(\mathbf{r}')\} &= M_\alpha\delta(\mathbf{r}'-\mathbf{r}^\alpha)\partial_k\delta(\mathbf{r}-\mathbf{r}^\alpha) + M_\alpha\delta(\mathbf{r}-\mathbf{r}^\alpha)\partial'_k\delta(\mathbf{r}'-\mathbf{r}^\alpha) \\
&+\frac{2I_\alpha\tilde{G}^\alpha_{kl}}{M_\alpha}\delta(\mathbf{r}-\mathbf{r}^\alpha)\partial'_l\delta(\mathbf{r}'-\mathbf{r}^\alpha) \,.
\end{aligned} \tag{5.87}$$

The PB $\{M(\mathbf{r}), g_k(\mathbf{r}')\}$ is then given by

$$\{M(\mathbf{r}), g_k(\mathbf{r}')\} = \delta(\mathbf{r}-\mathbf{r}')\partial_k M(\mathbf{r}) - 2\left[\sum_\alpha \frac{I_\alpha\tilde{G}^\alpha_{kl}}{M_\alpha}\delta(\mathbf{r}-\mathbf{r}^\alpha)\right]\partial_l\delta(\mathbf{r}-\mathbf{r}') \tag{5.88}$$

[3]Note that the PB of $\tilde{G}_{ij}$ given below is the same as the PB of the quantity R_{ij} of Ref. [181], albeit in 2D instead of 3D.

and involves a new field

$$\sum_\alpha \frac{I_\alpha \tilde{G}^\alpha_{kl}}{M_\alpha}\delta(\mathbf{r}-\mathbf{r}^\alpha) = \sum_\alpha I_\alpha \left(\nu^\alpha_i \nu^\alpha_j - \frac{1}{2}\delta_{ij}\right)\delta(\mathbf{r}-\mathbf{r}^\alpha)\ . \tag{5.89}$$

We will need to make approximations to close the equations. We will approximate as follows

$$\sum_\alpha \frac{I_\alpha \tilde{G}^\alpha_{kl}}{M_\alpha}\delta(\mathbf{r}-\mathbf{r}^\alpha) \approx \frac{R(\mathbf{r})\tilde{G}_{ij}(\mathbf{r})}{M(\mathbf{r})}\ . \tag{5.90}$$

Appendix 3.D Mean Field theory of Vertex Model

Following [78], we construct a mean-field free energy by rewriting the *single-cell* Vertex model energy in terms of the cell anisotropy parameter M_α. We then cast a Landau type expansion of the energy in powers of cell anisotropy, and find that the harmonic coefficient may be tuned by target shape index s_0 which serves as the "temperature" parameter. Let us define

$$M_\alpha = \lambda^\alpha_1 - \lambda^\alpha_2\ , \tag{5.91}$$

$$R_\alpha = \lambda^\alpha_1 + \lambda^\alpha_2\ , \tag{5.92}$$

which gives $\lambda^\alpha_{1,2} = (R_\alpha \pm M_\alpha)/2$. Equations (5.6) and (5.7) are exact for regular polygons, but also hold approximately true for slightly deformed polygons where the shape tensor remains diagonal and $M_\alpha/R_\alpha \ll 1$. We can then write

$$P_\alpha \approx \sqrt{2}n\sin\left(\frac{\pi}{n}\right)\left(\sqrt{\lambda^\alpha_1+\lambda^\alpha_2}\right) \equiv \tilde{\nu}(n)\sqrt{R_\alpha}\ , \tag{5.93}$$

$$A_\alpha = \frac{n}{2}\sin\left(\frac{2\pi}{n}\right)\sqrt{\lambda^\alpha_1\lambda^\alpha_2} \equiv \frac{\tilde{\mu}(n)}{2}\sqrt{R^2_\alpha - M^2_\alpha}\ . \tag{5.94}$$

The single-cell energy can then be written in terms of R_α and M_α as

$$E_\alpha = \frac{K_A}{2}\left(\frac{\tilde{\mu}}{2}\sqrt{R_\alpha^2 - M_\alpha^2} - A_0\right)^2 + \frac{K_P}{2}(P_\alpha - P_0)^2 \,. \tag{5.95}$$

Following [78], we restrict ourselves to small deformations from a regular polygon and expand $M_\alpha/R_\alpha \ll 1$, with the result

$$\begin{aligned} E_\alpha \quad &= \frac{K_A}{2}\Bigg[\left(\frac{\tilde{\mu}R_\alpha}{2} - A_0\right)^2 + \frac{1}{2}R\tilde{\mu}\left(A_0 - \frac{R\tilde{\mu}}{2}\right)\left(\frac{M_\alpha}{R_\alpha}\right)^2 \\ &\quad + \frac{R\tilde{\mu}}{8}A_0\left(\frac{M_\alpha}{R_\alpha}\right)^4 + \mathcal{O}\left(\left(\frac{M_\alpha}{R_\alpha}\right)^6\right)\Bigg] \\ &\quad + \frac{K_P}{2}\left(\tilde{\nu}\sqrt{R_\alpha} - P_0\right)^2 \,. \end{aligned} \tag{5.96}$$

We further assume that the cell perimeter is constant, or $P_\alpha = P_0$, hence $R_\alpha = P_0^2/\tilde{\nu}^2$. Substituting into Eq. (5.96), we can rewrite the single-cell energy density $e_\alpha = E_\alpha/A_0$ as

$$e_\alpha = e_0 + \frac{1}{2}\alpha(n, s_0)\left(\frac{M_\alpha}{A_0}\right)^2 + \frac{1}{4}\beta(n, s_0)\left(\frac{M_\alpha}{A_0}\right)^4 \,, \tag{5.97}$$

where e_0 is a constant and

$$\alpha(n, s_0) = \frac{\kappa_A A_0^2 \tilde{\mu}^2}{4 s_0^2}\left(s_0^{*2} - s_0^2\right) \,, \tag{5.98}$$

$$\beta(n, s_0) = \frac{\kappa_a A_0^4 \tilde{\mu}\tilde{\nu}^6}{4 s_0^6} \,, \tag{5.99}$$

with $s_0 = P_0/\sqrt{A_0}$ the shape index, our tuning parameter. Also, $\alpha(n, s_0)$ has been written in terms of the critical shape index,

$$s_0^* = \tilde{\nu}\sqrt{\frac{2}{\tilde{\mu}}} = \sqrt{4n\tan(\pi/n)} \,. \tag{5.100}$$

The limits of these approximations where tested numerically in Ref. [78], where it was shown that Eq. (5.97) provides a good description of the model near the transition point, where cells are only minimally deformed.

More familiar particulate systems can be tuned between solid and liquid states by changing the density or packing fraction. As discussed in more detail in chapter 1 and 2, confluent tissues have a packing fraction of unity, but nonetheless can be tuned between liquid and solid states by changing the target shape index s_0 that measures the target cell perimeter in units of the target cell area. For $s_0 < s_0^*$ the system is frustrated as cells cannot reach both their target area and perimeter, resulting in finite energy barriers for cellular rearrangements, and the tissue is a solid [47, 48]. For $s_0 > s_0^*$ such energy barriers vanish and cells easily exchange neighbors, resulting in a liquid-like state.

Recall from chapter 1 that the value of critical target shape index s_0^* depends on the specific undeformed polygonal shape, with $s_0^* = 4$ for squares and $s_0^* = 2\sqrt{2\sqrt{3}} \approx 3.722$ for hexagons. Eq. (5.98) shows explicitly that α changes sign at $s_0 = s_0^*$, while $\beta > 0$. For $\alpha > 0$ the stable ground state has $M = 0$ and corresponds to a solid-like state of isotropic cells. For $\alpha < 0$ the stable ground state is a fluid of anisotropic cells, with $M/A_0 = \pm\sqrt{-\alpha/\beta}$. At $\alpha = 0$ the system undergoes spontaneous symmetry breaking and fluidizes, choosing one of two equivalent axial direction along which to elongate. Here we have defined M as positive by assuming $\lambda_1 > \lambda_2$, hence breaking from the outside the Ising symmetry of the model.

The nature of this solid-liquid transition has been discussed in the context of Voronoi and Vertex model simulation, where a continuous transition results in fluidization at constant density, as quantified through measurements of energy barriers and mean-square displacement. [48, 39].

Finally, it was shown in Ref. [78] that the quartic form given in Eq. (5.97) is also obtained by assuming constant cell area, albeit with different expressions for the coeffi-

cients α and β. In both cases the coefficient α changes sign at $s_0 = s_0^*$ and the behavior near the transition is unaffected by the approximation used.

Appendix 3.E Derivation of Eqs. 5.6 and 5.7

The shape tensor approximates a polygonal cell, labeled by α, as an ellipse defined by,

$$(\mathbf{r}^\alpha - \mathbf{r}_\mathbf{C}^\alpha) \cdot (\mathbf{G}^\alpha)^{-1} (\mathbf{r}^\alpha - \mathbf{r}_\mathbf{C}^\alpha)^T = 1 \ , \tag{5.101}$$

where $\mathbf{r}_C^\alpha$ is the center of the cell. In a coordinate basis where the tensor is diagonal the equation for the cell boundary is given by

$$\frac{(x - x_0)^2}{\lambda_1} + \frac{(y - y_0)^2}{\lambda_2} = 1 \ , \tag{5.102}$$

where $1/\lambda_{1,2}^2$ are the eigenvalues of $\mathbf{G}^{\alpha^{-1}}$ and determine the major and minor semi-axes of the ellipse. For a regular polygon we have $\lambda_1 = \lambda_2 = R^2$, and Eq. (5.102) reduces to the equations for a circle of radius R. Consider a regular n-sided polygon with edges ℓ circumscribed in a circle of radius R, as illustrated in Fig. 5.2. The polygon has a total interior angle of $(n-2)\pi$. The angle between any two neighboring edges is $\varphi = \frac{(n-2)\pi}{n}$ and the central angle is given by $\theta = \frac{2\pi}{n}$. Elementary trigonometry then yields the following relationships:

$$P = n\ell = 2nR \sin\left(\frac{\pi}{n}\right) \ , \tag{5.103}$$

$$A = \frac{n}{2} \sin\left(\frac{2\pi}{n}\right) R^2 \ . \tag{5.104}$$

For regular polygons the eigenvalues of the shape tensor are equal, with $\lambda_1 = \lambda_2 = R^2$, and Eqs. (5.104) and (5.103) can be recast in the forms given in Eqs. (5.6) and (5.7) for the area and perimeter of regular polygons. Although Eq. (5.7) does not hold for general

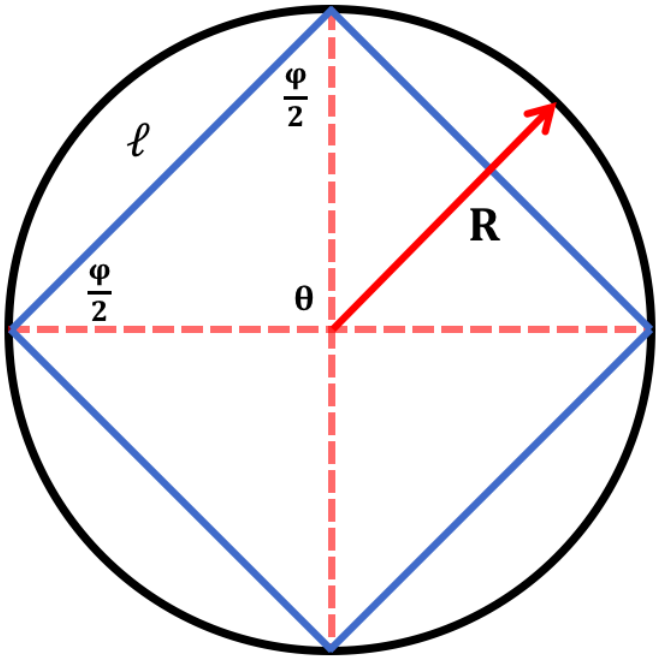

Figure 5.2—Regular polygon, of side ℓ circumscribed inside a circle of radius R.

deformed ellipses, it is the first order approximation of the exact expression given by a hypergeometric function and has been validated numerically for small deformations [76, 188].

Chapter 6

Conclusions

In this thesis I have discussed theoretical work on the vertex model in its most simple incarnation, neglecting mechanical-chemical feedback, cell motility, and topological rearrangements, and instead focused on its purely geometric aspects. Making use of a mean field approach my collaborators and I showed that the model encodes novel mechanical proprieties. This includes the rigidity transition as tuned by the target shape index s_0, but we also find that the linear elasticity of the model can encode auxetic behavior, robust non-affinity in response to even for infinitesmial strains, and tunable elasticity depending on parameters (s_0, r). The tunability of the elastic constants, as reflected by the Young's and bulk modulus, highlights that the solid proprieties of the vertex model are not reflected in the network topology, as would be the case for a conventional system of masses and springs. Instead the mechanical properties are controlled by self-tension due to geometrical frustration of cell shape.

We also showed that the vertex model energy does not admit a conventional Taylor series expansion about a reference state, and is non-analytic at the solid-floppy transition point. The model does not encode a unique reference state, as target perimeter and target area can never fix a unique cell shape. While the solid phase of the model does

exhibit a unique energy ground state, corresponding to a pre-stressed frustrated state, this is not a true reference state. The model, instead, contains hidden degrees of freedom related to the inherent shape degeneracy of the energy, and thus there is, in principle, a continuous family of degenerate reference states for a single cell in both solid and floppy phases. This continuous family of reference states was incorporated into the mean field approach as additional degrees of freedom by direct parametrization. The additional degrees of freedom are responsible for the floppy, fluid-like mechanical response in the compatible/fluid phase ($s_0 \geq s_0^*$), as well as the non-affinity of the mechanical response in the incompatible/solid phase ($s_0 < s_0^*$) whereby shape degeneracy encodes non-affine pathways by which cells may accommodate imposed deformations. They are also responsible the anomalous coupling between shear and compression modes at $s_0 = s_0^*$, which cannot be predicted *a priori* from structural analysis of the cell network.

Incorporating these additional degrees of freedom are essential to capture the non-linear mechanical response of the model to finite deformations. We found that isotropic compression and dilation shift the transition point s_0^*: finite compression will make an initially rigid system floppy, whereas finite dilation will exhaust shape degeneracy of cells and thereby make an initially floppy system become spontaneously rigid. A similar mean field approach showed that an initially floppy vertex model can exhibit shear-thickening, where finite shearing exhausts shape degeneracy and results in rigidification [125]. Furthermore, we were able to utilize our mean field study to make a prediction on how intrinsic curvature can also shift the transition point s_0^* by treating curvature as an effective compression/dilation on the tissue.

In the studies reported in chapters 2, 3, and 4 on the nonlinear response, as well as the work in Ref. [125], the mean field model was able to make predictions supported by simulations which exhibit varying degrees of inhomogeneities between cells. Perhaps the most surprising success is indicated in Figure 4.2 back in chapter 4 where the mean field

model predicts the shift of the transition point between solid-like and fluid-like phases due to curvature for a disordered vertex model simulated on a sphere, a scenario where none of the mean field assumptions hold.

A natural next step is formulating a faithful continuum description of the vertex model which incorporates the novel elasticity to shape degeneracy studied in this thesis. In particular, the bifurcation between solid-like and fluid-like phases as mediated by external deformations. To the author's knowledge, the most successful continuum description which consistently incorporates the dual solid-like and fluid-like phases of the vertex model is the work by Fielding et al [79], which unfortunately is not a closed model[1].

A study done in Ref.[189, 190] has shown that modified elasticity field equations can capture anomalous elasticity in amorphous solids by including additions terms which can model plastic events tied to quadrupole and dipole interactions. Perhaps a similar route may be useful for developing a faithful continuum formulation of the vertex model, and is the a framework I plan to pursue in future work.

[1]The model in this paper is not closed in the sense that the form of the stress is prescribed rather than directly integrated with other dynamical equations via a force-balance equation.

Bibliography

[1] N. Özkaya, D. Leger, D. Goldsheyder, and M. Nordin, *Fundamentals of biomechanics: equilibrium, motion, and deformation*. Springer, 2016.

[2] A. Goriely, *The mathematics and mechanics of biological growth*, vol. 45. Springer, 2017.

[3] S. E. Spagnolie, *Complex fluids in biological systems*, *Biological and Medical Physics, Biomedical Engineering* (2015).

[4] J.-F. Sadoc and R. Mosseri, *Geometrical frustration*. 1999.

[5] A. C. Martin, M. Kaschube, and E. F. Wieschaus, *Pulsed contractions of an actin–myosin network drive apical constriction*, *Nature* **457** (2009), no. 7228 495–499.

[6] R. Etournay, M. Popović, M. Merkel, A. Nandi, C. Blasse, B. Aigouy, H. Brandl, G. Myers, G. Salbreux, F. Jülicher, *et. al.*, *Interplay of cell dynamics and epithelial tension during morphogenesis of the drosophila pupal wing*, *Elife* **4** (2015) e07090.

[7] S. J. Streichan, M. F. Lefebvre, N. Noll, E. F. Wieschaus, and B. I. Shraiman, *Global morphogenetic flow is accurately predicted by the spatial distribution of myosin motors*, *Elife* **7** (2018) e27454.

[8] E. Maniou, M. F. Staddon, A. R. Marshall, N. D. Greene, A. J. Copp, S. Banerjee, and G. L. Galea, *Hindbrain neuropore tissue geometry determines asymmetric cell-mediated closure dynamics in mouse embryos*, *Proceedings of the National Academy of Sciences* **118** (2021), no. 19 e2023163118.

[9] M. Poujade, E. Grasland-Mongrain, A. Hertzog, J. Jouanneau, P. Chavrier, B. Ladoux, A. Buguin, and P. Silberzan, *Collective migration of an epithelial monolayer in response to a model wound*, *Proceedings of the National Academy of Sciences* **104** (2007), no. 41 15988–15993.

[10] A. Brugués, E. Anon, V. Conte, J. H. Veldhuis, M. Gupta, J. Colombelli, J. J. Muñoz, G. W. Brodland, B. Ladoux, and X. Trepat, *Forces driving epithelial wound healing*, *Nature physics* **10** (2014), no. 9 683–690.

[11] R. J. Tetley, M. F. Staddon, D. Heller, A. Hoppe, S. Banerjee, and Y. Mao, *Tissue fluidity promotes epithelial wound healing*, *Nature physics* **15** (2019), no. 11 1195–1203.

[12] V. Ajeti, A. P. Tabatabai, A. J. Fleszar, M. F. Staddon, D. S. Seara, C. Suarez, M. S. Yousafzai, D. Bi, D. R. Kovar, S. Banerjee, *et. al.*, *Wound healing coordinates actin architectures to regulate mechanical work*, *Nature physics* **15** (2019), no. 7 696–705.

[13] P. Friedl and D. Gilmour, *Collective cell migration in morphogenesis, regeneration and cancer*, *Nature reviews Molecular cell biology* **10** (2009), no. 7 445–457.

[14] E. Paluch and C.-P. Heisenberg, *Biology and physics of cell shape changes in development*, *Current Biology* **19** (2009), no. 17 R790–R799.

[15] E. N. Arwert, E. Hoste, and F. M. Watt, *Epithelial stem cells, wound healing and cancer*, *Nature Reviews Cancer* **12** (2012), no. 3 170–180.

[16] B. D. Hoffman and J. C. Crocker, *Cell mechanics: dissecting the physical responses of cells to force*, *Annual review of biomedical engineering* **11** (2009) 259–288.

[17] T. Mitchison and L. Cramer, *Actin-based cell motility and cell locomotion*, *Cell* **84** (1996), no. 3 371–379.

[18] R. J. Petrie and K. M. Yamada, *Fibroblasts lead the way: a unified view of 3d cell motility*, *Trends in cell biology* **25** (2015), no. 11 666–674.

[19] E. Lawson-Keister and M. L. Manning, *Jamming and arrest of cell motion in biological tissues*, *Current Opinion in Cell Biology* **72** (2021) 146–155.

[20] M. Sadati, N. T. Qazvini, R. Krishnan, C. Y. Park, and J. J. Fredberg, *Collective migration and cell jamming*, *Differentiation* **86** (2013), no. 3 121–125.

[21] L. Atia, J. J. Fredberg, N. S. Gov, and A. F. Pegoraro, *Are cell jamming and unjamming essential in tissue development?*, *Cells & development* **168** (2021) 203727.

[22] L. Atia, D. Bi, Y. Sharma, J. A. Mitchel, B. Gweon, S. A. Koehler, S. J. DeCamp, B. Lan, J. H. Kim, R. Hirsch, *et. al.*, *Geometric constraints during epithelial jamming*, *Nature physics* **14** (2018), no. 6 613–620.

[23] T. Stern, S. Y. Shvartsman, and E. F. Wieschaus, *Deconstructing gastrulation at single-cell resolution*, *Current Biology* **32** (2022), no. 8 1861–1868.

[24] S. B. Lemke and C. M. Nelson, *Dynamic changes in epithelial cell packing during tissue morphogenesis*, *Current Biology* **31** (2021), no. 18 R1098–R1110.

[25] B. Alberts, *Molecular biology of the cell*. Garland science, 2017.

[26] R. Kalluri, R. A. Weinberg, *et. al.*, *The basics of epithelial-mesenchymal transition*, *The Journal of clinical investigation* **119** (2009), no. 6 1420–1428.

[27] S. Kim, M. Pochitaloff, G. A. Stooke-Vaughan, and O. Campàs, *Embryonic tissues as active foams*, *Nature physics* **17** (2021), no. 7 859–866.

[28] E. Frittoli, A. Palamidessi, F. Iannelli, F. Zanardi, S. Villa, L. Barzaghi, H. Abdo, V. Cancila, G. V. Beznoussenko, G. Della Chiara, *et. al.*, *Tissue fluidification promotes a cgas–sting cytosolic dna response in invasive breast cancer*, *Nature materials* **22** (2023), no. 5 644–655.

[29] G. Follain, D. Herrmann, S. Harlepp, V. Hyenne, N. Osmani, S. C. Warren, P. Timpson, and J. G. Goetz, *Fluids and their mechanics in tumour transit: shaping metastasis*, *Nature Reviews Cancer* **20** (2020), no. 2 107–124.

[30] J.-A. Park, J. H. Kim, D. Bi, J. A. Mitchel, N. T. Qazvini, K. Tantisira, C. Y. Park, M. McGill, S.-H. Kim, B. Gweon, *et. al.*, *Unjamming and cell shape in the asthmatic airway epithelium*, *Nature materials* **14** (2015), no. 10 1040–1048.

[31] J. A. Mitchel, A. Das, M. J. O'Sullivan, I. T. Stancil, S. J. DeCamp, S. Koehler, O. H. Ocaña, J. P. Butler, J. J. Fredberg, M. A. Nieto, *et. al.*, *In primary airway epithelial cells, the unjamming transition is distinct from the epithelial-to-mesenchymal transition*, *Nature communications* **11** (2020), no. 1 5053.

[32] B. G. Godard and C.-P. Heisenberg, *Cell division and tissue mechanics*, *Current opinion in cell biology* **60** (2019) 114–120.

[33] A. Puliafito, L. Hufnagel, P. Neveu, S. Streichan, A. Sigal, D. K. Fygenson, and B. I. Shraiman, *Collective and single cell behavior in epithelial contact inhibition*, *Proceedings of the National Academy of Sciences* **109** (2012), no. 3 739–744.

[34] M. Abercrombie, *Contact inhibition in tissue culture*, *In vitro* **6** (1970), no. 2 128–142.

[35] T. E. Angelini, E. Hannezo, X. Trepat, M. Marquez, J. J. Fredberg, and D. A. Weitz, *Glass-like dynamics of collective cell migration*, *Proceedings of the National Academy of Sciences* **108** (2011), no. 12 4714–4719.

[36] A. Mongera, P. Rowghanian, H. J. Gustafson, E. Shelton, D. A. Kealhofer, E. K. Carn, F. Serwane, A. A. Lucio, J. Giammona, and O. Campàs *Nature* **561** (2018), no. 7723 401–405.

[37] M. Krajnc, *Solid–fluid transition and cell sorting in epithelia with junctional tension fluctuations*, *Soft Matter* **16** (2020), no. 13 3209–3215.

[38] M. Krajnc, T. Stern, and C. Zankoc, *Active instability of cell-cell junctions at the onset of tissue fluidity*, *arXiv preprint arXiv:2101.07058* (2021).

[39] D. Bi, X. Yang, M. C. Marchetti, and M. L. Manning *Physical Review X* **6** (2016), no. 2 021011.

[40] C. Malinverno, S. Corallino, F. Giavazzi, M. Bergert, Q. Li, M. Leoni, A. Disanza, E. Frittoli, A. Oldani, E. Martini, *et. al.*, *Endocytic reawakening of motility in jammed epithelia*, *Nature materials* **16** (2017), no. 5 587–596.

[41] N. I. Petridou, B. Corominas-Murtra, C.-P. Heisenberg, and E. Hannezo, *Rigidity percolation uncovers a structural basis for embryonic tissue phase transitions*, *Cell* **184** (2021), no. 7 1914–1928.

[42] O. Ilina, P. G. Gritsenko, S. Syga, J. Lippoldt, C. A. La Porta, O. Chepizhko, S. Grosser, M. Vullings, G.-J. Bakker, J. Starruß, *et. al.*, *Cell–cell adhesion and 3d matrix confinement determine jamming transitions in breast cancer invasion*, *Nature cell biology* **22** (2020), no. 9 1103–1115.

[43] C. Guillot and T. Lecuit, *Mechanics of epithelial tissue homeostasis and morphogenesis*, *Science* **340** (2013), no. 6137 1185–1189.

[44] A. G. Fletcher, M. Osterfield, R. E. Baker, and S. Y. Shvartsman, *Vertex models of epithelial morphogenesis*, *Biophysical journal* **106** (2014), no. 11 2291–2304.

[45] R. Farhadifar, J.-C. Röper, B. Aigouy, S. Eaton, and F. Jülicher *Current Biology* **17** (2007), no. 24 2095–2104.

[46] D. B. Staple, R. Farhadifar, J.-C. Röper, B. Aigouy, S. Eaton, and F. Jülicher, *Mechanics and remodelling of cell packings in epithelia*, *The European Physical Journal E* **33** (2010), no. 2 117–127.

[47] D. Bi, J. H. Lopez, J. M. Schwarz, and M. L. Manning *Soft matter* **10** (2014), no. 12 1885–1890.

[48] D. Bi, J. Lopez, J. M. Schwarz, and M. L. Manning *Nature Physics* **11** (2015), no. 12 1074–1079.

[49] X. Wang, M. Merkel, L. B. Sutter, G. Erdemci-Tandogan, M. L. Manning, and K. E. Kasza, *Anisotropy links cell shapes to tissue flow during convergent extension*, *Proceedings of the National Academy of Sciences* **117** (2020), no. 24 13541–13551.

[50] A. Jain, V. Ulman, A. Mukherjee, M. Prakash, M. B. Cuenca, L. G. Pimpale, S. Münster, R. Haase, K. A. Panfilio, F. Jug, *et. al.*, *Regionalized tissue fluidization is required for epithelial gap closure during insect gastrulation*, *Nature Communications* **11** (2020), no. 1 5604.

[51] S. Grosser, J. Lippoldt, L. Oswald, M. Merkel, D. M. Sussman, F. Renner, P. Gottheil, E. W. Morawetz, T. Fuhs, X. Xie, *et. al.*, *Cell and nucleus shape as an indicator of tissue fluidity in carcinoma*, *Physical Review X* **11** (2021), no. 1 011033.

[52] M. Leptin, *Drosophila gastrulation: from pattern formation to morphogenesis*, *Annual review of cell and developmental biology* **11** (1995), no. 1 189–212.

[53] F. Brauns, N. H. Claussen, E. F. Wieschaus, and B. I. Shraiman, *Epithelial flow by controlled transformation of internal force-balance geometry*, *bioRxiv* (2023).

[54] J.-F. Rupprecht, K. H. Ong, J. Yin, A. Huang, H.-H.-Q. Dinh, A. P. Singh, S. Zhang, W. Yu, and T. E. Saunders, *Geometric constraints alter cell arrangements within curved epithelial tissues*, *Molecular biology of the cell* **28** (2017), no. 25 3582–3594.

[55] H. S. Seung and D. R. Nelson, *Defects in flexible membranes with crystalline order*, *Physical Review A* **38** (1988), no. 2 1005.

[56] M. Born, K. Huang, and M. Lax, *Dynamical theory of crystal lattices*, *American Journal of Physics* **23** (1955), no. 7 474–474.

[57] J. Ericksen, *The cauchy and born hypotheses for crystals*, *Mechanics and mathematics of crystals: selected papers of JL Ericksen* (2005) 117.

[58] S. Alexander, *What is a solid?*, *Physica A: Statistical Mechanics and its Applications* **249** (1998), no. 1-4 266–275.

[59] B. Halperin and D. R. Nelson, *Theory of two-dimensional melting*, *Physical Review Letters* **41** (1978), no. 2 121.

[60] D. R. Nelson and B. Halperin, *Dislocation-mediated melting in two dimensions*, *Physical Review B* **19** (1979), no. 5 2457.

[61] A. Young, *Melting and the vector coulomb gas in two dimensions*, *Physical Review B* **19** (1979), no. 4 1855.

[62] M. L. Falk and J. S. Langer, *Deformation and failure of amorphous, solidlike materials*, *Annu. Rev. Condens. Matter Phys.* **2** (2011), no. 1 353–373.

[63] T. Egami, K. Maeda, and V. Vitek, *Structural defects in amorphous solids a computer simulation study*, *Philosophical Magazine A* **41** (1980), no. 6 883–901.

[64] S. Alexander, *Amorphous solids: their structure, lattice dynamics and elasticity*, *Physics reports* **296** (1998), no. 2-4 65–236.

[65] M. Moshe, I. Levin, H. Aharoni, R. Kupferman, and E. Sharon, *Geometry and mechanics of two-dimensional defects in amorphous materials*, *Proceedings of the National Academy of Sciences* **112** (2015), no. 35 10873–10878.

[66] A. J. Liu and S. R. Nagel, *The jamming transition and the marginally jammed solid*, *Annu. Rev. Condens. Matter Phys.* **1** (2010), no. 1 347–369.

[67] N. Goldenfeld, *Lectures on phase transitions and the renormalization group*. CRC Press, 2018.

[68] N. Murisic, V. Hakim, I. G. Kevrekidis, S. Y. Shvartsman, and B. Audoly *Biophysical journal* **109** (2015), no. 1 154–163.

[69] B. Loewe, F. Serafin, S. Shankar, M. J. Bowick, and M. C. Marchetti, *Shape and size changes of adherent elastic epithelia*, *Soft Matter* **16** (2020), no. 22 5282–5293.

[70] M. H. Köpf and L. M. Pismen, *A continuum model of epithelial spreading*, *Soft matter* **9** (2013), no. 14 3727–3734.

[71] G. Forgacs, R. A. Foty, Y. Shafrir, and M. S. Steinberg, *Viscoelastic properties of living embryonic tissues: a quantitative study*, *Biophysical journal* **74** (1998), no. 5 2227–2234.

[72] M. Doi and T. Ohta *The Journal of chemical physics* **95** (1991), no. 2 1242–1248.

[73] D. L. Weaire and S. Hutzler, *The physics of foams*. Oxford University Press, 1999.

[74] M. Popović, A. Nandi, M. Merkel, R. Etournay, S. Eaton, F. Jülicher, and G. Salbreux, *Active dynamics of tissue shear flow*, *New Journal of Physics* **19** (2017), no. 3 033006.

[75] J. Ranft, M. Basan, J. Elgeti, J.-F. Joanny, J. Prost, and F. Jülicher *Proceedings of the National Academy of Sciences* **107** (2010), no. 49 20863–20868.

[76] S. Ishihara, P. Marcq, and K. Sugimura *Physical Review E* **96** (2017), no. 2 022418.

[77] F. Pérez-Verdugo and R. Soto, *Continuum description of confluent tissues with spatial heterogeneous activity*, *Soft Matter* **19** (2023), no. 34 6501–6512.

[78] M. Czajkowski, D. Bi, M. L. Manning, and M. C. Marchetti *Soft matter* **14** (2018), no. 27 5628–5642.

[79] S. M. Fielding, J. O. Cochran, J. Huang, D. Bi, and M. C. Marchetti, *Constitutive model for the rheology of biological tissue*, *Physical Review E* **108** (2023), no. 4 L042602.

[80] Y. Han, Y. Shokef, A. M. Alsayed, P. Yunker, T. C. Lubensky, and A. G. Yodh, *Geometric frustration in buckled colloidal monolayers*, *Nature* **456** (2008), no. 7224 898–903.

[81] J. V. Selinger, *Director deformations, geometric frustration, and modulated phases in liquid crystals*, *Annual Review of Condensed Matter Physics* **13** (2022) 49–71.

[82] A. Ramirez, *Strongly geometrically frustrated magnets*, *Annual Review of Materials Science* **24** (1994), no. 1 453–480.

[83] N. Francois, M. Saadatfar, R. Cruikshank, and A. Sheppard, *Geometrical frustration in amorphous and partially crystallized packings of spheres*, *Physical review letters* **111** (2013), no. 14 148001.

[84] G. M. Grason, *Perspective: Geometrically frustrated assemblies*, *The Journal of Chemical Physics* **145** (2016), no. 11.

[85] R. Moessner and A. P. Ramirez, *Geometrical frustration*, *Physics Today* **59** (2006), no. 2 24–29.

[86] M. Moshe, M. J. Bowick, and M. C. Marchetti, *Geometric frustration and solid-solid transitions in model 2d tissue*, *Physical review letters* **120** (2018), no. 26 268105.

[87] O. K. Damavandi, V. F. Hagh, C. D. Santangelo, and M. L. Manning, *Energetic rigidity: a unifying theory of mechanical stability*, *arXiv preprint arXiv:2102.11310* (2021).

[88] O. K. Damavandi, V. F. Hagh, C. D. Santangelo, and M. L. Manning, *Energetic rigidity ii: Applications in examples of biological and underconstrained materials*, *arXiv preprint arXiv:2107.06868* (2021).

[89] M. Merkel and M. L. Manning, *A geometrically controlled rigidity transition in a model for confluent 3d tissues*, *New Journal of Physics* **20** (2018), no. 2 022002.

[90] K. Bertoldi, V. Vitelli, J. Christensen, and M. Van Hecke, *Flexible mechanical metamaterials*, *Nature Reviews Materials* **2** (2017), no. 11 1–11.

[91] M. Czajkowski, C. Coulais, M. van Hecke, and D. Z. Rocklin, *Conformal elasticity of mechanism-based metamaterials*, *Nature communications* **13** (2022), no. 1 211.

[92] M. Czajkowski and D. Rocklin, *Duality and sheared analytic response in mechanism-based metamaterials*, *arXiv preprint arXiv:2205.10751* (2022).

[93] J. Paulose, B. G.-g. Chen, and V. Vitelli, *Topological modes bound to dislocations in mechanical metamaterials*, *Nature Physics* **11** (2015), no. 2 153–156.

[94] D. Z. Rocklin, S. Zhou, K. Sun, and X. Mao, *Transformable topological mechanical metamaterials*, *Nature communications* **8** (2017), no. 1 14201.

[95] S. Armon, H. Aharoni, M. Moshe, and E. Sharon, *Shape selection in chiral ribbons: from seed pods to supramolecular assemblies*, *Soft matter* **10** (2014), no. 16 2733–2740.

[96] D. M. Hall and G. M. Grason, *How geometric frustration shapes twisted fibres, inside and out: competing morphologies of chiral filament assembly*, *Interface Focus* **7** (2017), no. 4 20160140.

[97] M. Lenz and T. A. Witten, *Geometrical frustration yields fibre formation in self-assembly*, *Nature physics* **13** (2017), no. 11 1100–1104.

[98] M. Merkel, K. Baumgarten, B. P. Tighe, and M. L. Manning, *A minimal-length approach unifies rigidity in underconstrained materials*, *Proceedings of the National Academy of Sciences* **116** (2019), no. 14 6560–6568.

[99] T. C. Hales, *The honeycomb conjecture*, *Discrete & computational geometry* **25** (2001) 1–22.

[100] A.-K. Classen, K. I. Anderson, E. Marois, and S. Eaton, *Hexagonal packing of drosophila wing epithelial cells by the planar cell polarity pathway*, *Developmental cell* **9** (2005), no. 6 805–817.

[101] R. Farhadifar, *Dynamics of cell packing and polar order in developing epithelia*, .

[102] W. T. D'Arcy, *On growth and form*, *Cambridge Univ. Press* **1** (1942), no. 6 7.

[103] W. Kong, O. Loison, P. Chavadimane Shivakumar, E. H. Chan, M. Saadaoui, C. Collinet, P.-F. Lenne, and R. Clément, *Experimental validation of force inference in epithelia from cell to tissue scale*, *Scientific reports* **9** (2019), no. 1 14647.

[104] J.-M. Armengol-Collado, L. N. Carenza, J. Eckert, D. Krommydas, and L. Giomi, *Epithelia are multiscale active liquid crystals*, *Nature Physics* (2023) 1–7.

[105] M. C. Gibson, A. B. Patel, R. Nagpal, and N. Perrimon, *The emergence of geometric order in proliferating metazoan epithelia*, *Nature* **442** (2006), no. 7106 1038–1041.

[106] G. Salbreux, G. Charras, and E. Paluch, *Actin cortex mechanics and cellular morphogenesis*, *Trends in cell biology* **22** (2012), no. 10 536–545.

[107] M. Murrell, P. W. Oakes, M. Lenz, and M. L. Gardel, *Forcing cells into shape: the mechanics of actomyosin contractility*, *Nature reviews Molecular cell biology* **16** (2015), no. 8 486–498.

[108] B. Ladoux and R.-M. Mège, *Mechanobiology of collective cell behaviours*, *Nature reviews Molecular cell biology* **18** (2017), no. 12 743–757.

[109] F. Graner and J. A. Glazier *Physical review letters* **69** (1992), no. 13 2013.

[110] M. C. Marchetti, J.-F. Joanny, S. Ramaswamy, T. B. Liverpool, J. Prost, M. Rao, and R. A. Simha, *Hydrodynamics of soft active matter*, *Reviews of modern physics* **85** (2013), no. 3 1143.

[111] S. Banerjee and M. C. Marchetti, *Continuum models of collective cell migration*, *Cell Migrations: Causes and Functions* (2019) 45–66.

[112] R. Alert and X. Trepat, *Physical models of collective cell migration*, *Annual Review of Condensed Matter Physics* **11** (2020) 77–101.

[113] S. Alt, P. Ganguly, and G. Salbreux, *Vertex models: from cell mechanics to tissue morphogenesis*, *Philosophical Transactions of the Royal Society B: Biological Sciences* **372** (2017), no. 1720 20150520.

[114] T. Nagai and H. Honda, *A dynamic cell model for the formation of epithelial tissues*, *Philosophical Magazine B* **81** (2001), no. 7 699–719.

[115] F. Graner, Y. Jiang, E. Janiaud, and C. Flament, *Equilibrium states and ground state of two-dimensional fluid foams*, *Physical Review E* **63** (2000), no. 1 011402.

[116] R. Höhler and S. Cohen-Addad, *Rheology of liquid foam*, *Journal of Physics: Condensed Matter* **17** (2005), no. 41 R1041.

[117] M. Marder, *Soap-bubble growth*, *Phys. Rev. A* **36** (Jul, 1987) 438–440.

[118] K. Kawasaki, T. Nagai, and K. Nakashima, *Vertex models for two-dimensional grain growth*, *Philosophical Magazine B* **60** (1989), no. 3 399–421.

[119] C.-Y. Loh, J. Y. Chai, T. F. Tang, W. F. Wong, G. Sethi, M. K. Shanmugam, P. P. Chong, and C. Y. Looi, *The e-cadherin and n-cadherin switch in epithelial-to-mesenchymal transition: signaling, therapeutic implications, and challenges*, *Cells* **8** (2019), no. 10 1118.

[120] M. F. Izaguirre, D. Larrea, J. F. Adur, J. E. Diaz-Zamboni, N. Vicente, C. Galetto, and V. H. Casco, *Role of e-cadherin in epithelial architecture maintenance*, *Cell communication & adhesion* **17** (2010), no. 1 1–12.

[121] L. Yan and D. Bi, *Multicellular rosettes drive fluid-solid transition in epithelial tissues*, *Physical Review X* **9** (2019), no. 1 011029.

[122] A. Hernandez, M. F. Staddon, M. J. Bowick, M. C. Marchetti, and M. Moshe, *Anomalous elasticity of a cellular tissue vertex model*, *Physical Review E* **105** (2022), no. 6 064611.

[123] R. Kupferman, B. Maman, and M. Moshe, *Continuum mechanics of a cellular tissue model*, *Journal of the Mechanics and Physics of Solids* **143** (2020) 104085.

[124] R. Osserman, *The isoperimetric inequality*, *Bulletin of the American Mathematical Society* **84** (1978), no. 6 1182–1238.

[125] J. Huang, J. O. Cochran, S. M. Fielding, M. C. Marchetti, and D. Bi, *Shear-driven solidification and nonlinear elasticity in epithelial tissues*, *arXiv preprint arXiv:2109.10374* (2021).

[126] A. Hernandez, M. F. Staddon, M. J. Bowick, M. C. Marchetti, and M. Moshe, *Anomalous elasticity of a cellular tissue vertex model*, *Physical Review E* **105** (2022), no. 6 064611.

[127] M. Gómez-González, E. Latorre, M. Arroyo, and X. Trepat, *Measuring mechanical stress in living tissues*, *Nature Reviews Physics* **2** (2020), no. 6 300–317.

[128] P. Sahu, J. Kang, G. Erdemci-Tandogan, and M. L. Manning, *Nonlinear analysis of the fluid-solid transition in a model for ordered biological tissues*, *arXiv preprint arXiv:1905.12714* (2019).

[129] S. Tong, N. K. Singh, R. Sknepnek, and A. Kosmrlj, *Linear viscoelastic properties of the vertex model for epithelial tissues*, *arXiv preprint arXiv:2102.11181* (2021).

[130] C. Scheibner, A. Souslov, D. Banerjee, P. Surówka, W. T. Irvine, and V. Vitelli, *Odd elasticity*, *Nature Physics* **16** (2020), no. 4 475–480.

[131] H. Honda, *Geometrical models for cells in tissues*, *International review of cytology* **81** (1983) 191–248.

[132] K. K. Chiou, L. Hufnagel, and B. I. Shraiman, *Mechanical stress inference for two dimensional cell arrays*, *PLoS computational biology* **8** (2012), no. 5 e1002512.

[133] D. L. Barton, S. Henkes, C. J. Weijer, and R. Sknepnek, *Active vertex model for cell-resolution description of epithelial tissue mechanics*, *PLoS computational biology* **13** (2017), no. 6 e1005569.

[134] M. Merkel, R. Etournay, M. Popović, G. Salbreux, S. Eaton, and F. Jülicher, *Triangles bridge the scales: Quantifying cellular contributions to tissue deformation*, *Physical Review E* **95** (2017), no. 3 032401.

[135] M. Popović, V. Druelle, N. A. Dye, F. Jülicher, and M. Wyart, *Inferring the flow properties of epithelial tissues from their geometry*, *New Journal of Physics* **23** (2021), no. 3 033004.

[136] D. Grossman and J.-F. Joanny, *Instabilities and geometry of growing tissue*, *arXiv preprint arXiv:2108.05326* (2021).

[137] T. Lubensky, C. Kane, X. Mao, A. Souslov, and K. Sun, *Phonons and elasticity in critically coordinated lattices*, *Reports on Progress in Physics* **78** (2015), no. 7 073901.

[138] M. Sheinman, C. Broedersz, and F. MacKintosh, *Nonlinear effective-medium theory of disordered spring networks*, *Physical Review E* **85** (2012), no. 2 021801.

[139] E. Siéfert, I. Levin, and E. Sharon, *Euclidean frustrated ribbons*, *Physical Review X* **11** (2021), no. 1 011062.

[140] R. Kupferman and C. Maor, *Variational convergence of discrete geometrically-incompatible elastic models*, *Calculus of Variations and Partial Differential Equations* **57** (2018), no. 2 1–27.

[141] J. R. Barber, *Elasticity*. Springer, 2002.

[142] K. A. Brakke, *The surface evolver*, *Experimental mathematics* **1** (1992), no. 2 141–165.

[143] M. F. Staddon, A. Hernandez, M. J. Bowick, M. Moshe, and M. C. Marchetti, *The role of non-affine deformations in the elastic behavior of the cellular vertex model*, *Soft Matter* **19** (2023), no. 17 3080–3091.

[144] M. L. Falk and J. S. Langer, *Dynamics of viscoplastic deformation in amorphous solids*, *Physical Review E* **57** (1998), no. 6 7192.

[145] B. Utter and R. Behringer, *Experimental measures of affine and nonaffine deformation in granular shear*, *Physical review letters* **100** (2008), no. 20 208302.

[146] W. G. Ellenbroek, Z. Zeravcic, W. van Saarloos, and M. van Hecke, *Non-affine response: Jammed packings vs. spring networks*, *EPL (Europhysics Letters)* **87** (2009), no. 3 34004.

[147] A. Zaccone and E. Scossa-Romano, *Approximate analytical description of the nonaffine response of amorphous solids*, *Physical Review B* **83** (2011), no. 18 184205.

[148] M. F. Staddon, M. P. Murrell, and S. Banerjee, *Interplay between substrate rigidity and tissue fluidity regulates cell monolayer spreading*, *Soft Matter* **18** (2022), no. 40 7877–7886.

[149] O. K. Damavandi, V. F. Hagh, C. D. Santangelo, and M. L. Manning, *Energetic rigidity. i. a unifying theory of mechanical stability*, *Physical Review E* **105** (2022), no. 2 025003.

[150] O. K. Damavandi, V. F. Hagh, C. D. Santangelo, and M. L. Manning, *Energetic rigidity. ii. applications in examples of biological and underconstrained materials*, *Physical Review E* **105** (2022), no. 2 025004.

[151] A. Hernandez, M. F. Staddon, M. Moshe, and M. C. Marchetti, *Finite elasticity of the vertex model and its role in rigidity of curved cellular tissues*, *Soft Matter* **19** (2023) 7744–7752.

[152] M. J. Hertaeg, S. M. Fielding, and D. Bi, *Discontinuous shear thickening in biological tissue rheology*, *arXiv preprint arXiv:2211.15015* (2022).

[153] B. Schamberger, R. Ziege, K. Anselme, M. Ben Amar, M. Bykowski, A. P. Castro, A. Cipitria, R. A. Coles, R. Dimova, M. Eder, *et. al.*, *Curvature in biological systems: Its quantification, emergence, and implications across the scales*, *Advanced Materials* **35** (2023), no. 13 2206110.

[154] F.-L. Wen, *Expansion of ring-shaped supracellular contractile cables induces epithelial sheet folding*, *Physical Review E* **106** (2022), no. 6 064403.

[155] Y. Ogura, F.-L. Wen, M. M. Sami, T. Shibata, and S. Hayashi, *A switch-like activation relay of egfr-erk signaling regulates a wave of cellular contractility for epithelial invagination*, *Developmental cell* **46** (2018), no. 2 162–172.

[156] D. M. Sussman, *Interplay of curvature and rigidity in shape-based models of confluent tissue*, *Physical Review Research* **2** (2020), no. 2 023417.

[157] M. De Marzio, A. Das, J. J. Fredberg, and D. Bi, *Epithelial layer fluidization by curvature-induced unjamming*, *arXiv preprint arXiv:2305.12667* (2023).

[158] X. Mao and T. C. Lubensky, *Maxwell lattices and topological mechanics*, *Annual Review of Condensed Matter Physics* **9** (2018) 413–433.

[159] I. Levin and E. Sharon, *Anomalously soft non-euclidean springs*, *Physical review letters* **116** (2016), no. 3 035502.

[160] M. Arieli, E. Sharon, and M. Moshe, *Geometric approach to mechanical design principles in continuous elastic sheets*, *arXiv preprint arXiv:2105.00751* (2021).

[161] A. Gray and L. Vanhecke, *Riemannian geometry as determined by the volumes of small geodesic balls*, *Acta Mathematica* **142** (1979) 157–198.

[162] A. Gray, *Tubes*, vol. 221. Springer Science & Business Media, 2003.

[163] T. Willmore, *Riemannian Geometry*. Oxford Science Publications, 1993.

[164] O. Veblen and J. Whitehead, *Foundations of Differential Geometry*. Cambridge Press, 1932.

[165] A. Hernandez and M. C. Marchetti, *Poisson-bracket formulation of the dynamics of fluids of deformable particles*, *Phys. Rev. E* **103** (Mar, 2021) 032612.

[166] T. Lecuit and P.-F. Lenne, *Cell surface mechanics and the control of cell shape, tissue patterns and morphogenesis*, *Nature reviews Molecular cell biology* **8** (2007), no. 8 633–644.

[167] D. J. Durian *Phys. Rev. Lett.* **75** (Dec, 1995) 4780–4783.

[168] S. Cohen-Addad, R. Höhler, and O. Pitois *Annual Review of Fluid Mechanics* **45** (2013).

[169] J. Mattsson, H. M. Wyss, A. Fernandez-Nieves, K. Miyazaki, Z. Hu, D. R. Reichman, and D. A. Weitz *Nature* **462** (2009), no. 7269 83–86.

[170] D. Vlassopoulos and M. Cloitre *Current opinion in colloid & interface science* **19** (2014), no. 6 561–574.

[171] A. J. Kabla *Journal of The Royal Society Interface* **9** (2012), no. 77 3268–3278.

[172] H. Honda, M. Tanemura, and T. Nagai *Journal of theoretical biology* **226** (2004), no. 4 439–453.

[173] L. Hufnagel, A. A. Teleman, H. Rouault, S. M. Cohen, and B. I. Shraiman *Proceedings of the National Academy of Sciences* **104** (2007), no. 10 3835–3840.

[174] E. Hannezo, J. Prost, and J.-F. Joanny *Proceedings of the National Academy of Sciences* **111** (2014), no. 1 27–32.

[175] E. Teomy, D. A. Kessler, and H. Levine *Physical Review E* **98** (2018), no. 4 042418.

[176] A. Boromand, A. Signoriello, J. Lowensohn, C. S. Orellana, E. R. Weeks, F. Ye, M. D. Shattuck, and C. S. O'Hern *Soft matter* **15** (2019), no. 29 5854–5865.

[177] A. Sagner, M. Merkel, B. Aigouy, J. Gaebel, M. Brankatschk, F. Jülicher, and S. Eaton *Current Biology* **22** (2012), no. 14 1296–1301.

[178] M. Popović, A. Nandi, M. Merkel, R. Etournay, S. Eaton, F. Jülicher, and G. Salbreux *New Journal of Physics* **19** (2017), no. 3 033006.

[179] X. Yang, D. Bi, M. Czajkowski, M. Merkel, M. L. Manning, and M. C. Marchetti *Proceedings of the National Academy of Sciences* **114** (2017), no. 48 12663–12668.

[180] D. Forster *Physical Review Letters* **32** (1974), no. 21 1161.

[181] H. Stark and T. C. Lubensky *Phys. Rev. E* **67** (Jun, 2003) 061709.

[182] H. Stark and T. C. Lubensky *Physical Review E* **72** (Nov, 2005).

[183] L. V. Goodrich and D. Strutt, *Principles of planar polarity in animal development*, *Development* **138** (2011), no. 10 1877–1892.

[184] A. N. Beris, B. J. Edwards, B. J. Edwards, *et. al.*, *Thermodynamics of flowing systems: with internal microstructure*. No. 36. Oxford University Press on Demand, 1994.

[185] F. Graner, B. Dollet, C. Raufaste, and P. Marmottant, *Discrete rearranging disordered patterns, part i: Robust statistical tools in two or three dimensions*, *The European Physical Journal E* **25** (2008), no. 4 349–369.

[186] S. R. De Groot, *Thermodynamics of irreversible processes*. (North-Holland Amsterdam, 1951).

[187] S. T. Milner *Phys. Rev. E* **48** (1993) 3674–3691.

[188] T. R. Chandrupatla and T. J. Osler, *The perimeter of an ellipse.*, *Mathematical Scientist* **35** (2010), no. 2.

[189] N. S. Livne, A. Schiller, and M. Moshe, *Geometric theory of mechanical screening in two-dimensional solids*, *Physical Review E* **107** (2023), no. 5 055004.

[190] A. Lemaître, C. Mondal, M. Moshe, I. Procaccia, S. Roy, and K. Screiber-Re'em, *Anomalous elasticity and plastic screening in amorphous solids*, *Physical Review E* **104** (2021), no. 2 024904.